

Intercalation of the Quantum Spin Hall Insulator Indenene into the Silicon Carbide/Graphene Interface

Master thesis

Cedric Franz Schmitt



Julius-Maximilians-Universität Würzburg

Chair of experimental physics 4

Prof. Dr. Ralph Claessen

Group of Dr. Simon Moser

Würzburg, 2022

Master's thesis

Intercalation of the Quantum Spin Hall Insulator Indene into the Silicon Carbide/Graphene Interface

submitted by

Cedric Franz Schmitt

1. Examiner:

Prof. Dr. Ralph Claessen

Experimentelle Physik IV

Julius-Maximilians-Universität Würzburg

2. Examiner:

Prof. Dr. Friedrich Reinert

Experimentelle Physik VII

Julius-Maximilians-Universität Würzburg

Fakultät für Physik und Astronomie
Experimentelle Physik IV
Julius-Maximilians-Universität Würzburg
Am Hubland, 97074 Würzburg, Deutschland

Zusammenfassung

Zweidimensionale topologische Isolatoren sind Materialsysteme, die den Quanten-Spin-Hall-Effekt zeigen. Damit sind sie vielversprechende Kandidaten für energiesparende Anwendungen in der Elektronik und der Spintronik. Die Materialklasse zeichnet sich dadurch aus, dass sie isolierend in der Fläche ist, aber metallische und spinpolarisierte Randkanäle besitzt, die durch Symmetriebedingungen vor elastischen Streuungen an Defekten geschützt sind. Der Strom kann hier verlustfrei geleitet werden. Ein erst kürzlich realisierter topologischer Isolator ist Indenen. Letzteres bezeichnet eine Monolage Indium, die auf einem 4H-SiC(0001) Substrat gewachsen wird. Bringt man dieses System jedoch an Luft, oxidiert Indenen und verliert seine besonderen topologischen Eigenschaften.

Ziel dieser Arbeit ist es, das Indenen mit einer Graphenschicht abzudecken und damit vor Oxidation zu schützen. Dazu wird zunächst Graphen auf dem SiC Substrat epitaktisch gewachsen und anschließend werden Indium Atome in die Zwischenschicht interkaliert.

Zu Beginn dieser Arbeit werden die verwendeten Methoden der Oberflächenanalyse vorgestellt. Anschließend ist die Arbeit in zwei Bereiche gegliedert. Zunächst wird das Wachstum von Graphen auf dem Substrat untersucht und die bestmöglichen Startbedingungen für den Interkalationsprozess festgelegt. Es wurden drei verschiedene Dicken der Graphenschicht charakterisiert. Neben der graphitisierten Pufferschicht wurden noch die Mono- und die Bilage von Graphen untersucht. Für die Charakterisierung wurden Beugungsexperimente mit niederenergetischen Elektronen, Rastertunnelmikroskopie und -spektroskopie, sowie Photoelektronenspektroskopie angewendet. Durch gezielte Fehlstellen in der Graphenschicht können die Indium Atome in die Zwischenschicht interkalieren und entkoppeln damit die Pufferschicht vom Substrat. Dadurch bildet sich eine quasi-freistehende Graphenschicht über dem Indenen aus. Das Indium tritt nach der Interkalation zunächst als Bilage auf. Durch anschließendes Heizen wird eine Lage entfernt und es entsteht die topologische Monolage Indenen. Mittels Photoelektronenspektroskopie wird dann der elektronische Charakter der interkalierten Monolage untersucht und mit dem ungeschützten Indenen verglichen. Transmissionselektronenmikroskopie Aufnahmen belegen außerdem den Schutz vor Luft. Des Weiteren hat sich herausgestellt, dass das Graphen die topologische Monolage beeinflusst. Im direkten Vergleich mit der

ungeschützten Indenen Probe wird gezeigt, dass durch das Graphen der In-Si Bindungsabstand erhöht wird. Dadurch wird das Indenen tiefer in die Quanten Spin Hall Isolator Phase gebracht.

Zusammenfassend zeigt diese Arbeit, dass Indenen in die SiC/Graphen-Grenzfläche interkaliert werden kann, vor Umgebungsbedingungen geschützt ist und die Topologie erhalten bleibt.

Abstract

Two-dimensional topological insulators exhibit the quantum spin Hall effect, making them a promising candidate for energy-saving electronic devices, as well as for spintronic applications. This class of materials exhibits one-dimensional metallic and spin-polarized edge states, which are protected from elastic scattering at defects by symmetry conservations. This leads to a dissipationless electronic transport at the edge, the bulk, however, is insulating. A recently realized quantum spin Hall insulator consists of a monolayer of indium on a 4H-SiC(0001) substrate and is named indenene. If the new quantum material is exposed to ambient conditions, indenene oxidizes and loses its special properties.

The goal of this thesis is to protect indenene from degradation in air by a graphene capping. For this purpose, the buffer layer graphene is epitaxially grown on the SiC substrate. In the next step, indium atoms are intercalated into the graphene/SiC interface.

In the beginning of this thesis the methods for surface analysis are introduced. Afterwards the work is divided into two sections. Inspired by publications, the growth of graphene on SiC, is reproduced in order to identify the best possible starting conditions for the intercalation process. Here, three different graphene coverages could be qualitatively grown, namely the graphitized buffer layer, mono- and bilayer graphene. The three phases were investigated by low-energy electron diffraction, scanning tunneling microscopy and -spectroscopy and photoelectron spectroscopy. Intentional defects in the graphene layer allow the indium atoms to intercalate into the interface. Hereby, the buffer layer decouples from the substrate and forms a quasi-freestanding graphene layer. The intercalated indium is found to form as a bilayer. Subsequent annealing removes one In layer and thus yields intercalated indenene. Photoelectron spectroscopy confirms that the electronic properties of the intercalated monolayer are preserved and transmission electron microscopy images reveal the protection from air. A direct comparison with the unprotected indenene shows, that the graphene influences the intercalant as it increases the In-Si bond length, which drives the indenene even deeper into the quantum spin hall insulating regime.

In conclusion, this thesis shows, that indenene can be intercalated to the SiC/graphene interface, is protected from ambient conditions and the topology is preserved.

Contents

1	Motivation: A roadmap to energy-saving electronic devices	11
2	Experimental methods	13
2.1	Sample fabrication	13
2.2	Methods for surface analysis	14
2.2.1	Scanning tunneling microscopy	15
2.2.2	Inelastic mean free path	18
2.2.3	Low-energy electron diffraction	19
2.2.4	Photoelectron spectroscopy	21
3	Graphene on silicon carbide	27
3.1	Physics of graphene	27
3.1.1	Electronic properties of graphene	27
3.1.2	Epitaxial graphene	31
3.2	Growth of epitaxial graphene	33
3.2.1	Hydrogen passivation of the 4H-SiC substrate	33
3.2.2	Growth of the buffer layer graphene	34
3.2.3	Quasi-freestanding monolayer graphene	39
3.2.4	Bilayer graphene	43
4	Intercalation of indenene into graphene/SiC	45
4.1	Topological insulators	45
4.1.1	Su-Schrieffer-Heeger model	46
4.1.2	Two-dimensional topological insulators	48
4.2	Indenene - a novel quantum material	49
4.3	Indium intercalation	52

4.4	Roadmap to indenene intercalation	54
4.5	Electronic properties of the intercalated indenene	56
4.6	Heat and oxidation stability of indenene	61
4.7	Topological properties of intercalated indenene	64
5	Conclusion and Outlook	71
	Bibliography	75
	Acknowledgements	85
	Selbstständigkeitserklärung	87

Chapter 1

Motivation: A roadmap to energy-saving electronic devices

Reducing the CO₂ emission to keep the man-made global warming within 2°C to avoid irreversible consequences such as sea-level rise, wildfires and heatwaves are challenging. To achieve this goal the search for new energy-saving electronic devices is highly important [1]. A potential solution could be a new class of materials, the so-called topological insulators (TIs) [2]. They are insulating in the bulk, but have dissipationless metallic edge states, which are protected by time-reversal symmetry (TRS).

In view of the ever-increasing miniaturization of electronic components [3], ultra-thin metals are highly interesting as they push bulk properties to the 2D limit. The first bulk material, that was reduced to an atomic thick two-dimensional (2D) layer was graphite. In 2004 Geim and Novoselov managed to peel off one layer of graphite, namely graphene, just by using scotch tape [4]. For the discovery and the groundbreaking experiments on this 2D material, they were awarded with the physics Nobel prize in 2010.

One year after the discovery of the first 2D material, Kane and Mele theoretically described graphene as a quantum spin Hall insulator (QSHI), which is the 2D version of a TI [5]. Due to the spin-orbit coupling (SOC) in graphene, a bulk energy gap with helical edge states opens and gives rise to the non-trivial topology. The scaling of SOC with Z^4 , however, yields a gap of less than 50 μeV for graphene ($Z=6$), not suitable for electronic application at any temperature [6]. Thus, the quantum spin Hall effect (QSHE) was first experimentally realized in HgTe/CdTe quantum wells by the group of Molenkamp in 2007 [7]. Although this discovery was realized in a semiconductor heterostructure, the honeycomb lattices still dominate the field of QSHIs. By replacing the light C atoms with heavy Bi atoms, the group of Claessen found the QSHI with the so far largest energy gap of around 800 meV to be bismuthene [8]. The larger abundance of triangular adsorbates on hexagonal substrates compared to the honeycomb structure leads to the search for new quantum materials with a triangular structure. In 2021 the group of Claessen also realized

the first large-gap QSHI on a triangular lattice consisting of a single layer of indium on a silicon carbide (SiC) substrate, called indenene [9].

Nevertheless, applications of these systems demand to overcome further obstacles. An exposure to ambient atmosphere leads to an instantaneous oxidation of the indenene. Hence, the QSHI needs to be protected by a capping material. This thesis aims to combine graphene and indenene, to protect the latter against reactions with air. For this purpose, the graphene layer is grown on a SiC substrate and subsequently In atoms are intercalated into the SiC/graphene interface. Due to the inert graphene layer on top of the indenene, it remains intact upon air exposure.

Starting with chapter 2 the sample fabrication and methods of investigation are discussed. Scanning tunneling microscopy (STM), photoelectron spectroscopy (PES) and low-energy electron diffraction (LEED) are explicitly presented. Chapter 3 introduces the theoretical framework of graphene as a mono- and bilayer and its different growth methods. Afterwards, the epitaxial growth of the buffer layer as well as the mono- and bilayer graphene on the SiC substrate is treated. In chapter 4 the non-trivial topology is introduced, where the one-dimensional Su-Schrieffer-Heeger (SSH) model builds the bridge to the 2D QSHIs. Besides the indium intercalation and the subsequent indenene formation, the temperature and oxidation stability is studied. Furthermore, the topology of the new system is discussed and compared to pristine indenene.

Chapter 2

Experimental methods

The investigated 2D materials are evaporated onto a flat H-saturated SiC substrate using molecular beam epitaxy (MBE). STM measurements resolve the surface atomically and provide information about the local density of states (LDOS) of the sample. The high quality of the sample growth and its long-range periodicity is confirmed by LEED. For a more detailed study, including the chemical composition and the energy dispersion, PES is necessary.

2.1 Sample fabrication

In this work, n-doped 4H-SiC(0001) substrates are used. They were produced and polished by the company TankeBlue Semiconductor Co. Ltd. with a miss-orientation of less than 0.5° and a sample resistivity of $R = (0.015 - 0.028) \Omega\text{cm}$. The (11.0×2.5) mm wafers have a thickness of 0.34 mm and for the growth the Si-terminated side is used. The substrates are treated with a triple organic cleaning process inside a flow box. During this process, the SiC wafer is slewed for 2 min successively in acetone, isopropanol and methanol, in order to clean the sample surface from contaminations. After that, the substrate is mounted on a Scienta Omicron DC-sample holder, as illustrated in Fig. 2.1a. The rhodium foil between the SiC substrate and the sample holder reduces the Schottky barrier. For an even better electrical contact, the overlying substrate ends are roughened with a hard and sharp material e.g. diamond. After that, the SiC substrates were put into an ultra-high vacuum (UHV) chamber to continue the in-situ etching process, as described in Ref. [10]. At first the sample is degassed at 950°C until a base pressure of $< 3 \cdot 10^{-8}$ mbar is reached. At this point, adsorbates from the triple organic process are removed. The sample is then heated by an applied direct current, while the temperature is read out through a pyrometer (emissivity $\epsilon = 85\%$). For hydrogen etching, the pressure of the chamber is set to 950 mbar by adding He and H₂ with a 2 slm flux of He (7.0 purity) and

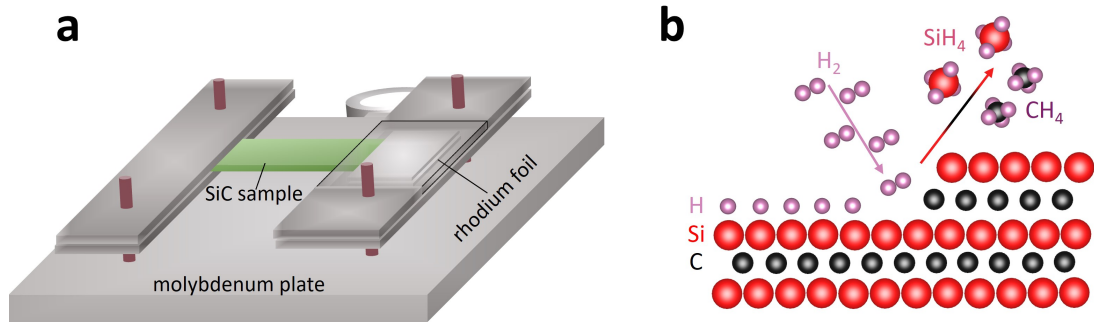


Fig. 2.1: **a** Schematic structure of the SiC sample in the Scienta Omicron DC setup. Rhodium foil ensures a lower Schottky barrier. **b** Hydrogen etching process showing, that the H₂ atoms are cracked due to the hot surface and bind to Si and C atoms. They are removed and form SiH₄ and CH₄, respectively. Adapted from Ref. [10].

H (7.0 purity). The sample temperature is first held at $T=1250\text{ }^{\circ}\text{C}$ for 2 min, subsequently at $1180\text{ }^{\circ}\text{C}$ for 5 min and finally cooled down to $255\text{ }^{\circ}\text{C}$ within 11 min. This temperature is held for another 10 min in the UHV for a second degassing. During the etching process, the hot surface temperature cracks the hydrogen molecules into highly reactive atomic hydrogen [10]. This is illustrated in Fig. 2.1b. The atomic H adsorbs predominantly on Si and C at the edges as here more unsaturated bonds are present. They are removed and form silane (SiH₄) and methane (CH₄). The layer-by-layer removal in a hydrogen flow, which prevents redeposition, is decisive for the atomically flat and H-saturated SiC surface.

After the etching process, the sample is annealed up to $1300\text{ }^{\circ}\text{C}$ to grow different layers of graphene on top of the substrate. This is described in chapter 3. Afterwards, indium is intercalated in the graphene/SiC interface by a two-step process. Using a Knudsen cell, indium with a purity of 99.9999% is evaporated for 10 min on the graphene at room temperature (RT). Subsequently the sample is post-annealed to $500\text{ }^{\circ}\text{C}$ for 20 min. Hereby the In atoms can penetrate through the buffer layer graphene and lift this layer to form a free-standing graphene layer. This process is repeated twelve times to achieve a homogeneous In intercalation, while the temperature is controlled by a PID.

2.2 Methods for surface analysis

In this section, the surface analysis methods used in this work are described. Particular focus is placed on STM, which atomically resolves the sample surface, as well as LEED and PES to characterize 2D materials in detail. Further techniques, like X-ray standing wave measurements (XSW) [11], transmission electron microscopy (TEM) [12, 13] and Raman spectroscopy [14], as well as the density functional theory (DFT) for the electronic structure calculations [15, 16] are only used supplementary in this work. Their detailed

description would exceed the frame of this chapter but can be found in detail in the stated literature.

2.2.1 Scanning tunneling microscopy

In 1981 Binnig and Rohrer discovered the electron tunneling between a tungsten tip and a platinum sample [17]. By scanning the tip over the sample an atomic structure image is produced. Thereby, the STM, a novel surface analytical instrument was developed. For their discovery, they were awarded with the Nobel prize in physics in 1986 [18].

The general principle of STM is to bring a metallic tip within a few ångström above the sample. By applying a bias voltage between the atomically sharp tip and the sample, electrons can tunnel through the vacuum barrier. This tunneling is possible, due to the wavelike properties of the electrons. In quantum mechanics the probability for the electron to penetrate through a potential barrier is given by

$$T \propto e^{-2\kappa \cdot d} = e^{-2\sqrt{2m(\Phi_0 - E)/\hbar^2} \cdot d}, \quad (2.1)$$

where Φ_0 is the potential, κ is the decay rate, $\hbar = h/2\pi$ with h being the Planck constant and d the width of the rectangular barrier [18]. The sensitivity of the tunneling probability inside the barrier leads to an exponential dependence of the tunneling current in an STM measurement. Thus, small changes in the tip-to-sample distance d have a huge influence on the current and therefore individual atoms can be observed.

In Fig. 2.2 a typical STM setup is depicted. The tunneling current is measured by a current amplifier, which is connected to a control unit. The STM images shown in this thesis were performed in the so-called constant current imaging (CCI) mode. The control unit adjusts the height of the tip from the sample surface during the scan, to keep the tunneling current at a constant value. This height adjustment, as well as the x and y tip movements are performed by piezoelectric crystals [19]. The tip rasterizes the sample surface line by line and for each pixel, the required voltage for the piezoelectric devices is recorded. Together with the applied voltages $U_{x,y}$, to move the sample in x and y direction, a computer can translate $U_{x,y,z}$ to a contour map $z(x, y)$. However, such a “topographic” image does not only provide information about the surface topography, but it also contains specific sample properties and therefore a more detailed theoretical description of the tunneling current is discussed below [19].

Theoretical expression for the tunneling current

All the theoretical descriptions are evaluated in a time-dependent treatment, also known as Bardeen’s formalism [20]. Using the first-order perturbation theory the tunneling current

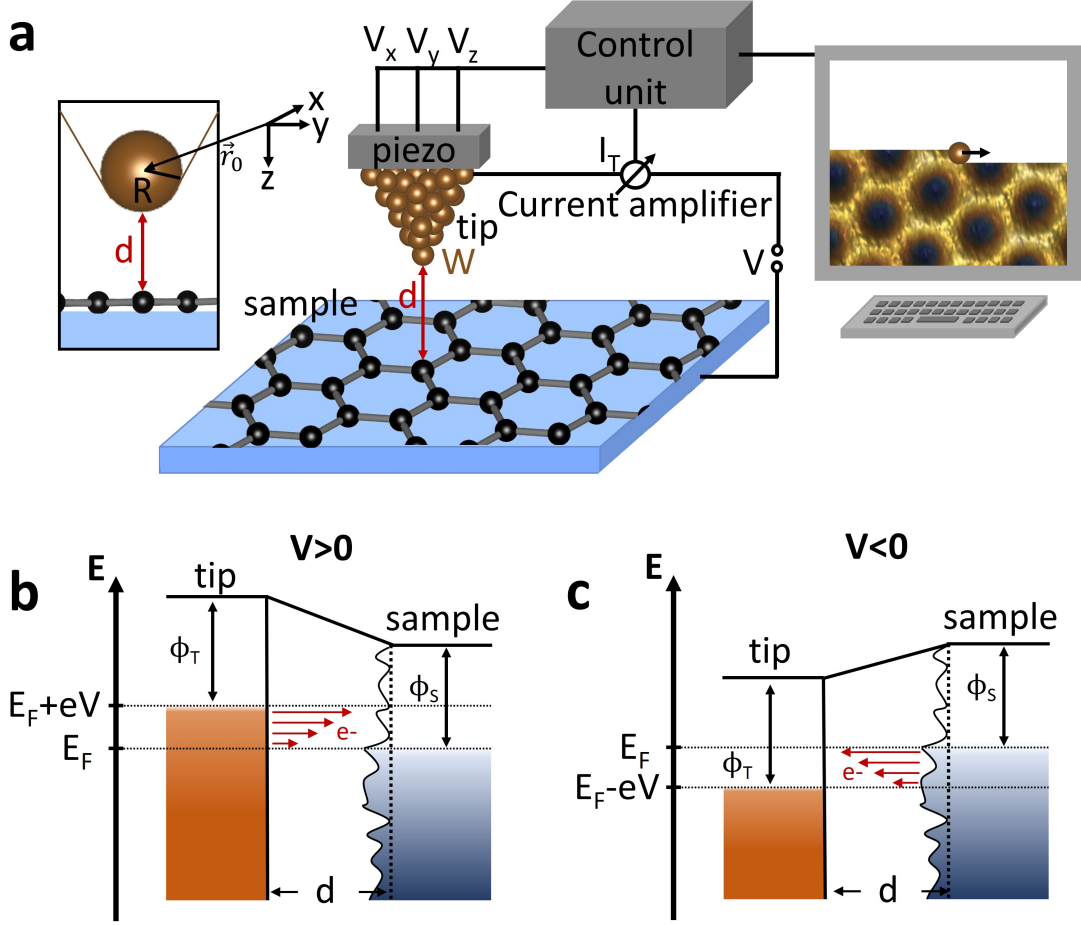


Fig. 2.2: **a** STM setup for a CCI measurement. The W tip is brought a few ångström above the samples surface and by applying a bias voltage between tip and sample, electrons can tunnel through the vacuum barrier. The control unit readjusts the height of the sample, by monitoring the z piezoelectric device, for a constant tunneling current I_T . The STM contour map is visualized by a computer. The enlargement on the left-hand side shows the s -type tip wave function in the model from Tersoff and Hamann. **b,c** Electron tunneling depending on the bias voltage. **b** Electrons tunnel from the tip to the sample for $V > 0$ and vice versa for $V < 0$. The length of the red arrows indicates the states of the electrons, which contribute the most to the tunneling current.

I_T between tip and sample is given by

$$I_T = \frac{2\pi e}{\hbar} \sum_{\mu\nu} \left\{ \underbrace{f(E_\mu)[1 - f(E_\nu + eV)]}_{\text{tip} \rightarrow \text{sample}} - \underbrace{f(E_\nu + eV)[1 - f(E_\mu)]}_{\text{sample} \rightarrow \text{tip}} \right\} |M_{\mu,\nu}|^2 \delta(E_\nu - E_\mu), \quad (2.2)$$

where $f(E)$ is the Fermi function and V is the applied voltage between tip and sample [19]. The delta function ensures only elastic tunneling, where E_ν (E_μ) is the energy of state Ψ_ν (Ψ_μ) of the sample (tip) in the unperturbed case. The first and second term in

Eq. (2.2) corresponds to tunneling from tip to sample and sample to tip, respectively. The calculation of the tunneling matrix element

$$M_{\mu\nu} = -\frac{\hbar^2}{2m} \int (\Psi_\mu^* \nabla \Psi_\nu - \Psi_\nu \nabla \Psi_\mu^*) d\vec{S} \quad (2.3)$$

faces a problem, since the integral over a surface lying inside the vacuum barrier must be solved, which also requires the knowledge of the two wave functions Ψ_ν and Ψ_μ . However, the wave function of the tip Ψ_μ is not known [19]. To calculate the tunneling matrix element Tersoff and Hamann [21] assumed a locally spherical tip with radius R at \vec{r}_0 and a minimum distance d to the sample surface as depicted in Fig. 2.2a on the left-hand side. They have furthermore considered the simplification of the tunneling current I_T in the limit of low temperatures and small bias voltages ($V \approx 10$ meV), which allows to reduce Eq. (2.2) to [21]:

$$I_T = \frac{2\pi e^2 V}{\hbar} \sum_{\mu\nu} |M_{\mu,\nu}|^2 \delta(E_\nu - E_F) \delta(E_\mu - E_F). \quad (2.4)$$

With the assumption of a s-type tip wave function, the tunneling current can be further simplified to:

$$I_T \propto n_T(E_F) \cdot V \cdot e^{2R\kappa} \underbrace{\sum_{\nu} |\Psi_\nu(\vec{r}_0)|^2}_{n_S(E_F)} \delta(E_\nu - E_F). \quad (2.5)$$

Here κ is the decay rate from Eq. (2.1), $n_T(E_F)$ and $n_S(E_F)$ are LODS at the Fermi level E_F of the tip and sample, respectively. Therefore, the constant current STM image at low bias voltages and for a tip with locally spherical symmetry represents contour maps of constant LODS of the sample.

STM images for metallic graphene lattices were taken at low bias voltages. However, in this thesis also the semiconducting SiC substrate and ZLG are investigated, where several volts have to be applied. Thus, the simple interpretation of Tersoff and Hamann is no longer valid.

Using the Wentzel-Kramers-Brillouin (WKB) theory the tunneling current for finite bias can be expressed by [19]:

$$I_T \propto n_T(\pm eV \mp \epsilon) \cdot n_S(\epsilon) \cdot T(\epsilon, eV) d\epsilon. \quad (2.6)$$

Here, the transmission probability T is given by:

$$T(\epsilon, eV) = \exp \left[-2(d + R) \sqrt{\frac{2m}{\hbar^2} \left(\frac{\Phi_T + \Phi_S}{2} + \frac{eV}{2} - \epsilon \right)} \right], \quad (2.7)$$

where ϵ is the energy with respect to the Fermi level E_F , m the electron mass and Φ_T and Φ_S denote the work function of the tip and sample, respectively. Furthermore, the transmission probability T depends on the bias voltage V applied to the tip. The tunneling of the electrons for a positive (negative) bias is depicted in Fig. 2.2c (d), where a constant DOS of the tip is assumed. For $V > 0$ electrons tunnel from occupied tip states to sample states above the Fermi level. $V < 0$ ensures the electrons to tunnel from occupied sample states to unoccupied tip states. As indicated with red arrows the contribution to the tunneling current for positive bias increases with increasing state energy in the range from E_F to $E_F + eV$. For a negative bias, the largest contribution stems from sample states at the Fermi level.

2.2.2 Inelastic mean free path

LEED and PES make use of the scattering and emission of electrons at and from the sample surface, respectively. Therefore, the inelastic mean free path (IMPF) of the electrons plays an important role. Electrons from deep inside the bulk have a higher probability to scatter on their way to the surface, than electrons originating near the surface. They lose energy and therefore, their information of the initial state. In this thesis, LEED as well as ARPES operate in an energy range of 10-100 eV. In this range, the IMFP has a minimum, which is depicted in the universal curve in Fig. 2.2.2. Here the energy dependence of the IMPF is displayed. Due to the similar behavior of the electron density, the curve is

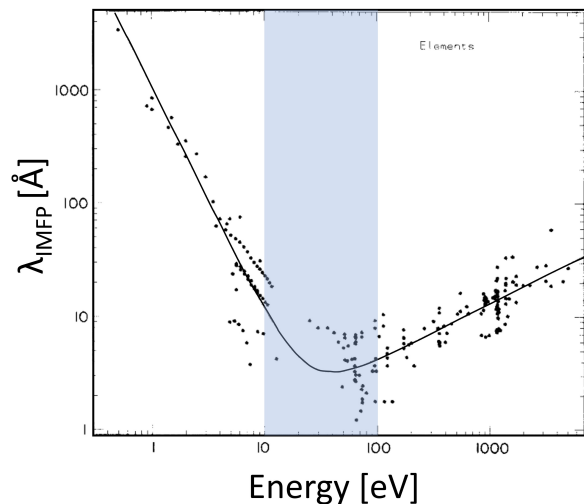


Fig. 2.3: Universal curve for the mean free path λ_{IMPF} of electrons in various materials. The blue area represents the energy range of the experiments performed in this work, which are highly surface-sensitive. Taken from Ref. [22].

universal for many materials [22]. Since the measurements are in the energy range around the minimum of the IMPF, these methods are highly surface-sensitive. That means only a few layers can be investigated, which, however, is sufficient for the study of 2D materials.

2.2.3 Low-energy electron diffraction

In 1927 Davisson and Germer first proved, that electrons can be diffracted, due to their wave-like behavior [23]. Prior to this, Laue realized the first diffraction experiment using X-rays in 1912 [24]. One year later Bragg succeeded with the first bulk structure analysis [25]. Nevertheless, it took until 1970 before the first structure analysis with LEED was performed [26]. Using the wave nature of electrons, the electron beam can be seen as a plane wave with the wavelength

$$\lambda = \frac{h}{\sqrt{2mE_{\text{kin}}}}, \quad (2.8)$$

as postulated by de Broglie, where E_{kin} is the kinetic energy of the electrons. Due to the before mentioned energy range for LEED, the electron wavelength with a few ångström, is in the same order of magnitude as atomic distances. The constructive interference of the diffracted electrons provides information on the long-range order of the sample surface [27].

LEED instrumentation

The experimental setup is depicted in Fig. 2.4. It consists of an electron gun, a fluorescence screen and three grids. The sample is placed in front of the setup. In this configuration, electrons can hit the surface in normal incidence. The electrons are produced by the thermal emission of a LaB₆ coated material. This material is chosen, due to its low work function [26]. The beam is focused by a Wehnelt cylinder and afterward collimated by an electrostatic lens. Electrons with an energy of E_e leave the electron gun through the drift tube into a field-free space, because the drift tube, the first grid and the sample are grounded [26]. After the electrons got elastically or inelastically scattered at the samples surface they head towards the screen. Due to the negative potential of the second grid, inelastically scattered electrons with an energy $E < E_e$ are filtered. Between the grounded third grid and the screen a voltage of the order of 5 kV is applied. The electrical field accelerates the electrons onto the fluorescence screen, where a diffraction pattern is created. This LEED pattern can be photographed by a conventional camera [28, 27].

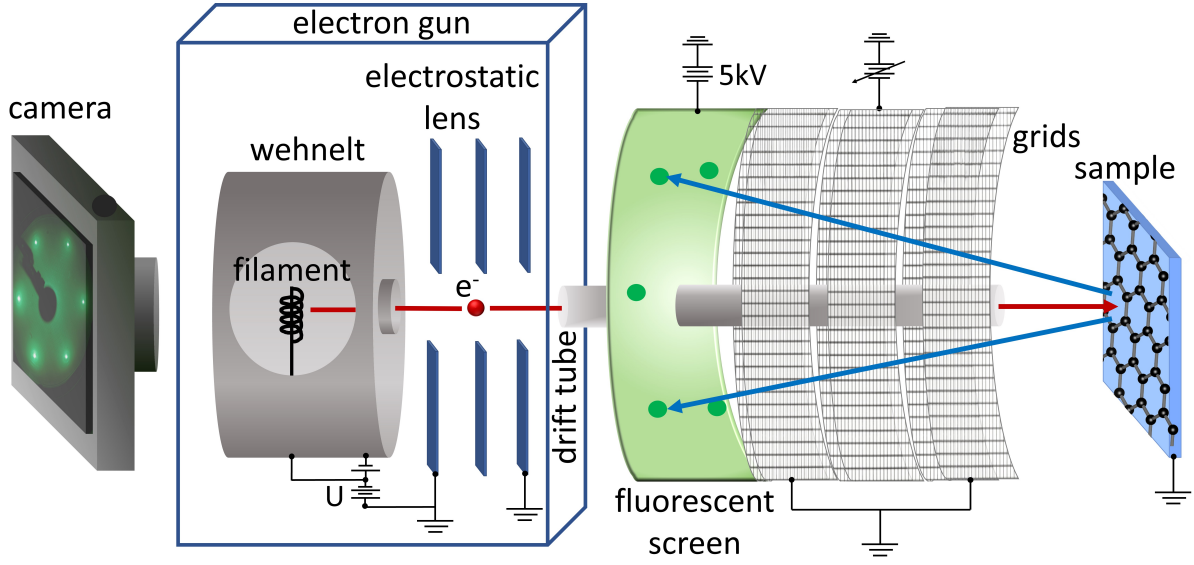


Fig. 2.4: Conventional LEED setup. The electron gun accelerates electrons onto a sample surface. Only elastic scattered electrons (blue) can pass the three grids and fluorescence at the screen. The diffraction spots are captured with a camera. Adapted from Ref. [27].

Diffraction theory

As evident from the universal curve, LEED is highly surface sensitive and it is assumed, that the electrons only scatter at the first atomic layer. Thus, a sufficient description of the 2D lattice requires only the real space vectors $\vec{a}_{1,2}$, which span one of the five Bravais lattices. Because the diffraction pattern corresponds to the Fourier transformation of the real space atomic positions, the further consideration is made in the reciprocal space. The transformation of the real space vectors to the reciprocal space vectors $\vec{b}_{1,2}$ can be done using the relationship

$$\vec{a}_i \cdot \vec{b}_j = 2\pi\delta_{ij}, \quad (2.9)$$

where δ_{ij} is the Kronecker delta. The linear combination of the vectors $\vec{b}_{1,2}$ fully describe the reciprocal lattice with its reciprocal vectors [28]

$$\vec{K}_{hk} = h\vec{b}_1 + k\vec{b}_2, \quad (2.10)$$

where h, k are integers. Due to the wave character of electrons, the incoming electron beam can be described by the wave vector \vec{k}_i and scattered electrons have the wave vector \vec{k}_f . Due to the second grid in Fig. 2.4 only elastically scattered electrons can contribute to the LEED pattern and therefore the absolute value of the wave vector is $|\vec{k}_i| = |\vec{k}_f|$. Constructive interference for diffracted electrons occurs according to the Laue condition,

when the difference of the incident and scattered wave vectors $\vec{k}_i - \vec{k}_f$ is equal to the reciprocal lattice vector \vec{K}_{hk} [27]

$$\vec{k}_i - \vec{k}_f = \vec{K}_{\text{hk}}. \quad (2.11)$$

The diffraction maxima can be detected on the screen. They provide information about the atomic arrangements and periodicity of a 2D surface, which is depicted for a honeycomb lattice in Fig. 2.4.

2.2.4 Photoelectron spectroscopy

To study the electronic properties as well as the energy-momentum relation of 2D materials, PES is a widely used method [29, 30]. PES is based on the photoelectric effect, which was discovered by Hertz [31] and Hallwachs [32] in 1887. Their experiments dealt with the interaction of light with solids, but could not be theoretically described until 1905 when Einstein published his famous work [29, 33]. In this work, he introduced the concepts of the quantum nature of light. He claimed that light is quantized and consists of photons with the energy $E_{\text{ph}} = h\nu$. If a solid is exposed to light electrons can leave the material. The kinetic energy E_{kin} of the photoelectron is given by the energy conservation law:

$$E_{\text{kin}} = h\nu - \Phi - |E_{\text{bin}}|, \quad (2.12)$$

where Φ is the material specific work function and E_{bin} the binding energy of the electron in the solid. Making use of this simple effect, a lot of groups pioneered the field of PES. Among many other techniques, Spicer was the first who realized an ultraviolet photoemission (UPS) valence spectrum [34]. Siegbahn later developed the X-ray photoelectron spectroscopy (XPS) [29, 35]. The basic principle of PES is depicted in Fig. 2.5a. Occupied states can be excited by light, if the energy E_{ph} is greater than the binding energy E_{bin} and the work function Φ of the material. Since UPS and XPS utilize different photon energies $h\nu$, the valence band states and the core level states can be investigated, respectively [29].

Theoretical consideration of photoelectron spectroscopy

In reality, the excitation of the photoelectron is much more complicated than shown in Fig. 2.5a. The transition probability w_{fi} from a N -electron ground state Ψ_i into a final state Ψ_f , due to an optical excitation is described by Fermi's golden rule [36]:

$$w_{\text{fi}} = \frac{2\pi}{\hbar} |\langle \Psi_f^N | H_{\text{int}} | \Psi_i^N \rangle|^2 \delta(E_f^N - E_i^N - h\nu). \quad (2.13)$$

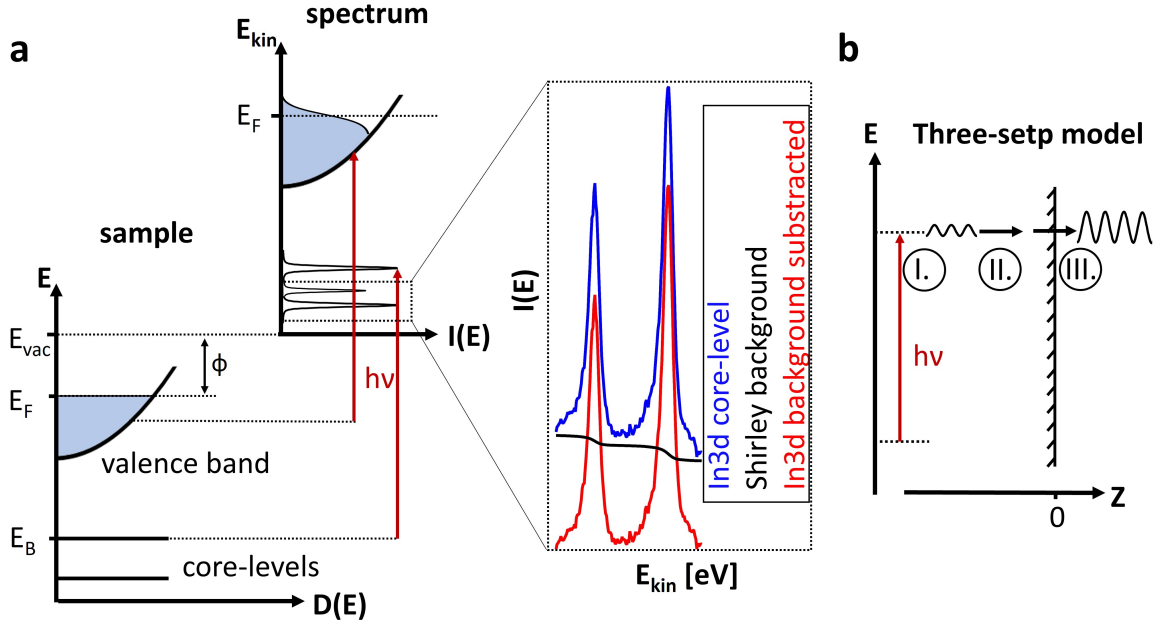


Fig. 2.5: **a** Photoemission process. A photon with energy $h\nu$ excites an electron from the core level or the valence band, which can then be measured in terms of the intensity as a function of their kinetic energy. Inset: In 3d core level peak (blue), the Shirley background (black) and the background corrected data (red). **b** Three-step model description of the photoemission process. Step 1: Excitation of an electron into a final state. Step 2: Electron travels through the samples surface. Step 3: Transmission into the vacuum. Adapted from Ref. [36].

The second term ensures energy conservation, because it only provides a contribution to w_{fi} , if the difference between the initial state $E_i^N = E_i^{N-1} - E_B^k$ and final state $E_f^N = E_f^{N-1} - E_{kin}$ of the N electron system is equal to the photon energy E_{ph} . Here E_{bin}^k is the binding energy of the photoelectron and E_{kin} its kinetic energy [36]. Since the sample is in an electromagnetic field with vector potential \vec{A} , the unperturbed Hamiltonian $H_0 = p^2/2m_e + eV(\vec{r})$ is extended, due to the transformation of the momentum operator $\vec{p} \rightarrow \vec{p} - \frac{e}{c}\vec{A}$. The Hamiltonian operator is then given by [29]:

$$H = \underbrace{\frac{p^2}{2m}}_{H_0} + \underbrace{\frac{e}{2mc}(\vec{A} \cdot \vec{p} + \vec{p} \cdot \vec{A}) + \frac{e^2}{2mc^2}A^2}_{H_{int}}. \quad (2.14)$$

The perturbation operator H_{int} can be simplified, when neglecting non-linear processes (term $\propto A^2$) and assuming the long wavelength limit without surface effects ($\text{div}\vec{A}=0$). The Hamiltonian can be expressed by [29]:

$$H_{int} = \frac{e}{mc}\vec{A} \cdot \vec{p}. \quad (2.15)$$

For a correct description of the photoelectron being removed by a photon and its detection afterwards, the perturbation operator must also consider surface resonances in addition to bulk, surface and evanescent states in a coherent process [36]. This approach is called the One-step model. It is quite complicated and the simpler Three-step model is here sufficient to describe PES. As the name suggests, the photoemission process is divided into three independent steps:

- (I) Optical excitation of an electron from the initial to the final bulk state.
- (II) Propagation of the excited electron to the surface.
- (III) Exit of the photoelectron into the vacuum.

Step (I) provides all the information on the electronic structure of the sample and is discussed below. Step (II) takes the IMPF into account and gives the probability, for the electron reaching the surface without losing information, due to scattering processes. Lastly, step (III) is the process of the transmission of an electron into the vacuum. The product of all three terms provides the total photoemission intensity. The transition probability in step (I) can be calculated using Eq. (2.13). When removing the photoelectron, the $(N - 1)$ -electron system will relax, making the system far from trivial [36]. Therefore, this electron-interacting system can be simplified by using the Sudden Approximation (SA). Here it is assumed, that the photoelectron is decoupled from the $(N - 1)$ -electron system and all the interactions are neglected. The decoupled final state $|\Psi_f\rangle = |\Psi_{\vec{k},s}\rangle$ can then be written as:

$$|\Psi_{\vec{k},s}\rangle = |\vec{k}; N - 1, s\rangle \xrightarrow{\text{SA}} c_{\vec{k},s}^\dagger |N - 1, s\rangle \quad (2.16)$$

with the creation operator $c_{\vec{k},s}^\dagger$ for the photoelectron with momentum \vec{k} and the remaining $(N - 1)$ -electron system with all its possible excitations s of the final state [29]. The photoelectron current $I_{\vec{k}}(h\nu) = \sum_{\vec{k}'} w_{\vec{k},\vec{k}'}$, with $w_{\vec{k},\vec{k}'}$ from Eq. (2.13), can be calculated as the sum over all possible states \vec{k}' [29]:

$$I_{\vec{k}}(h\nu) = \frac{2\pi}{\hbar} \sum_{\vec{k}'} |\langle \Psi_{\vec{k}} | H_{\text{int}} | \Psi_{\vec{k}'} \rangle|^2 A_{\vec{k}'}^{\leq}(E_{\text{kin},\vec{k}} - h\nu). \quad (2.17)$$

Here, the transition probability from state $|\Psi_{\vec{k}',s}\rangle$ into the state $|\Psi_{\vec{k},s}\rangle$ of a single electron is described by the one-particle spectral function

$$A_{\vec{k}'}^{\leq}(h\nu) = \sum_s |\langle N - 1, s | c_{\vec{k}'} | N \rangle|^2 \cdot \delta(h\nu - E_s). \quad (2.18)$$

For a single electron with many-body interactions, the one-electron Green's function $G_{\vec{k}'}(\omega)$ can describe the system. In the Dyson equation

$$G_{\vec{k}'}(\omega) = \frac{1}{\omega - E_{\text{kin},\vec{k}'} - \Sigma_{\vec{k}'}(\omega)} \quad (2.19)$$

the complex self-energy $\Sigma_{\vec{k}'}(\omega) = \text{Re} \Sigma_{\vec{k}'}(\omega) + i \text{Im} \Sigma_{\vec{k}'}(\omega)$ includes electron-electron and electron-phonon interactions. Due to the connection of the one-particle Green's function to the spectral function $A_{\vec{k}'}^<(\omega) = -\frac{1}{\pi} \text{Im} G_{\vec{k}'}(\omega) \cdot f(\omega, T)$, with the Fermi-Dirac distribution $f(\omega, T)$, Eq. (2.18) can be expressed by [29]:

$$A_{\vec{k}'}^<(\omega) = -\frac{1}{\pi} \frac{\text{Im} \Sigma_{\vec{k}'}(\omega)}{[\omega - E_{\text{kin},\vec{k}'} - \text{Re} \Sigma_{\vec{k}'}(\omega)]^2 + [\text{Im} \Sigma_{\vec{k}'}(\omega)]^2}. \quad (2.20)$$

This expression gives the photoemission intensity with the consideration of many particle effects. These effects lead to a lifetime broadening (coded in the imaginary part of the self-energy) and to the energy renormalization (real part of self-energy).

Angle-resolved photoelectron spectroscopy

ARPES measures not only the kinetic energy of the photoelectron but also its momentum. Therefore the energy dispersion $E(\vec{k})$ of the solid can be imaged. After the photoelectron is removed from the material, it passes the electrostatic lenses, which collect, decelerate or accelerate, depending on E_{kin} of the electrons, and focus the electrons on the entrance slit. The photoelectron then reaches the hemispherical analyzer at an angle θ relative to the surface normal. This is depicted in Fig. 2.6a. Between the two hemispherical electrodes, a voltage is applied. This enables, that only electrons with a defined pass energy E_{pass} can pass the analyzer. They are then collected at the microchannel plate (MCP). It consists of millions of thin capillaries, thus acting as a secondary-electron multiplier. In combination with a phosphor fluorescent screen and a charge-coupled device (CCD) camera, 2D imaging is practicable. By adapting the voltages of the hemispherical electrodes, electrons with different energies can be detected and an energy spectrum is obtained. The energy resolution ΔE of the analyzer

$$\Delta E = E_{\text{pass}} \left(\frac{2w}{R_1 + R_2} + \frac{\alpha^2}{4} \right) \quad (2.21)$$

is given by the electrodes radii R_1 and R_2 , the entrance slit width w and the acceptance angle α [36].

With the out-of-plane angle θ and the azimuthal in-plane angle ϕ , the momentum \vec{k} of the photoelectron can be fully described, as illustrated in Fig. 2.6b. The electron momentum

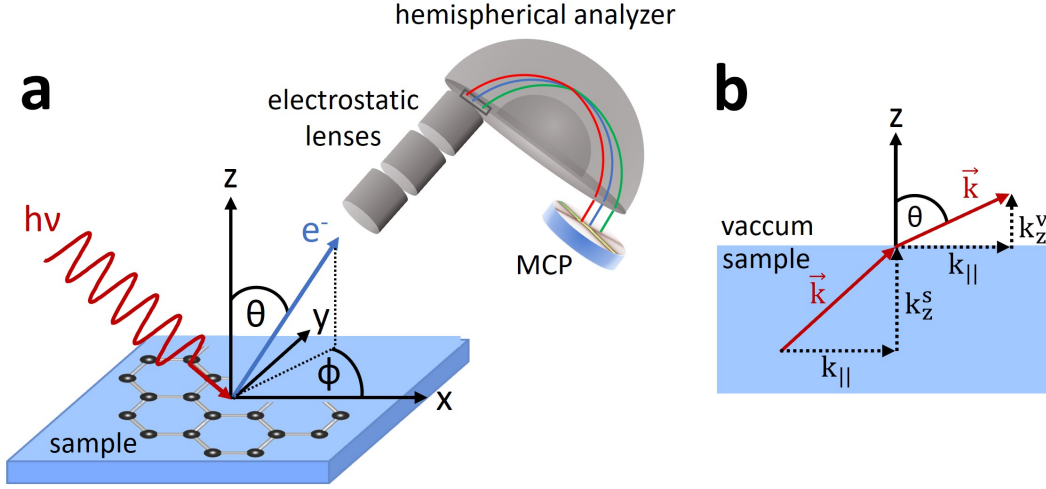


Fig. 2.6: **a** Schematic of an ARPES measurement. The emitted electrons are focused on the entrance slit of a hemispherical analyzer by the electrostatic lens system. After passing the analyzer with its electric field, the electrons are collected at the detector. **b** Illustration of the photoemission. While the wave vector component parallel to the surface k_{\parallel} is conserved, the perpendicular component k_z changes after the electron leaves the solid. Adapted from Ref. [36].

$|\vec{k}| = \frac{1}{\hbar}\sqrt{2mE_{\text{kin}}}$ is now divided into the perpendicular $|\vec{k}_z|$ and the parallel component

$$|\vec{k}_{\parallel}| = \frac{1}{\hbar}\sqrt{2mE_{\text{kin}}}\sin(\theta) \quad (2.22)$$

relative to the solid surface. At step (III) of the Three-step model, the photoelectron penetrates through the samples surface into the vacuum. Here the particle experiences a potential difference. When comparing the perpendicular component of the momentum inside the solid k_z^s with the one of the vacuum k_z^v in Fig. 2.6b, it can be seen, that the perpendicular component of the momentum is not conserved. Parallel to the surface the potential is periodic and differs only by a reciprocal lattice vector K_{hk} . Hence, the parallel component of the momentum k_{\parallel} is preserved. Since only 2D materials are investigated in this work, the k_z component is not of importance, but the interested reader will find an approach in Ref. [30]. The surface energy dispersions $E(k_{\parallel})$ shown in this work were taken with a PHOIBOS 100 Specs analyzer with a resolution of nominal 5 meV, in reality around 10-15 meV. A He discharge lamp is used with the He I_{α} and II_{α} line with a photon energy of 21.2 eV and 40.8 eV, respectively. High-resolution ARPES measurements with various photon energies were taken at the Diamond Light Source synchrotron at end station I05 under the two proposal IDs SI26860-1 and SI30583-1.

X-ray photoelectron spectroscopy

For XPS measurements the surface is irradiated with soft X-rays with the energies in the order of 0.1-10 keV. In this work, the Al K_α line with a corresponding photon energy of $h\nu = 1486.6$ eV is used for the excitation [37]. At this photon energies, XPS mainly probes the core levels, as shown in Fig. 2.5a. The sharp core level peaks are located at defined binding energies, which are characteristic for a respective chemical composition [38]. XPS therefore provides information about the atomic species of the surface. This is an important tool for the growth of a new system, like the graphene/indium/SiC, and in particular the chemical analysis upon oxygen exposure. The XPS line shapes in Fig. 2.5a can be described with a Voigt function, due to its convolution of a Lorentzian (lifetime broadening) and a Gaussian (instrumental broadening) contribution [39]. However, the intensity of the XPS signal $I_0 \propto N_A \cdot J \cdot \sigma_{h\nu} \cdot \lambda(E_{\text{kin}}) \cdot T(E_{\text{kin}})$ is not only proportional to the density of occupied states N_A , but also depends on the photon flux J , the photoionization cross section $\sigma_{h\nu}$, the inelastic mean free path $\lambda(E_{\text{kin}})$ and the analyzer transmission function $T(E_{\text{kin}})$ [30]. Step (II) in the Three-step model indicates the travel of the photoelectron to the surface. In this process, some of the electrons are scattered and still contribute to the signal. Therefore, the spectrum not only shows the elastically scattered photoelectrons, but also a background created by secondary electrons, which has to be subtracted from the measured spectrum. In this thesis, the background correction is done by using the model proposed by Shirley [40]. He developed an iterative process, where the background is subtracted in the energy range from E_1 to E_2 :

$$I_c^{n+1}(E) = I_m(E) - I_m(E_1) \left(\frac{\int_E^{E_2} I_c^n(E') dE'}{\int_{E_1}^{E_2} I_c^n(E') dE'} \right), \quad (2.23)$$

where $I_c^{n+1}(E)$ is the corrected spectrum after n iterations and $I_m(E)$ is the measured spectrum. The Shirley background, the measured and the corrected spectrum for the In 3d doublet core level peak is depicted in the inset in Fig. 2.5a.

Chapter 3

Graphene on silicon carbide

Before indium can be intercalated into the SiC/graphene interface, the physics of graphene need to be understood. Here, the different fabrication techniques as well as the electronic properties of the mono- and bilayer graphene are reviewed. The recipes for the growth of three different epitaxial graphene coverages on top of a 4H-SiC substrate are presented, followed by an investigation using LEED, STM and PES.

3.1 Physics of graphene

3.1.1 Electronic properties of graphene

Graphene is a monolayer of carbon atoms that arrange in a honeycomb crystal structure. It can be classified by two triangular Bravais sublattices with the lattice vectors

$$\vec{a}_1 = \frac{a}{2}(3, \sqrt{3}), \quad \vec{a}_2 = \frac{a}{2}(3, -\sqrt{3}), \quad (3.1)$$

where $a \approx 1.42 \text{ \AA}$ is the distance between nearest neighbor carbon atoms [41]. In Fig. 3.1a the two graphene sublattices (red and green) and the unit cell with its lattice vectors are shown. The Brillouin zone of graphene including the reciprocal lattice vectors

$$\vec{b}_1 = \frac{2\pi}{3a}(1, \sqrt{3}), \quad \vec{b}_2 = \frac{2\pi}{3a}(1, -\sqrt{3}), \quad (3.2)$$

as well as some high-symmetry points are depicted in Fig. 3.1b. As shown later the K and K' points are of great importance in graphene, wherein both correspond to one sublattice respectively. The hexagonal structure of graphene originates from the sp^2 hybridization, where the $2p_x$ and $2p_y$ orbitals as well as the $2s$ orbital form the σ -bonding [42]. These σ -bands occupy the shell fully and therefore do not contribute to electronic conduction [43, 44]. The p_z -orbitals though form π -bonds perpendicular to the graphene lattice as

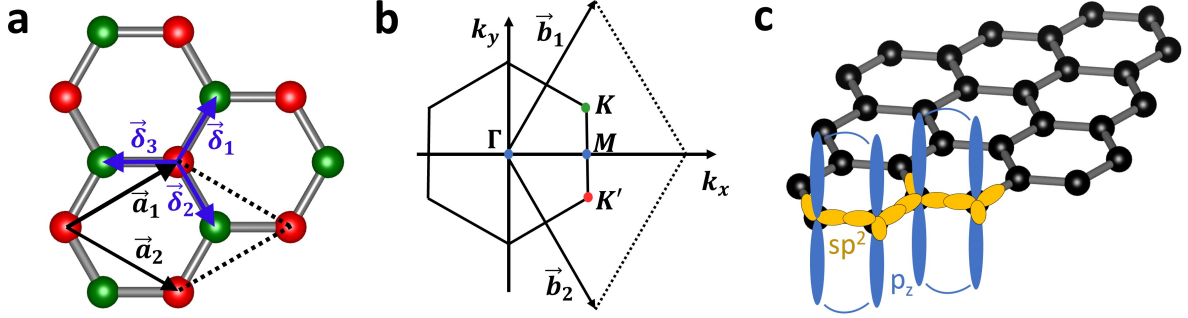


Fig. 3.1: **a** The honeycomb graphene lattice consists of two identical triangular sublattices (red and green). The unit cell is defined by the vectors $\vec{a}_{1,2}$. **b** The Brillouin zone with its reciprocal vectors $\vec{b}_{1,2}$ including high symmetry points. Adapted from Ref. [41]. **c** sp^2 -hybridized C atoms form the σ -bonds and out-of-plane p_z -orbitals the π -bonds. Adapted from Ref. [43].

sketched in Fig. 3.1c.

The monolayer graphene band structure was first calculated by Wallace in 1947, using the tight binding approximation [45]. Here only the π -states and the nearest-neighbor coupling are considered. That means, that there is no interaction within one sublattice. In this simplified case the Hamiltonian is described by

$$\hat{H}(\vec{k}) = \begin{pmatrix} 0 & tS(\vec{k}) \\ tS(\vec{k}) & 0 \end{pmatrix}, \quad (3.3)$$

where t is the hopping parameter, \vec{k} the wave vector and

$$S(\vec{k}) = \sum_{i=1}^3 e^{i\vec{k}\vec{\delta}_i} = 2e^{\frac{ik_x a}{2}} \cos\left(\frac{\sqrt{3}ak_y}{2}\right) + e^{-ik_x a} \quad (3.4)$$

is the sum over each of the three nearest neighbours $\vec{\delta}_i$ [46]. The energy dispersion resulting from this Hamiltonian is

$$E(\vec{k}) = \pm t|S(\vec{k})| = \pm t \sqrt{1 + 4 \cos\left(\frac{1}{2}ak_x\right) \cos\left(\frac{\sqrt{3}}{2}ak_y\right) + 4 \cos^2\left(\frac{1}{2}ak_x\right)}, \quad (3.5)$$

where the positive (negative) solution corresponds to the conduction (valence) band. In Fig. 3.2a, the band structure of graphene, calculated for $t=3$ eV, is depicted. Graphene is a gapless semiconductor, as the π - and π^* -bands are touching at the Dirac points (K and K'). The gapless state itself is not the only interesting feature of the graphene band structure. In the inset in Fig. 3.2a the linear behavior of the π -bands near the Dirac points is observed. Wallace first calculated the linear energy dispersion around the K

point with $\vec{q} = \vec{k} - \vec{K}$ to be

$$E_{\pm}(\vec{q}) = \pm \hbar v_F |\vec{q}|, \quad (3.6)$$

where $v_F = \frac{3ta}{2} = 1.0 \cdot 10^6 \frac{m}{s}$ is the Fermi velocity [41, 45]. Such linear dispersions are otherwise only known for relativistic particles like e.g., photons. Thus, the electrons in graphene behave like relativistic particles without a mass.

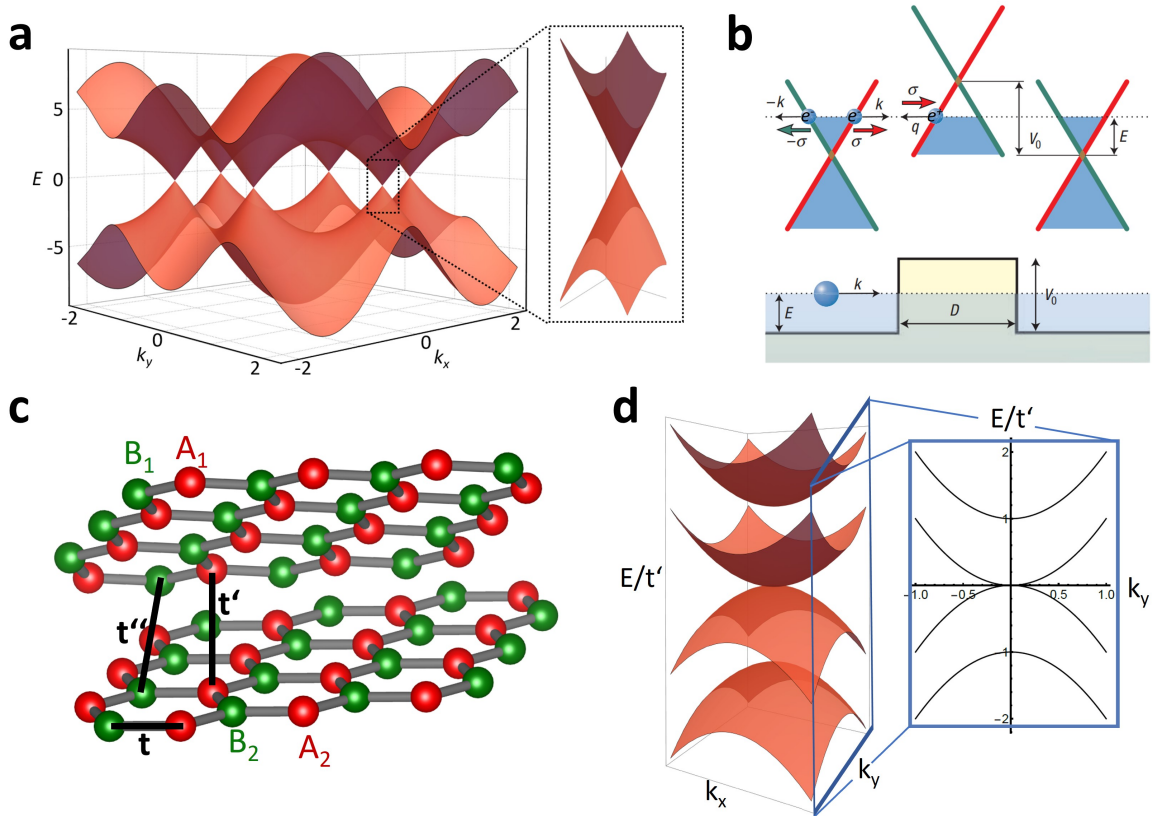


Fig. 3.2: **a** Energy dispersion for the graphene lattice with $t=3\text{ eV}$. Calculated using *Mathematica*. **b** Tunnelling through a potential step V_0 at the graphene Dirac points. The red (green) arrows indicate the pseudospin σ of the particle at the sublattice A (B). The protection of the pseudospin to the momentum results in perfect tunneling through a potential barrier. Taken from Ref. [47]. **c** Bilayer graphene with additional hopping parameters t' , t'' and **d** its energy dispersion around the Dirac point.

Quantum electrodynamics in graphene

The linear energy dispersion of graphene leads to a further study of novel effects. This 2D material is used to experimentally enable quantum relativistic phenomena and is also called “CERN on one’s desk“ [46]. In graphene, the two sublattices can be seen as the pendant to the spin in Dirac fermions and therefore, a pseudospin σ is defined for graphene.

This pseudospin leads to an additional degree of freedom for the electrons in the 2D material [44, 46]. Fig. 3.2b displays the perfect tunneling and the forbidden backscattering of quasiparticles in the 2D material. The two branches of the linear dispersion (red and green) stem from the two sublattices. When the Fermi level is above the crossing point, like for the first cone, the quasiparticle behavior is electron-like. But when the Fermi level is below the Dirac point the charge carriers are hole-like. The red and green pseudospin vectors correspond to the respective sublattice branch. Electrons that propagate to the right (k) and holes that propagate to the left (q) originate from the same branch and have the same pseudospin σ [47]. The pseudospin is therefore parallel (antiparallel) to the direction of motion for electrons (holes) [47]. Nevertheless, the quasiparticles of the same branch have the same chirality, which is formally a projection of pseudospin on the direction of motion, which is positive and negative for electrons and holes, respectively. [43, 47]. Due to the conservation of the pseudospin, an electron from the red branch can scatter only into the same red branch. This can be seen when including a potential step V_0 . The right-moving electron cannot be scattered in a left-moving electron state, but in a right-moving hole state, which implies perfect tunneling. This is also in analogy to the Dirac fermions in quantum electrodynamics and is called Klein tunneling [43, 46, 47].

The already mentioned properties make graphene very interesting and to one of the most studied systems so far. Furthermore, the half-integer QHE was discovered in graphene, where the Hall conductivity σ of the plateaus is given by [48]:

$$\sigma = \left(i + \frac{1}{2}\right) \cdot g \frac{e^2}{h}. \quad (3.7)$$

Here g takes the spin and valley degeneration into account and i is the plateau number. This QHE in the 2D material could be also observed at room temperature [49]. Besides the discovery of the fractional QHE in graphene [50], the 2D material is also very interesting to study, due to a mobility up to $200.000 \frac{cm^2}{Vs}$ [51], a breaking strength of $42 \frac{N}{m}$ [52] or the discovered properties of two stacked graphene lattices.

Bilayer graphene

The crystal structure of bilayer graphene is shown in Fig. 3.2c. Two graphene lattices are stacked above each other in the Bernal stacking type, which is also known as the ABAB stacking [53, 54]. To calculate the band structure for the bilayer graphene an additional hopping parameter is required. While the parameter t is still the nearest neighbor hopping between the two graphene sublattices (A_2, B_2), $t'=0.4$ eV indicates the coupling between the same sublattices from the two different carbon monolayers (A_1, A_2) [55]. Due to the Bernal stacking the coupling between the sublattices B_1 and B_2 is neglectable [41, 46].

The Hamiltonian for this simplified case is given by

$$\hat{H}(\vec{p}) = \begin{pmatrix} 0 & tS(\vec{k}) & t' & 0 \\ tS^*(\vec{k}) & 0 & 0 & 0 \\ t' & 0 & 0 & tS(\vec{k}) \\ 0 & 0 & tS(\vec{k}) & 0 \end{pmatrix}, \quad (3.8)$$

with $S(\vec{k})$ from Eq. (3.4). The eigenvalues and therefore the energy dispersion can be calculated to be

$$E(\vec{k}) = \pm \frac{1}{2}t' \pm \sqrt{\frac{1}{4}(t')^2 + t^2|S(\vec{k})|^2}. \quad (3.9)$$

Near the Dirac points, this expression can be simplified to

$$E(\vec{k}) \approx \pm \frac{t^2|S(\vec{k})|^2}{t'} \approx \pm \frac{\hbar^2 k^2}{2m^*}, \quad (3.10)$$

where $m^*=0.028 m_e$ is the effective mass [46, 56]. The energy dispersion near the K and K' points is depicted in Fig. 3.2d. The second graphene lattice changes the band structure enormously compared to the monolayer case. Besides the two additional π -bands starting at $\pm t$ [57], the band structure still corresponds to a gapless semiconductor. But other than in graphene, the dispersion is parabolic near the Dirac points.

The probably most known phenomenon of bilayer graphene is the superconductivity for twisted graphene layers [58]. In this system, the two graphene lattices are rotated by $\theta = 1.1^\circ$ with respect to each other. Unfortunately, this effect could only be observed at temperatures below $T=1.7$ K. Nevertheless, it can help to understand the mechanism of superconductivity [58]. A more detailed band structure calculation of the mono- and bilayer graphene, as well as the justifications for the simplifications done in this section, can be found in Ref. [46].

3.1.2 Epitaxial graphene

Graphene can be produced in a variety of ways. In 2004, graphene was for the first time isolated by mechanical exfoliation by Geim and Novoselov. Here a sticky tape is used to exfoliate a few graphene layers from a three-dimensional highly oriented pyrolytic graphite crystal. By repeating this process and subsequently applying it to a substrate a monolayer graphene flake can be achieved [60, 61]. However, this technique is not suitable for device applications, due to the small size of the graphene flakes and its time-consuming process. Another popular way of producing graphene is chemical vapor deposition (CVD) [62]. A copper substrate, acting as a catalyst, is put together with methane inside a reaction

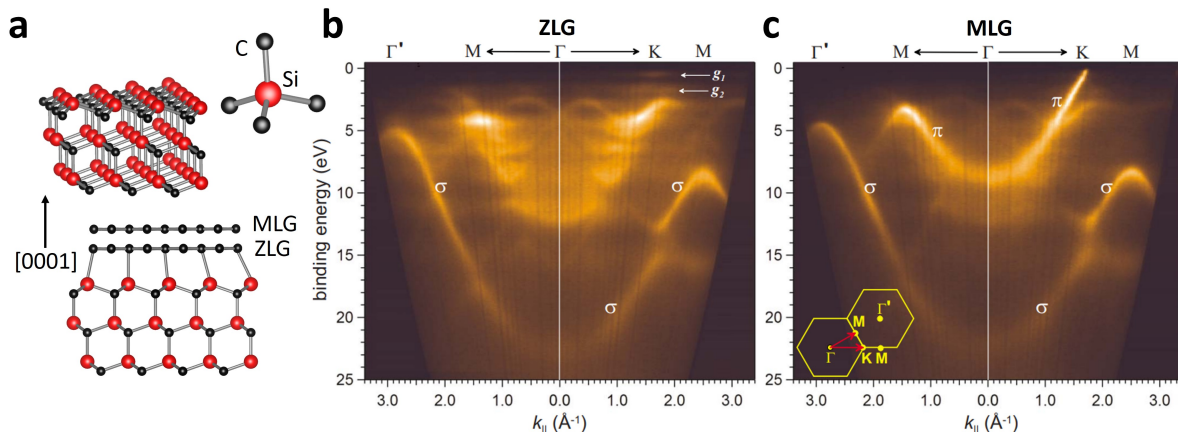


Fig. 3.3: **a** The bare 4H-SiC(0001) substrate before (top) and after post-annealing, where a ZLG and a monolayer graphene are formed (bottom). **a,b** ARPES band map for **b** the ZLG with two smeared states at the K point indicated as g_1 and g_2 and **c** the monolayer graphene with the linear π -bands. Taken from Ref. [59]

chamber. During heating, the carbon atoms from the methane are trapped on the Cu surface, while the remaining hydrogen atoms will bond and form molecular hydrogen. The carbon atoms on the other side will form a single-layer of graphene [62]. This method was extended to many other metallic substrates, like Ni(111)[63, 64], Ru(0001)[64] and Pt(111)[65]. Its advantage towards exfoliation is that graphene can be produced over a large area. However, graphene is grown on metallic substrates, which poses a problem for potential applications.

In this work, graphene was grown on 4H-SiC(0001) substrates, which have a lattice constant of $a_{\text{SiC}} = 3.074 \text{ \AA}$ [41, 66]. These substrates are semiconductors with a gap of 3.2 eV at room temperature, making them promising templates for device applications [67]. In Fig. 3.3a the SiC structure is shown. The stoichiometric ratio of the carbon and the silicon atoms is 1:1. The atoms form a tetrahedral configuration, where the Si (C) atoms are surrounded by four C (Si) atoms [44]. As depicted in Fig. 3.3a, the substrate has two different sides. While the top side is the Si-terminated face of the 4H-SiC, the bottom side is C-terminated. In this work, graphene is grown on the Si-face of the SiC substrate. At high temperatures the epitaxial graphene can be grown based on thermal decomposition of the SiC [59]. Due to the high temperatures, the silicon sublimates and the carbon atoms will rearrange in a graphene-like configuration, where the (13×13) graphene cell aligns with the $(6\sqrt{3} \times 6\sqrt{3})R30^\circ$ SiC periodicity [68]. This graphitic layer owns different electronic properties, but its topography is reminiscent of graphene. Thus, it is also called zero-layer graphene (ZLG). By further substrate annealing, a new ZLG in the "old" ZLG/SiC interface is formed. This second layer decouples the previous ZLG from the SiC substrate, which relaxes and transforms to quasi-freestanding monolayer graphene [61].

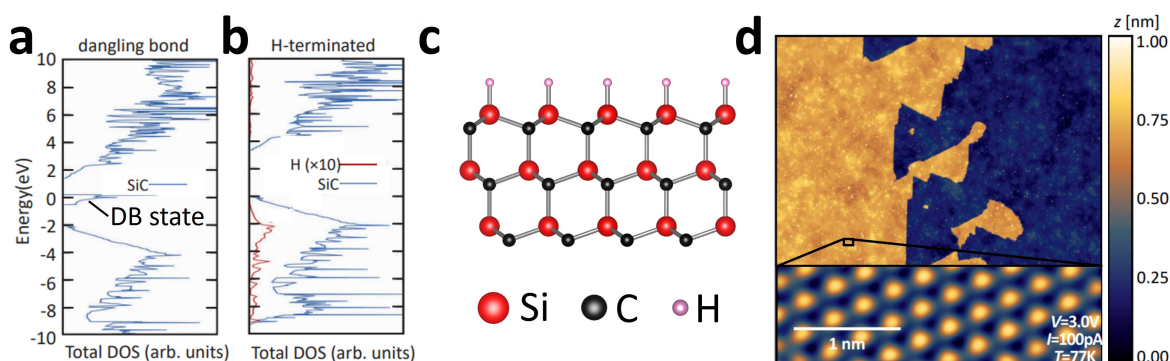


Fig. 3.4: **a,b** DFT calculation of the total DOS for a six-layer SiC substrate with dangling bonds **a** without and **b** with hydrogen passivation. **c** Structural model of the H-passivated 4H-SiC substrate. **d** STM image from a large-scale ultra-flat surface with an atomic resolution in the inset, showing the topmost Si atoms. Taken from Ref. [69]

The band structure measured by ARPES for the zero and monolayer can be seen in Fig. 3.3b and c. While the monolayer has linear π -bands, the ZLG shows only two smeared out insulating states at the graphene K point. Therefore the ZLG cannot contribute to charge carrier transport [68].

3.2 Growth of epitaxial graphene

The epitaxial graphene results should be reproduced and investigated in detail, for a well-defined intercalation starting condition. After the hydrogen etching process, the surface of the 4H-SiC substrate is atomically flat [10]. Starting from this, the temperature of the SiC substrate is increased from room temperature (RT) to 1300 °C. This results in various epitaxial grown graphene layers, which are introduced in the following.

3.2.1 Hydrogen passivation of the 4H-SiC substrate

The bare 4H-SiC(0001) surface exhibits Si atoms with unsaturated dangling bonds. This leads to a flat band around the Fermi energy in the band dispersion [69]. The total density of states (DOS), computed by the DFT for six layers of the SiC substrate is depicted in Fig. 3.4a. The unpassivated dangling bond states generate a high DOS at the Fermi level. After the substrate treatment, discussed in chapter 2.1, the surface is atomically flat. In this case, the dangling bonds of the 4H-SiC are H-passivated. A second DFT calculation, that takes the saturated dangling bonds into account, yields the DOS illustrated in Fig. 3.4b. After the H-passivation, the DOS reveals a gap of around 3.29 eV [69]. This surface condition is the starting point for every epitaxial growth mentioned in this thesis. The growth of indenene on SiC, however, requires unsaturated Si atoms, due

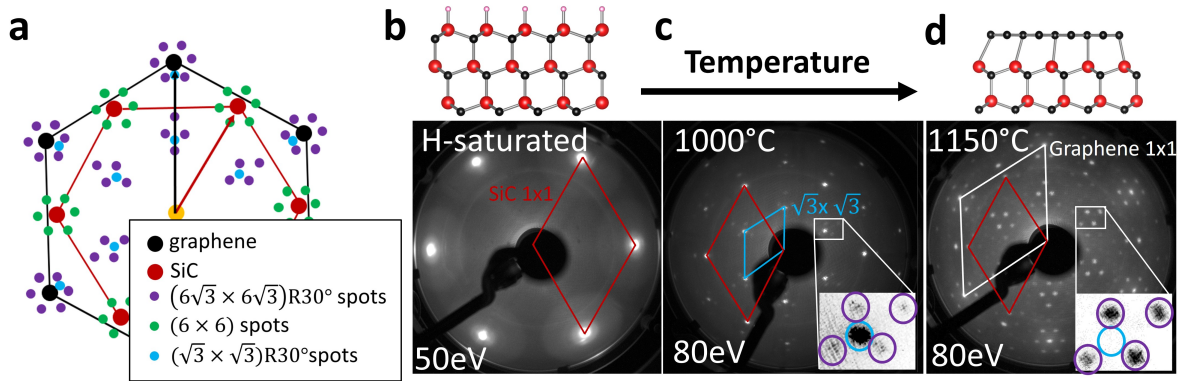


Fig. 3.5: **a** Sketch of the visible spots of the LEED pattern of the $(6\sqrt{3} \times 6\sqrt{3})R30^\circ$ reconstruction. **b** LEED pattern of the hydrogen etched SiC surface at 50 eV, **c** after annealing to 1000 °C and **c** to 1150 °C at 80 eV.

to the necessity of covalent bonds between the indium and the silicon atoms. To solve this, the sample is put to temperatures above 500 °C, immediately before the growth, to desorb the hydrogen atoms. Since the graphene growth requires higher temperatures than 500 °C, the hydrogen desorption happens independently. The structural model for the 4H-SiC with H-passivation is depicted in Fig. 3.4c. The STM image in Fig. 3.4d demonstrates large-scale terraces with sharp steps with a height of approximately 0.5 nm. In the inset, the (1×1) substrate surface can be seen with atomic resolution. The measured lattice constant of 3.08 Å is in good agreement with the before discussed literature value of 3.074 Å [66, 69].

3.2.2 Growth of the buffer layer graphene

The hydrogen etched sample with its (1×1) periodicity is depicted in the LEED image in Fig. 3.5b. With increasing temperature, more and more Si atoms sublime and a wide range of stable metaphases occur. When the temperature is high enough, up to three graphene layers can form above the substrate. A sketch of the LEED pattern corresponding to the different phases is depicted in Fig. 3.5a. Besides the SiC spots (red), the additional phases for the $(\sqrt{3} \times \sqrt{3})R30^\circ$ (blue), the $(6\sqrt{3} \times 6\sqrt{3})R30^\circ$ (purple), the (6×6) (green) and the (1×1) spots, which originate from the graphene (black), can be seen. The smaller graphene lattice constant leads to a larger Brillouin zone, that is rotated by 30° with respect to the SiC substrate.

The first stable phase of interest is the buffer layer graphene. There are several methods to grow this layer on the SiC substrate. One of them is to grow step by step all the reconstructions. This means to start with a (3×3) phase at an annealing temperature of 800 °C in a Si flux. Followed by annealing the sample at 650 °C in UHV to form

a $(\sqrt{3} \times \sqrt{3})R30^\circ$ reconstruction and finally, the buffer layer grows at temperatures of around 1100°C .

Another option is to begin with the $(\sqrt{3} \times \sqrt{3})R30^\circ$ reconstruction in a Si flux with a substrate temperature of 950°C . Afterwards the sample is further heated without Si flow until the $(6\sqrt{3} \times 6\sqrt{3})R30^\circ$ reconstruction appears [43].

In this work, the simplest way to grow the buffer layer was used, by directly annealing the sample at 1150°C for 15 min [70]. The LEED images in Fig. 3.5c and d show the buffer layer growth for different temperatures. A temperature of around 1000°C is still too low to grow a homogeneous buffer layer graphene on the substrate. Here the $(\sqrt{3} \times \sqrt{3})R30^\circ$ reconstruction is dominating. Nevertheless, a partially $(6\sqrt{3} \times 6\sqrt{3})R30^\circ$ reconstruction can be seen in the inset in Fig. 3.5c. Comparing the LEED spots, it is obvious that a substrate temperature of 1150°C is necessary to get rid of the $(\sqrt{3} \times \sqrt{3})R30^\circ$ spots (blue circle) and to form a large-scale $(6\sqrt{3} \times 6\sqrt{3})R30^\circ$ reconstruction. As depicted in Fig. 3.5d, the buffer layer graphene contains also the (1×1) graphene spots (black) despite its missing graphene-like properties, which is demonstrated in Fig. 3.3b [59].

There has been a long debate in the literature about the structure of this buffer layer. One model features a Moire pattern from the ZLG and the substrate [71], but it was so far not confirmed by LEED or ARPES. Another two structure models, namely the $(6\sqrt{3} \times 6\sqrt{3})R30^\circ$ and the (6×6) reconstruction, have been discussed [59, 72]. The LEED spots in Fig. 3.5d originate from the ZLG also showing a $(6\sqrt{3} \times 6\sqrt{3})R30^\circ$ and a (6×6) periodicity, where not all spots of these reconstructions are visible. But a true $(6\sqrt{3} \times 6\sqrt{3})R30^\circ$ reconstruction can already be confirmed by the inset in Fig. 3.5d of the LEED image. The position of the $(\frac{1}{3}, \frac{1}{3})$ spot (blue circle) originates from the $(\sqrt{3} \times \sqrt{3})R30^\circ$ reconstruction. It is however also part of the (6×6) grid and disappears for higher temperatures. The surrounding spots, which are marked in purple, have a distance of $\frac{1}{6}$ of the SiC reciprocal lattice vector to the $(\frac{1}{3}, \frac{1}{3})$ spot. Due to the shift of the spots marked in purple compared to the $(\frac{1}{3}, \frac{1}{3})$ spots, they are clearly part of the $(6\sqrt{3} \times 6\sqrt{3})R30^\circ$ reconstruction [70]. Later this periodicity will be confirmed by STM measurements.

To get a better understanding of the properties of the buffer layer graphene, corresponding XPS core level spectra of the C 1s and the Si 2p before and after the growth are investigated. Additionally, the ARPES band structure of the graphene K point is discussed. The presented core level spectra in Fig. 3.6 are subtracted by a Shirley background following Eq. (2.23) and fitted by Voigt curves. Note, that the minimum number of peaks was fitted, i.e. each peak is associated with an expected species. After the hydrogen etching process, the C 1s core level only shows a bulk peak at 283.4 eV , which is displayed in Fig. 3.6a₁. After the ZLG growth, three additional peaks have to be taken into account besides the new SiC bulk peak at 283.9 eV . The black peak at 284.3 eV in Fig. 3.6a₂ corresponds

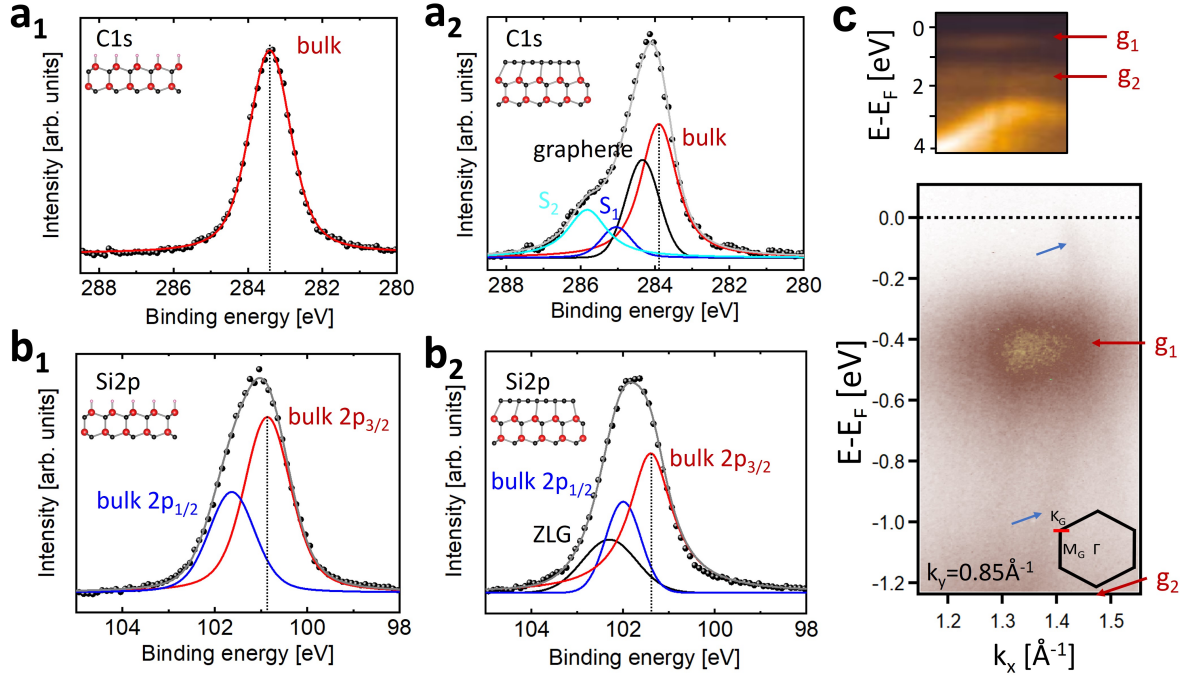


Fig. 3.6: **a,b** C 1s and Si 2p core level spectra of the H-passivated SiC substrate (**a₁**,**b₁**) and after ZLG growth (**a₂**,**b₂**), including Voigt curve fitting. **c** ARPES spectrum ($h\nu=21.2$ eV at RT) at the K point of the $(6\sqrt{3} \times 6\sqrt{3})R30^\circ$ reconstruction (bottom), compared to the literature (top). Taken from Ref. [59]. The measurement direction is depicted in the red line in the BZ.

to graphene. The peaks at 285.8 eV (light blue) and 285.0 eV (dark blue) indicate two different types of carbon that belong to the $(6\sqrt{3} \times 6\sqrt{3})R30^\circ$ reconstruction [43]. One species of C atoms (dark blue) are covalently bound to the substrate and the other one (light blue) is freestanding. Due to the 2:1 ratio of the peaks $S_2:S_1$, it can be obtained, that $\frac{1}{3}$ of the carbon atoms are still covalently bound to the substrate [43]. However, since the graphene peak also appears, the ZLG growth is not homogeneous, but partially monolayer graphene is grown on top of the buffer layer. The peak positions are in close agreement with the values from literature [73].

Not only the carbon C 1s signal shows a difference after the graphene growth, but also the Si 2p peak. For the H-passivated substrate, the Si 2p core level can be fitted with two Voigt functions with their peak maxima at 100.9 eV (blue: 2p_{1/2}) and 101.6 eV (red: 2p_{3/2}). After the graphitization, the main Si bulk peaks shift, like the C 1s peak, around 0.5 eV to higher binding energies, due to the hydrogen desorption and the graphene growth. The covalent bond between the topmost Si atoms and the C atoms from the ZLG results in an additional peak (black) with a maximum at 102.3 eV. The spectrum is in good agreement with the literature [43].

The different electronic properties of the quasi-freestanding graphene and the ZLG, due to the covalent bond, can be seen in the ARPES measurement at the graphene K point in Fig.

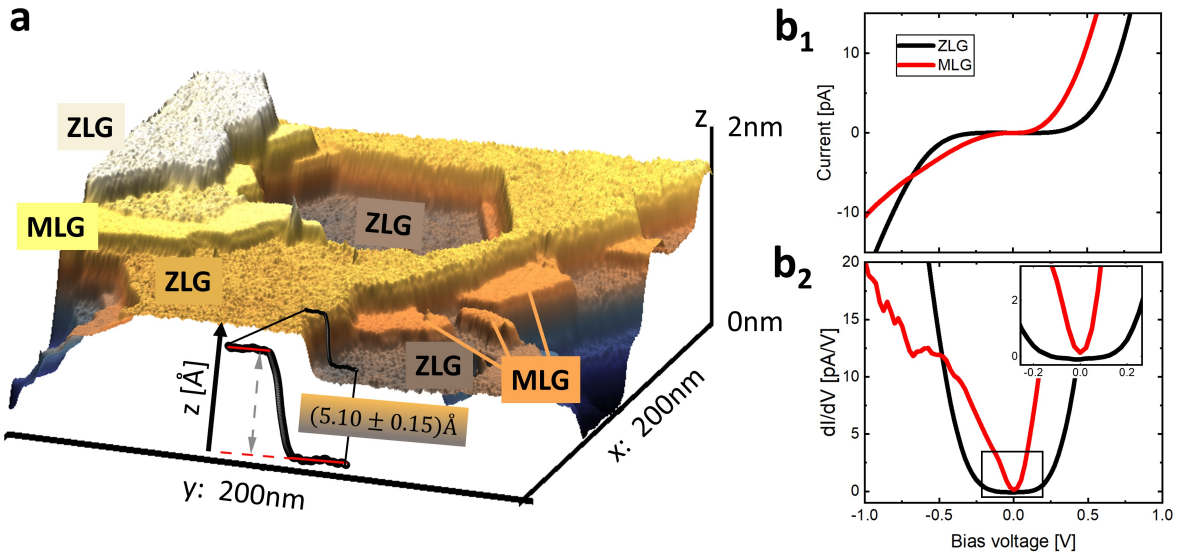


Fig. 3.7: **a** Three-dimensional STM image ($I=10 \text{ pA}$, $U=3.0 \text{ V}$, $T=4 \text{ K}$) of the ZLG. Three substrate caused steps with a height of $(5.10 \pm 0.15) \text{ \AA}$ and a MLG growth at the step edge is observed. **b** STS measurements for both coverages, with the I-V curve (**b₁**) and their derivation (**b₂**) reveal the semi-metallic graphene behavior and a large-gap of the DOS around E_F for the ZLG.

3.6c. As discussed in chapter 3.1.2, the band structure of the ZLG exhibits graphene-like σ -bands, but due to the covalent bond between the substrate and the $(6\sqrt{3} \times 6\sqrt{3})R30^\circ$ reconstruction, no π -bands are observed. The band structure of the ZLG from the literature (top) is in good agreement with the ARPES spectrum around the K point in Fig. 3.6 (bottom). Two localized states at the K point arise with their binding energies around 0.3 eV to 0.5 eV and above 1.3 eV . Partially graphene-covered ZLG regions on the surface make the linear π -bands also slightly visible. This is indicated with blue arrows in Fig. 3.6c.

A three-dimensional large-scale STM image of the ZLG and monolayer graphene (MLG) growth is displayed in Fig. 3.7a. There are three terrace steps on the surface in white, yellow and brown from the left to the right. The terraces are approximately 200 nm wide and emerge from the SiC substrate, as mentioned in chapter 3.2.1. Their step height of $(5.10 \pm 0.15) \text{ \AA}$ matches with the before discussed value for bare $4\text{H-SiC}(0001)$ [66]. The error is determined by using the largest error estimation. Besides the ZLG terraces, also monolayer graphene flakes are formed. However, the area of the MLG on the surface was determined to be 7.8% , which suggests a nearly homogeneous ZLG growth and agrees with the ARPES data in Fig. 3.6c. It can be clearly seen that the graphene forms first at the step edge of the SiC substrate. To identify ZLG and MLG, STS measurements on both coverages were performed. For a representative surface area of 20 nm^2 , the tunneling voltage was ramped in a range from -1.0 eV to 1.0 eV and the corresponding current was

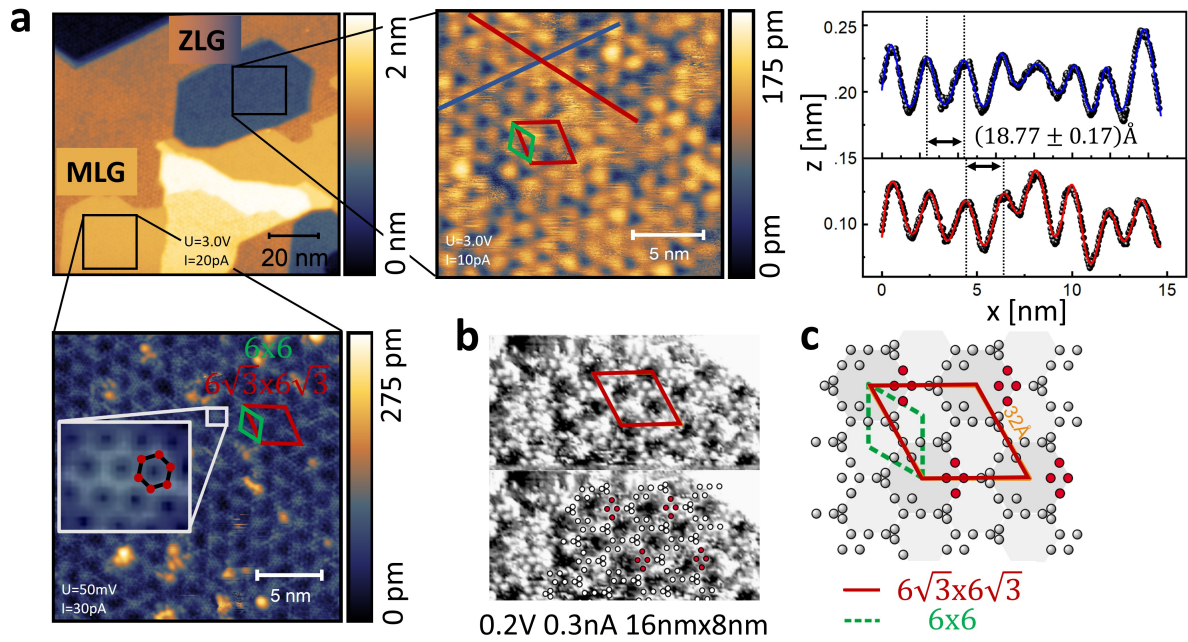


Fig. 3.8: **a** Large-scale STM image ($T=4\text{K}$) of the MLG and ZLG with the inset for both coverages. For the ZLG, the (6×6) periodicity, determined by the line profile on the right, is visible. In the MLG case the quasi-freestanding graphene layer is in addition atomically resolved. **b** STM image of the ZLG resolved two rings with different sizes, thus refuting the (6×6) periodicity. Taken from Ref. [70]. **c** The structure model from **b** leading to the true $(6\sqrt{3} \times 6\sqrt{3})R30^\circ$ periodicity. Taken from Ref. [70]

detected. The average I-V as well as the differential tunneling conductivity dI/dV curves, a measure of the LDOS, are plotted in Fig. 3.7b. The ZLG (black curve) exhibits a significantly larger plateau at the Fermi level of $\pm 0.2 \text{ V}$ compared to MLG. The dI/dV curves reveal no states in a range of about 300 meV around the Fermi energy for ZLG. In the case of MLG, there is a minimum in the dI/dV curve, but the minimum value is larger than zero, indicating metallic states as to be expected in graphene. The observed curves reproduce the known behavior, which was reported earlier [74, 75].

A second large-scale STM image of the buffer layer and the MLG is depicted in Fig. 3.8a. Both types of coverages are displayed in the insets with atomic resolution. For the ZLG, a triangular reconstruction is observed. Therefore, various line profiles, as seen for example in blue and red, were taken and result in a distance of $(18.77 \pm 0.17) \text{ nm}$. The error is the standard error of the mean. This distance corresponds to a (6×6) reconstruction, with respect to the SiC lattice constant. The (6×6) unit cell is shown in green. For the monolayer graphene, the same substructure appears, but in addition to that the honeycomb graphene lattice, which is grown on top of the ZLG, could be resolved (white inset). The positions of the carbon atoms in the honeycomb are marked in red. Previously it was discussed that a $(6\sqrt{3} \times 6\sqrt{3})R30^\circ$ reconstruction was determined, but this STM

image shows supposedly a (6×6) periodicity. Such a periodicity has been reported in many other STM studies [76, 77, 78], but this is in contradiction to the above-mentioned LEED measurements and also to theoretical calculations [79, 50]. C. Riedl *et al.* were the first to resolve the $(6\sqrt{3} \times 6\sqrt{3})R30^\circ$ reconstruction in an STM measurement [70]. The results are shown in Fig. 3.8b, where the upper and lower panel display the same area on the sample. In the lower panel, the individually resolved atoms are sketched. This atomic order leads to two different sized rings, which can be better seen in the structural model in Fig. 3.8c (dark and light gray). Due to the two different hexagon sizes, the unit cell exhibits not a (6×6) (green), but the larger $(6\sqrt{3} \times 6\sqrt{3})R30^\circ$ periodicity (red). The true $(6\sqrt{3} \times 6\sqrt{3})R30^\circ$ periodicity can be clearly seen from the atomic bumps, displayed as red atoms. Only for the large $(6\sqrt{3} \times 6\sqrt{3})R30^\circ$ unit cell it is possible to periodically repeat their occurrence. The unit vector lengths determined from Fig. 3.8a of the $(6\sqrt{3} \times 6\sqrt{3})R30^\circ$ reconstruction is (3.24 ± 0.16) nm, as expected from Ref. [70]. The error is the standard error of the mean.

This section has demonstrated, that the buffer layer graphene can be grown with high quality on SiC by simply heating the substrate. Furthermore, it has been shown that the ZLG is a true $(6\sqrt{3} \times 6\sqrt{3})R30^\circ$ reconstruction, where $\frac{1}{3}$ of the carbon atoms are still covalently bound to the substrate. Therefore, the electronic structure is different compared to a freestanding graphene layer.

3.2.3 Quasi-freestanding monolayer graphene

By further increasing the substrate temperature, quasi-freestanding graphene layers are formed above the ZLG. Here, the topmost silicon atoms sublime through the $(6\sqrt{3} \times 6\sqrt{3})R30^\circ$ reconstruction. Thus, the covalent bonds are broken and the ZLG decouples from the substrate and transforms into monolayer graphene. The C atoms below the graphene then rearrange in a new $(6\sqrt{3} \times 6\sqrt{3})R30^\circ$ reconstruction. This kind of graphene growth was already observed before, where only small monolayer graphene flakes close to the SiC step edge occurred. For temperatures above 1150°C the whole sample is covered by MLG. The STM image in Fig. 3.8a demonstrates the honeycomb structure of the graphene lattice, with the $(6\sqrt{3} \times 6\sqrt{3})R30^\circ$ buffer layer reconstruction below. The monolayer graphene lattice constant is (2.5 ± 0.1) Å. The error was estimated by the STM stage calibration. This value is in good agreement with the lattice constant of exfoliated graphene (2.46 Å) [41] and the value found in the literature for epitaxial graphene growth on SiC with (2.5 ± 0.1) Å [74]. Due to the quasi-freestanding behavior of the MLG, the linear π -bands are formed. Fig. 3.9b displays the ARPES measurement around the Dirac point of graphene in the mapping direction parallel to k_x , which is depicted in Fig. 3.9a. The linear dispersion of the valence and conduction band can be identified, but they are

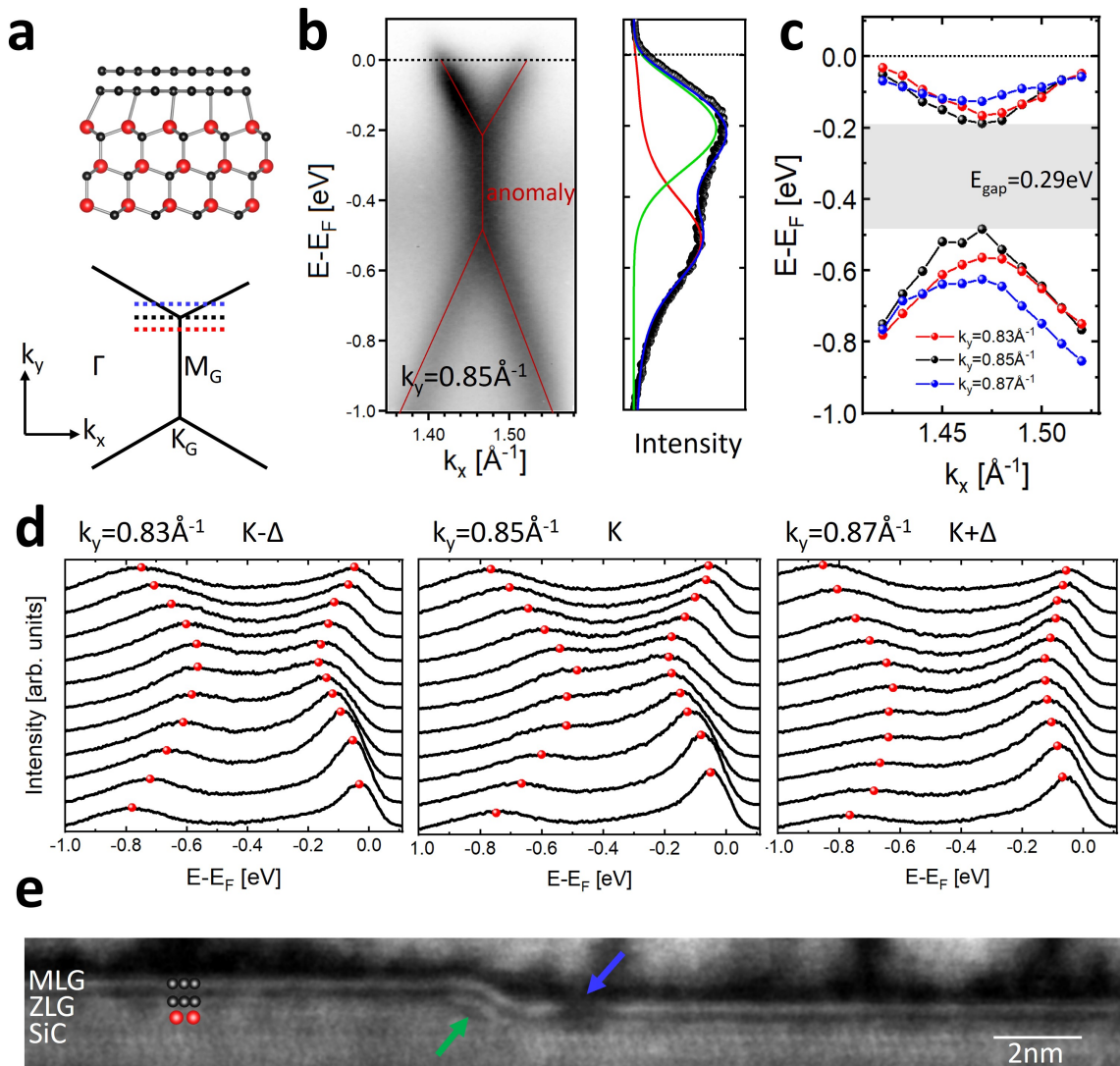


Fig. 3.9: **a** Ball-and-stick model for the MLG. **b** ARPES spectrum ($h\nu=21.2$ eV, at RT) of the quasi-freestanding graphene layer at the K point with an exemplary EDC along the black path shown in **a**. **c** Peak position results by Voigt fitting the EDCs in **d** for the three different cuts. **e** STEM image of the MLG with a SiC substrate step (green arrow) and a vacancy in the graphene lattice (blue arrow).

not connected to each other in a straight line, as expected for freestanding graphene. To prove that the ARPES data was measured exactly at the K point and the discrepancy between the well-known freestanding graphene band structure is not made by a false cut through the Brillouin zone, two additional ARPES cuts with a spacing of 0.02 \AA^{-1} were analyzed. For each of the three cuts, the energy distribution curves (EDCs) are fitted by two Voigt peaks multiplied by the Fermi-Dirac distribution function, as shown in Fig. 3.9b. The green curve indicates the minimum of the conduction band and the red one reveals the valence band maximum. All the corresponding EDCs for each cut including

their peak positions obtained by the curve fitting (red markers) are depicted in Fig. 3.9d. The fit results are then displayed as a function of the wave vector k_x in Fig. 3.9c, indicating a non-linear behavior at the Dirac point. From the measurements, one can be ensured, that the ARPES measurement in Fig. 3.9b is exactly at the K point of graphene, since the anomalies at the Dirac point become larger for $k_y = \pm 0.02 \text{ \AA}^{-1}$.

The MLG growth on top of the ZLG can also be confirmed by a STEM image shown in Fig. 3.9e. Besides the MLG and the substrate step, indicated with a green arrow, a vacancy in the graphene layer (blue arrow) is depicted. Such impurities are yet significant for the intercalation process, as discussed in chapter 4.

The anomalies at the graphene Dirac points on SiC have been in debate in the literature for over ten years. The three attempts of explanation, which report an energy gap, a kink in the band at the Dirac point or none of them and the anomalies are attributed to the lifetime and momentum broadening in the experiments, which will be discussed below. In Fig. 3.10a, the ARPES spectrum near the K point is assumed to have an energy gap of around 0.26 eV, due to an AB sublattices symmetry breaking [80]. The EDCs peak positions give rise to the dispersion (black) in the ARPES spectra. This energy gap is in close agreement with the potential gap seen in Fig. 3.9c with about 0.29 eV. As mentioned in chapter 3.1.1, graphene consists of two equivalent sublattices, namely sublattice A and B. Due to the interaction between the ZLG and the monolayer on top, the equivalence of the two sublattices is destroyed and an energy gap opens. Such inequivalent sublattices are well known from Bernal stacked bilayer graphene. As discussed previously, the ZLG is structurally identical to the monolayer and therefore it can break the AB sublattices symmetry, similar to two ABAB stacked graphene layers. The sublattice symmetry breaking causes also the breaking of the six-fold rotational symmetry. Indeed the ARPES constant-energy surface maps in Fig. 3.10a₂ reveal a six-fold symmetry at the Fermi energy E_F around the graphene K point, but for energies that are located inside the "band gap", the sublattices are inequivalent, leading to a three-fold symmetry [80]. These two measurements explain the absence of three-fold symmetry in Fig. 3.8a. The main graphene signal in STM is at the Fermi level, where the six-fold symmetry remains. S.Y. Zhou *et al.* also claim, that the non-zero intensity in the band gap is due to the overlap of the intensities of the band maxima.

Compared to the interpretation of a band gap, Bostwick *et al.* assert, that there is a kink at the Dirac energy E_D due to a strong electron-plasmon coupling [81]. In Fig. 3.10b₁ the ARPES spectra and the calculated band dispersion of the graphene K point are shown. Due to interference effects, the second band is suppressed [81, 83]. The black solid line in the ARPES spectra displays the fitted Lorentzian peak positions of the momentum distribution curves (MDCs). The two kinks are marked with a yellow and a blue arrow. The linewidth of the Lorentzian peaks fitted to the MDCs is proportional to the imaginary

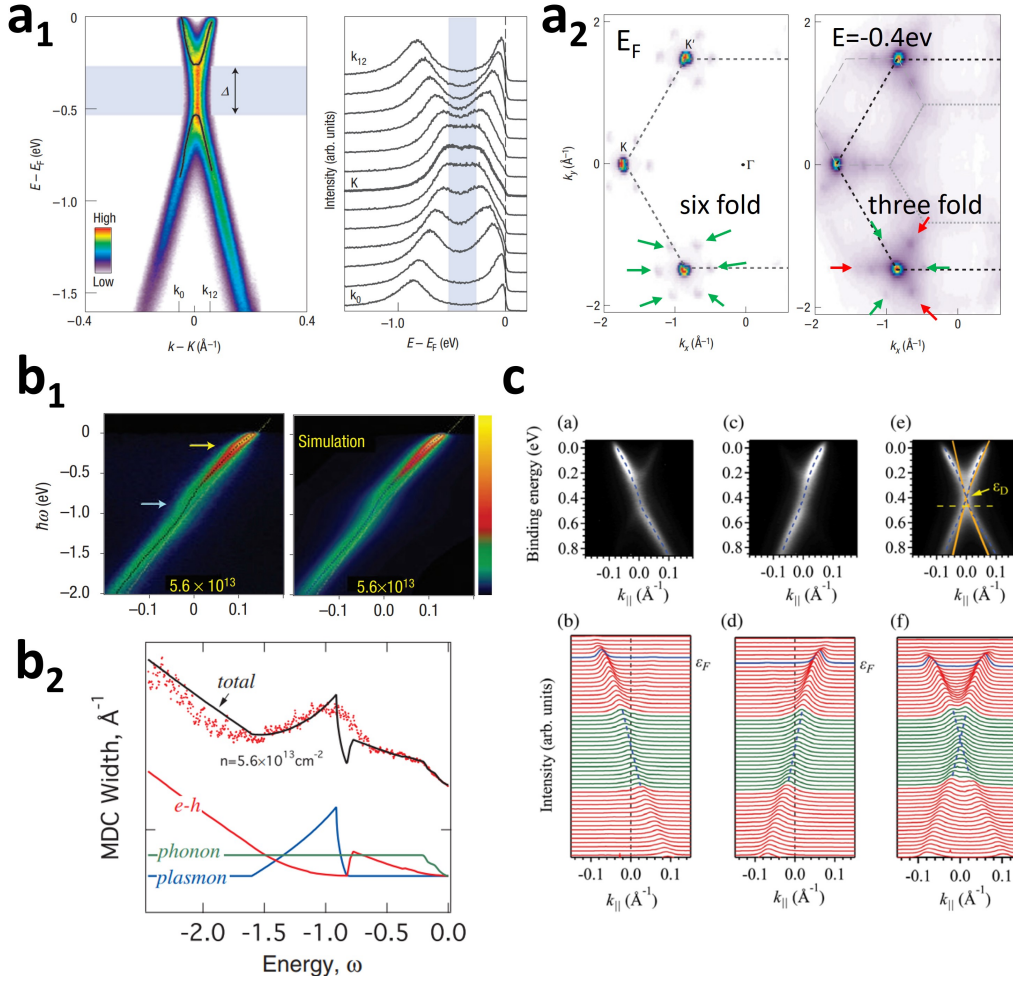


Fig. 3.10: **a** ARPES spectra at the graphene Dirac point with the corresponding EDCs in **a₁** and **a₂** the constant energy maps at the Fermi level and inside the gap. Taken from Ref. [80]. **b** Band structure of the graphene K point measured with ARPES (**b₁** left) and simulated using the spectral function (**b₁** right). The MDCs width of the ARPES spectra as a function of the energy in **b₂** is fitted by the total scattering rate. The different contributions due to electron-hole pairs (red), electron-plasmon (blue) and electron-phonon scattering (green) are displayed at the bottom. Taken from [81]. **c** ARPES data of the graphene K point measured with s -polarized (left), p -polarized (middle) and circularly polarized light (right) with their corresponding MDCs. Taken from Ref. [82].

part of self-energy $\Sigma(\vec{k}, \omega)$. The latter contains the scattering rate and the band renormalization and was introduced in chapter 2.2.4 [81]. The imaginary part can be converted into the real part using a Hilbert transformation. Subsequently, with Eq. (2.20) the spectral function measured with ARPES can be calculated and compared to the experimental results. Due to the fact that the theory, based on the MDCs widths, and the experimental spectrum matches perfectly, it could be shown that the anomalies must be attributed to many-body interactions [84]. In Fig. 3.10b₂, the Lorentzian width is plotted as a function

of the energy (dots) and fitted by the total scattering rate. The individual contributions are depicted at the bottom. The upturn in the MDCs at the Dirac energy E_D can then be associated with the electron-plasmon coupling. The quasiparticle dynamics in graphene renormalize the bands around the K point.

However, both approaches have vulnerabilities. The interpretation of electron-plasmon band renormalization is based on the upturn in the MDCs. This conclusion must be viewed critically, as such anomalous upturn is often seen in ARPES measurements at band extrema [80]. Therefore an EDC analysis would lead to a more reliable result, as in the first presented approach. However, there are also doubts about the existence of a substrate-induced band gap, because there was no band gap observed in transport measurements hitherto [70, 82].

Recently A. Pramanik *et al.* claimed, that both approaches are incorrect and the anomalies at the K point arise due to experiment-caused momentum broadening [82]. Therefore, the ARPES spectra at the Dirac point were measured with s and p polarized light, which suppresses one band in each case, respectively. The dispersion for each of the two polarizations separately, both plotted together and their MDCs can be seen in Fig. 3.10c. With the dashed blue lines, obtained from the MDCs, the ARPES spectrum is fitted. Together with the DFT calculation, which is shown in orange, the theory and experiment are, at least at the K point, in good agreement and no band gap is visible. In their work, they also studied the change of the band dispersion, when reducing the carrier concentration n by boron doping. With decreasing n , the Dirac cone gets narrower. As a consequence, the band at the K point cannot be resolved, because the distance of the two bands is similar to the momentum resolution [82]. This means, that the effect of the overlap from different bands causes the anomalies at the Dirac point, which increase with decreasing carrier concentration n . However, this contradicts the many-body interaction approach. The plasmon frequency is proportional to $\propto \sqrt{n}$, which denotes that the plasmon frequency and therefore also the anomalies decrease for decreasing carrier concentration n [81, 82]. Thus, to date, the anomalies around the Dirac point are not unambiguously clarified.

3.2.4 Bilayer graphene

At temperatures above 1250 °C, even more Si sublimates and another graphene buffer layer is formed. The previous ZLG will then decouple from the substrate and a new quasi-freestanding graphene layer arises. This bilayer graphene on top of the ZLG is shown in Fig. 3.11b. The two graphene layers are exemplarily displayed in green and black. When looking from the top, the Bernal stacking of the layers is observed. The two monolayers are stacked in such a way that the carbon atoms from one sublattice lie directly above the C atoms from the lower layer. Therefore, the two sublattices (red

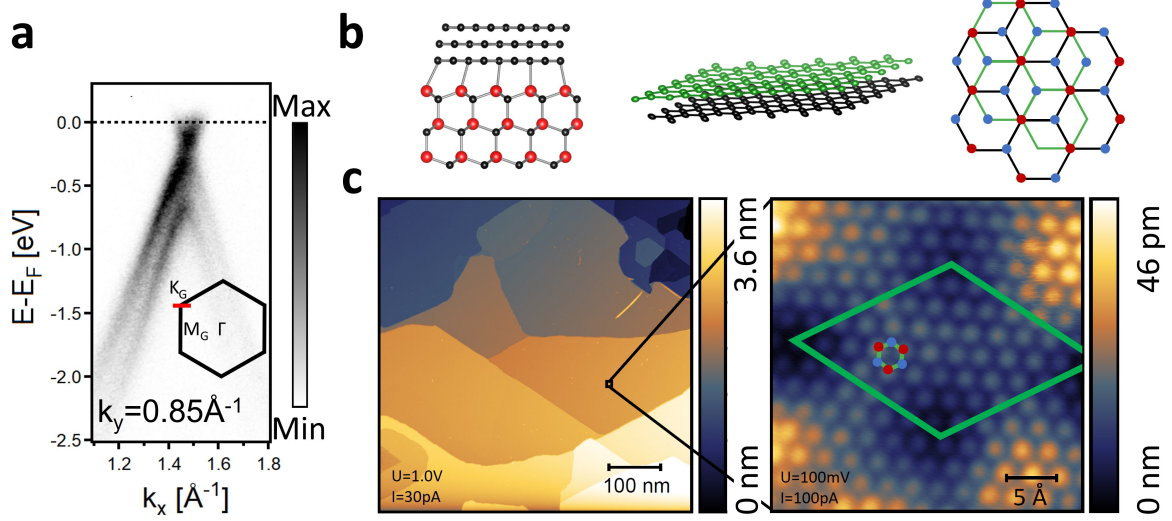


Fig. 3.11: **a** ARPES spectra ($h\nu=40.8\text{ eV}$ at RT) of the graphene Dirac point for a bilayer graphene sample with Bernal stacked structure shown in **b**. **c** STM image ($T=4\text{ K}$) of the large-scale bilayer graphene and an inset, showing the three-fold symmetry and the quasi (6×6) unit cell.

and blue) can be distinguished. Consequently, the six-fold symmetry for the freestanding graphene is reduced to a three-fold symmetry. The bilayer graphene in this work was not grown just by high substrate temperatures, but with the flash annealing method reported in Ref. [85]. One flash cycle consists of the annealing from $650\text{ }^\circ\text{C}$ to $1300\text{ }^\circ\text{C}$ in 80 s, a constant temperature of $1300\text{ }^\circ\text{C}$ for 30 s and a cooling down to $650\text{ }^\circ\text{C}$ in 30 s [85]. At least 80 cycles are necessary to grow high-quality large-scale bilayer graphene.

In Fig. 3.11a, the corresponding ARPES spectrum measured with HeII radiation is depicted. Due to the interlayer coupling, the graphene π -bands will split and the number of graphene layers can be determined by simply counting the bands. The STM images in Fig. 3.11c show the high-quality growth on the micrometer scale. In the inset (right) the quasi (6×6) unit cell (green) and the honeycomb lattice with the carbon atoms in red and blue are placed on the data. For bilayer graphene, this honeycomb lattice is not visible due to the three-fold symmetry. At the chosen tunneling parameter the atomic resolution from one sublattice can be displayed.

Chapter 4

Intercalation of indenene into graphene/SiC

In this chapter, the topology in reduced dimensions (SSH model) is motivated to build the bridge to the properties for 2D TIs. Afterwards, the recently discovered triangular QSHI indenene is introduced. Indenene immediately oxidizes at ambient conditions, making it useless for electronic device applications. The goal of this thesis is to cap the indenene with the inert quantum material graphene. As discussed in the previous chapter, ZLG is first grown on the 4H-SiC(0001) substrate. Subsequently, indium atoms are intercalated into the graphene/SiC interface, reproducibly forming bilayer indium underneath the graphene. After a post-annealing step without further In evaporation, the intercalated high-coverage phase of indium transforms into a single layer that captures the band and real space structure of the QSHI indenene. Finally, the oxidation and heat stabilities, as well as the topological properties of this new heterostructure are investigated.

4.1 Topological insulators

TIs are in the bulk insulating, but they host metallic edge states [5, 86]. These spin-polarized edge states contribute to dissipationless conduction and are protected by TRS. The discovery of different topological phases of matter started in 1988 when Haldane theoretically described the QHE [87, 88]. Here, the degeneracy of the graphene Dirac point is lifted by breaking the TRS using a magnetic field [86, 87]. In 2005 Kane and Mele extended the model of the QHE to the QSHE in graphene, where they take the spin of the electrons into account. Here the edge states emerge, due to the SOC and an unbroken TRS at the same time [5]. By the fact, that 2D TIs exhibit the QSHE, the first TI was born in theory [86]. Only two years later König *et al.* could realize the first TI consisting of $Hg_xCd_{1-x}Te$ quantum wells [7].

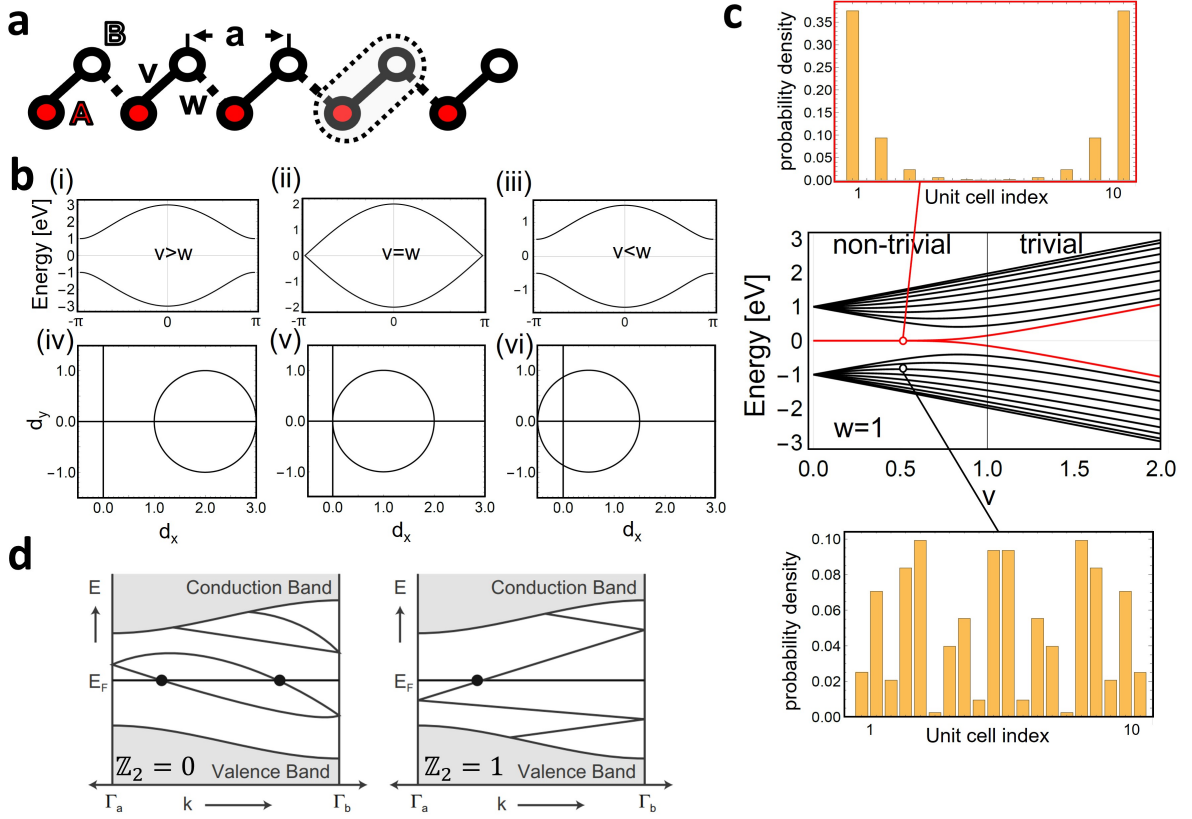


Fig. 4.1: **a** SSH chain with five unit cells indicated by dotted lines. **b** Energy dispersion after Eq. (4.3) for (i) $v = 2, w = 1$; (ii) $v = 1, w = 1$; (iii) $v = 0.5, w = 1$ and in (iv)-(vi) the corresponding path of the vector \vec{d} in $d_x d_y$ plane. **c** Energy spectrum for 10 unit cells as a function of v , while $w = 1$. The wave function of the bulk (edge) at $v = 0.5, w = 1$ is depicted with a black (red) frame. Calculations were performed using *Mathematica*. **d** Band structure for a trivial (left) and a non-trivial insulator (right), showing an even and odd surface state crossing at the Fermi level, respectively. Taken from Ref. [89].

4.1.1 Su-Schrieffer-Heeger model

A simple, yet important model to learn about topology is the 1D SSH model [90]. This model describes the hopping of neighboring atoms on a 1D chain as depicted in Fig. 4.1a. The linear chain exists of two sublattices, illustrated as filled (A) and empty (B) circles. The unit cell is shown with dotted lines and contains one atom from each sublattice. Here, v is the hopping amplitude within one unit cell and w denotes the intercell hopping. At first, the focus is placed on the bulk part of the infinite chain with periodic Born-von Karman boundary conditions. The lattice constant a is the distance between two atoms from the same sublattice. The Hamiltonian of this system, when neglecting the electron

interaction, is given by

$$\hat{H} = v \sum_{m=1}^N (|m, B\rangle \langle m, A| + h.c.) + w \sum_{m=1}^{N-1} (|m+1, A\rangle \langle m, B| + h.c.), \quad (4.1)$$

where *h.c.* stands for the Hermitian conjugated and m is the index of the N unit cells [91]. Thus, the first term describes the hopping from A to B in the same unit cell, whereas the second term allows the hopping between two unit cells. With a tight binding approach for two atoms per unit cell, the momentum space Hamiltonian

$$H = \begin{pmatrix} 0 & v + we^{-ika} \\ v + we^{-ika} & 0 \end{pmatrix}, = \vec{d} \cdot \vec{\sigma} \quad \text{with} \quad \vec{d} = \begin{pmatrix} v + w \cos(k) \\ w \sin(k) \end{pmatrix} \quad (4.2)$$

is a (2×2) matrix with the wavenumber k [91]. Since it was assumed that the on-site energy of each orbital is the same, the diagonal entries are zero. Similar to graphene, this Hamiltonian can be written as a scalar product of the Pauli matrices $\vec{\sigma}$ with a coefficient \vec{d} [91]. By diagonalizing the Hamiltonian, the eigenvalues can be calculated to:

$$E_{\pm} = \pm \sqrt{v^2 + w^2 + 2vw \cos(ka)} \quad [91]. \quad (4.3)$$

This dispersion relation is displayed for different v and w values in Fig. 4.1 (i)-(iii). If $v = w$ the band gap is closed and the system acts like a gapless semiconductor similar to graphene. But for the case $v \neq w$ an energy gap with

$$E_{\text{Gap}} = 2|v - w| \quad (4.4)$$

between the upper and lower band opens. With regards to solid-state physics such a band gap corresponds to an insulator. But what does that have to do with TIs? Hence, the path of the vector \vec{d} , when k goes through the Brillouin zone, on the $d_x d_y$ plane is shown in Fig. 4.1b (iv)-(vi) [91]. This vector encodes another internal structure of the eigenstates. The circle with radius w and center $(v, 0)$ can be used to distinguish the topological class of the system. Therefore, the winding number around the origin is a topological invariant. If the circle avoids the origin $v > w$ the system belongs to a trivial insulator with winding number 0, but when $v < w$ the system is in a topological non-trivial phase and has a winding number of 1 [91]. This winding number is related to the \mathbb{Z}_2 invariant of TIs and is discussed in the forthcoming chapter. As depicted in Fig. 4.1b the topological invariant can only be changed when closing and reopening a band gap. Due to the non-trivial bulk band structure edge states exist. To prove that, an open chain containing ten unit cells is calculated. In Fig. 4.1c the energy spectrum is shown, when tuning the intracell hopping v , while w is set to 1. The topological trivial phase should be at $v > 1$. Indeed, a band

gap between the upper and lower band is found. In the non-trivial phase for $v < 1$, the band gap of the black bands remains, but inside this gap states appear, which are plotted in red. For a fixed intracell hopping of $v = 0.5$ the probability density for each unit cell of the black and the red bands are shown in the inset of 4.1c. It can be clearly seen, that the red bands correspond to the edge states, whereas the black band originates from the bulk bands. The probability density from the red bands is strongly located only at the edge of the chain and decays exponentially into the bulk [91]. As mentioned above, the bulk band structure is linked to the winding number to distinguish the topological non-trivial from the trivial phase. Since the topological non-trivial phase always has edge states, the winding number is also connected to the occurrence of these states. This is also known as bulk-boundary correspondence [91]. The SSH model introduces the physical properties of a 1D TI, which will be extended to the 2D TIs in the next section.

4.1.2 Two-dimensional topological insulators

There are a lot of parallels between the 1D TI in the SSH model and the 2D TIs consisting of one monolayer. The properties of 2D TIs will be explained using the already familiar graphene. Its band structure in Eq. (3.5) does not involve SOC contributions and therefore no energy gap appears [45, 46]. Kane and Mele first calculate the energy dispersion for graphene by taking SOC into account [5]. The SOC opens a band gap at the Dirac points and therefore the dispersion is given by

$$E(q) = \pm \sqrt{|\hbar v_F q|^2 + \Delta_{\text{SOC}}^2}, \quad (4.5)$$

where $2\Delta_{\text{SOC}}$ is the arising energy gap [5]. Like in the SSH model, graphene also hosts helical (spin-momentum locked) edge states, that are protected by TRS. Thus spin up and down states propagate in opposite directions [92]. The distinction between the topological trivial and non-trivial phase can be done analogously to the winding number in the SSH model. In Fig. 4.1d the band structure of a trivial and non-trivial insulator is depicted, showing only one half of the Brillouin zone, due to the mirror image of the second half. The topological phase of a material can be determined by counting the crossing points of the edge states at a certain energy inside the bulk band (gray) gap. If the crossing number is even, the topological invariant is $\mathbb{Z}_2=0$. These states can be pushed out of the gap and the system is in the topological trivial phase [89]. For an odd number of crossing points, the edge states always remain and the QSHI has a \mathbb{Z}_2 invariant equal to 1.

For future devices applications, the energy gap must be larger than the thermal broadening at room temperature ($E_{\text{Gap}} = 3.5 k_B T \sim 90 \text{ meV}$) [92]. In the case of graphene the SOC opens a band gap, which is less than $50 \mu\text{eV}$ [6]. Consequently, this discovery started the search for new 2D materials with larger energy gaps. The fact that the QSH gap depends

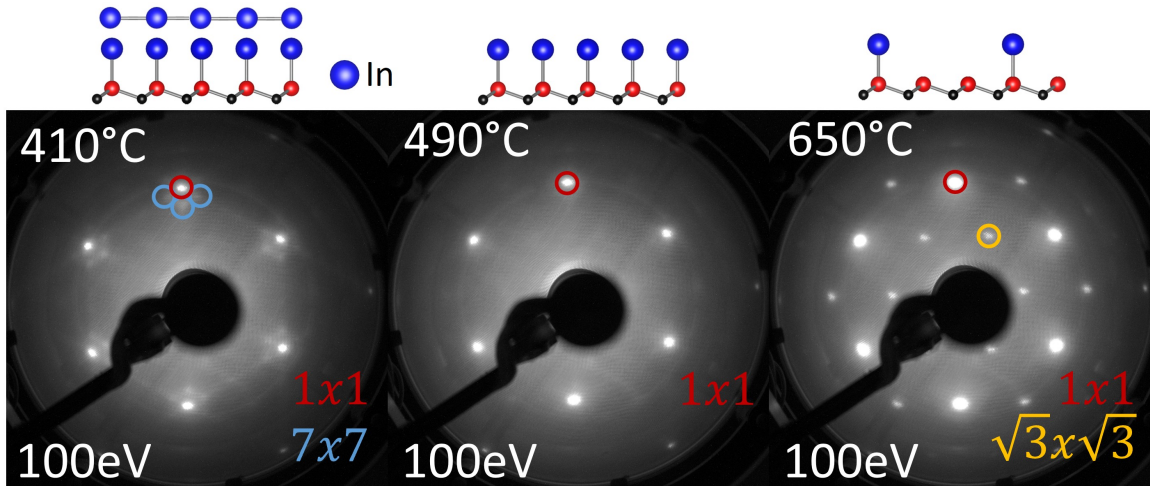


Fig. 4.2: LEED images for different numbers of indium layers grown on 4H-SiC. With successive annealing, the high-coverage phase of indium turns into the QSHI indenene and lastly into a $(\sqrt{3} \times \sqrt{3})R30^\circ$ reconstruction.

mainly on the strength of the SOC and the SOC scales with Z^4 , the search focuses on heavy materials, like Pb, Bi or In. To date, the QSH state has been theoretically predicted and experimentally demonstrated for many 2D materials and most of them are grown in a graphene-like honeycomb lattice [93]-[96]. The 2D TI with the so far largest energy gap of $E_{\text{Gap}} \sim 800$ meV, is bismuthene on SiC(0001) [8].

4.2 Indenene - a novel quantum material

In 2021 Bauernfeind *et al.* realized a new type of 2D TI [9]. They theoretically predicted a QSHI existing of a triangular instead of a honeycomb lattice and realized the system as a monolayer of indium on SiC(0001), called indenene. A triangular arrangement is supposed to be more favored by most elements on hexagonal templates [9].

The hydrogen passivated 4H-SiC substrates are evaporated with indium atoms from a Knudsen cell. Indium on 4H-SiC(0001) grows in a Stranski–Krastanov growth mode. Hereby In islands with up to 7 nm height arise on top of three homogeneous In wetting layers [97]. Via thermal treatment at temperatures between 250 °C and 460 °C the island are evaporated and only a flat film of the wetting layer indium remains [97]. The surface structure of this phase determined by LEED can be seen in Fig. 4.2. Besides the (1×1) structure of the pure SiC substrate, a (7×7) reconstruction is observed, which corresponds to an up to three layers indium coverage [97]. Starting from this, the sample is heated up to temperatures around 490 °C until the (7×7) reconstruction vanishes and the monolayer indenene forms. The monolayer is very sensitive to temperature, meaning that 600 °C are sufficient for an evaporation of the indium atoms. At such high temperatures a $(\sqrt{3} \times$

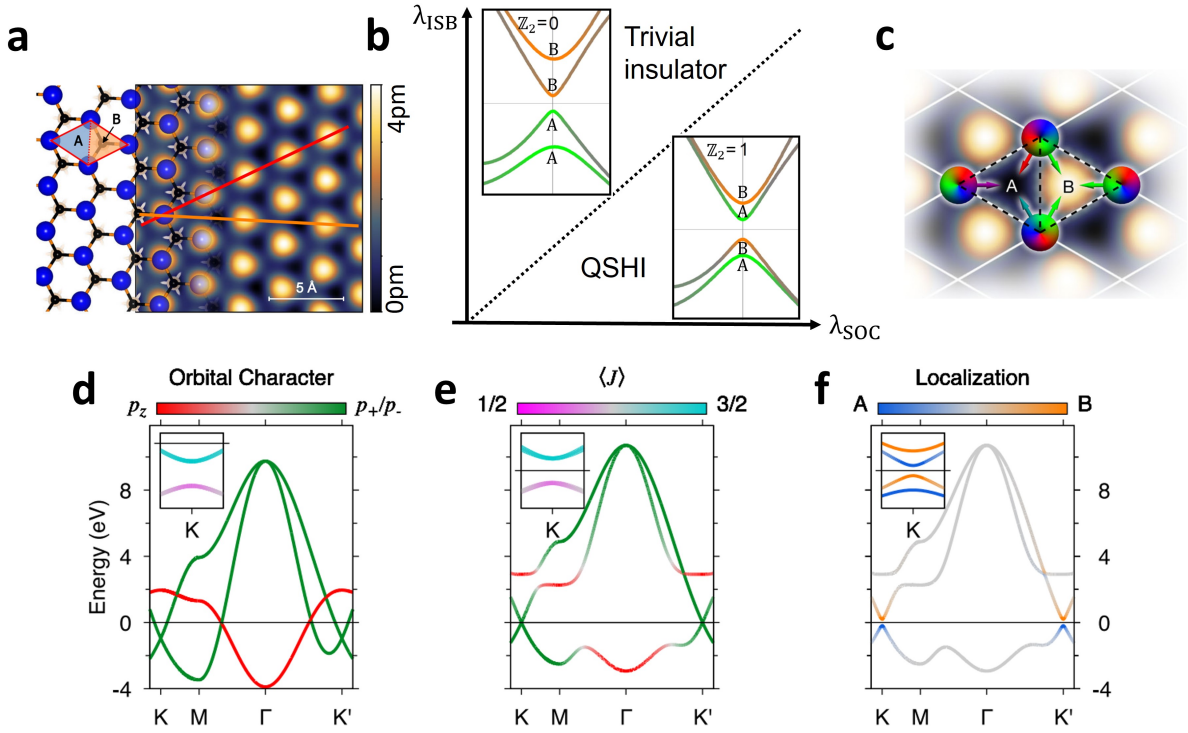


Fig. 4.3: **a** Structural model and STM topography of indenene on SiC(0001). **b** Topological phase diagram of a trivial insulator and a QSHI depending on the strength of SOC and ISB, with its corresponding OAM stacking at the Dirac point. **c** Indenene unit cell with the charge localization in half B due to the constructive interference of the Bloch and orbital phases of p_- states at K . **d-f** Band structure for a triangular QSHI along the $KMT\Gamma K'$ high symmetric path without (with) SOC in the main panel (inset), **d** for a freestanding monolayer, **e** grown on a homogeneous substrate and **f** on a SiC substrate with inequivalent halves A, B of the unit cell. All taken from Ref. [9].

$\sqrt{3})R30^\circ$ reconstruction appears, which could be due to the indium atoms rearranging in a new configuration or a large amount of indium is evaporated and the $(\sqrt{3} \times \sqrt{3})R30^\circ$ reconstruction originates from the SiC substrate.

The structural model including an STM measurement of this system, is depicted in Fig. 4.3a. To describe a model for a triangular 2D TI the two in-plane $p_\pm = \frac{1}{\sqrt{2}}(p_x \pm ip_y)$ and the out-of-plane p_z orbital are used [9, 97]. The tight binding model of a freestanding triangular monolayer is presented in Fig. 4.3d. This system is in a metallic phase, where the p_\pm orbitals provide a similar band crossing at the K and K' points like in graphene, but where the crossing point is below the Fermi level. In the insets of Fig. 4.3d-f the dispersions around the K point valley states are depicted, when taking SOC into account. Although an energy gap opens for the freestanding monolayer, the system remains metallic due to band crossing at the Fermi level in the ΓK and ΓM direction. Expanding this model to a homogeneous substrate, the mirror symmetry along the surface normal breaks and the p_z and p_\pm orbitals hybridize and a global gap opens [9]. Taking SOC into account,

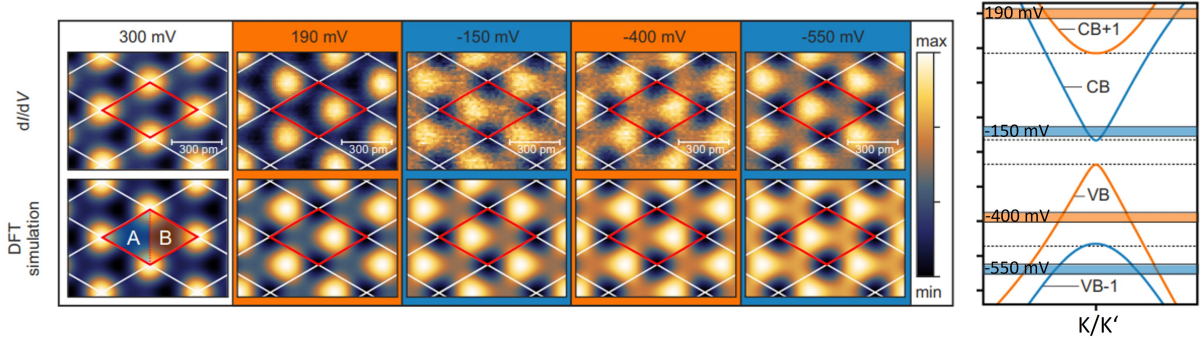


Fig. 4.4: Comparison of the DFT simulation and the STS dI/dV maps representing the charge localization for the different valleys at the Dirac point. The alternating charge localization switching denotes the non-trivial phase of indenene. Taken from Ref. [9].

a topological non-trivial state is realized. However, indenene is grown on a SiC(0001) substrate. Here, the carbon atoms for the topmost SiC substrate layer render the halves A (blue) and B (orange) of the indenene unit cell inequivalently (see Fig. 4.3a) [9]. Thus, the $C_{6\nu}$ symmetry is reduced to a $C_{3\nu}$ symmetry. The occurring inversion-symmetry break (ISB) counteracts the SOC and favors the trivial phase. The band structure without SOC is depicted in Fig. 4.3f, where the ISB ensures that the triangular lattice is in a trivial insulating phase. When SOC is included and dominates the ISB, the Dirac points exhibit a non-trivial topology, which is accompanied by the ABAB stacking of the orbital angular momentum (OAM). This is, however, directly translated to the flipping of the charge localization. In Fig. 4.3c the LDOS and the indium orbitals from one unit cell including their total phase consisting of Bloch and orbital phases, are displayed. The charge localization in the energetically favored halve of the unit cell can be explained by the interference of the lattice Bloch wave functions. Around each atom, an $e^{\pm i\Phi}$ angular dependence occurs [9]. The constructive interference of the phases in halve B (indicated by green arrows), provides a charge localization in this halve [9]. This leads to an overall charge localization reminiscent of a honeycomb as shown in 4.3c.

The alternating charge localization between the two halves of the indenene unit cell can be probed by STS. The dI/dV maps for each of the K point valley states (two VB and two CB) were taken. At first, the positions of the indium atoms were calibrated. The bias voltage is set to 300 mV, where the p_z states are dominating [9]. Here the charge is localized above the In atoms and thus allows to identify their positions. Afterwards the bias voltage is gradually reduced and the p_{\pm} states, which are dominating at the Dirac points, prevail [9]. At 190 mV the charge localization is obtained at the halve B of the indenene unit cell and the conduction band CB+1, which is depicted on the right-hand side in Fig. 4.4 is dominating. By further lowering the bias voltage, the charge localization flips to A (CB), then to B (VB) again and in the end to A (VB-1). This alternating

charge localization, when following the K point valley states, is in good agreement to the corresponding DFT calculation for a QSHI [9].

Even though a new type of large-gap QSHI could be realized, it is not applicable for ex-situ transport measurements or electronic devices as it oxidizes in air. This major challenge may be overcome via intercalation.

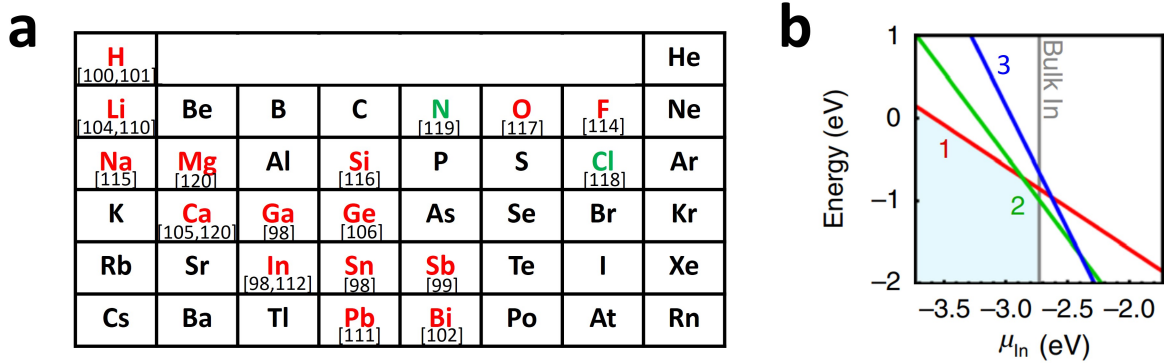


Fig. 4.5: **a** Main group of the periodic table of elements with the calculated (green) and intercalated materials in the graphene/SiC interface. **b** Equilibrium-phase stability calculations leading to intercalated bilayer and monolayer indium. Taken from Ref. [98].

4.3 Indium intercalation

Intercalation is the inclusion of materials into an interface of layers. In this work, indium is intercalated into the SiC/graphene interface. The principle of intercalation is well known and has been performed with a wide range of materials [99]-[120]. In Fig. 4.5a the main group of the periodic table of elements is displayed. The materials that have been already theoretically calculated (green) and successfully intercalated in the graphene/SiC interface (red), are marked. The intercalation was not only done with main group elements, but also with gold [109] and copper [108], to name just two of many. Today, almost all of the intercalation works focus on the changes of the graphene properties, due to the decoupling with various materials. In this framework, indium was also intercalated, but only as a bilayer or a $(\sqrt{3} \times \sqrt{3})R30^\circ$ reconstruction [98, 112]. Therefore, the (1×1) indenene structure was up to now not unambiguously identified as an intercalant so far. The big advantage, compared to all publications so far, is that both, capped and uncapped indenene could be realized and the properties of the intercalated version can be compared side by side to the pristine one.

Having presented the recipe for the growth of indium on SiC, the focus now turns to the intercalated system. Briggs *et al.* successfully intercalated a bilayer of indium beneath three graphene layers [98]. In their work, they also calculated the preferred number of

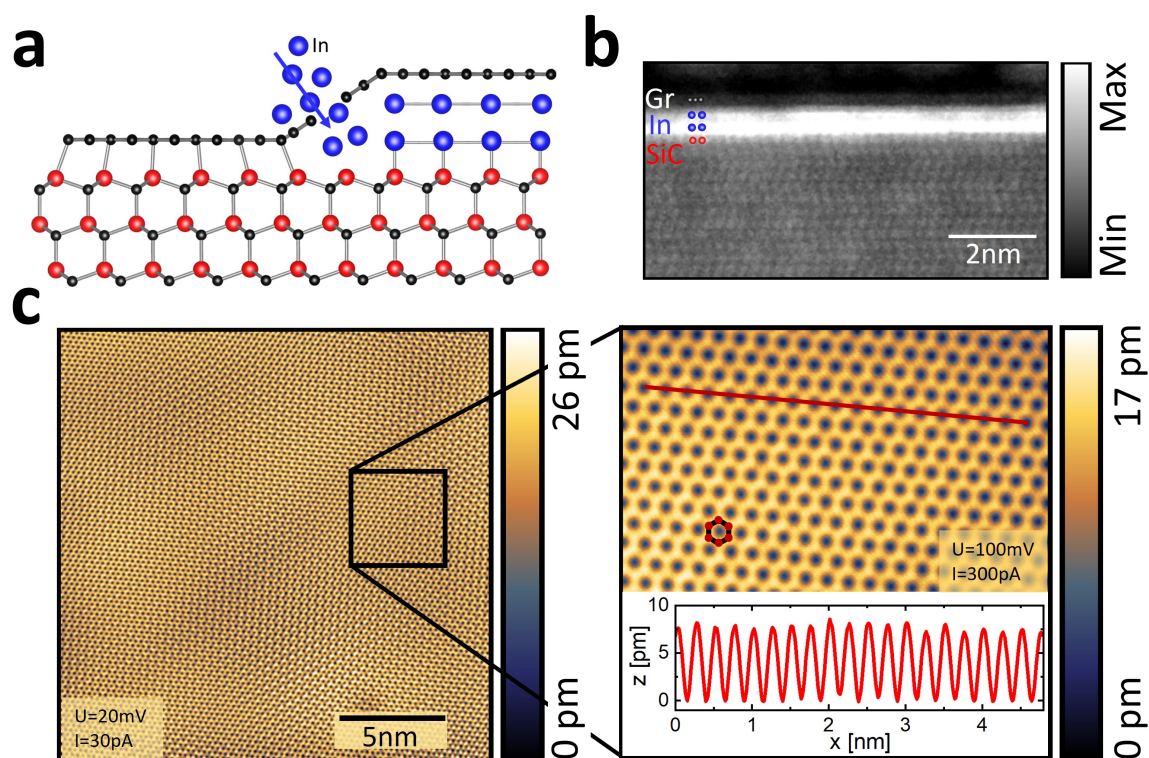


Fig. 4.6: **a** Ball-and-stick model indicating the intercalation process through a defect in the graphene lattice. **b** STEM showing two indium layers between the 4H-SiC(0001) substrate and the graphene layer on top. **c** STM image from the decoupled ZLG forming a quasi-freestanding graphene lattice. The red circles point out the carbon atoms.

layers that will form in the graphene/SiC interface, due to energy minimalization. The results of the first-principle equilibrium phase stability calculations are displayed in Fig. 4.5b. Here, the energy as a function of the chemical potential μ_{In} for the different indium layers (red, green and blue for one, two and three layers, respectively) is depicted. The vertical grey line at around $\mu_{\text{In}} = 2.25 \text{ eV}$ corresponds to the chemical potential of the bulk indium [98]. Below this value, a 2D material can emerge due to the strong metal-SiC bonding, above which In bulk formation is favored. The area in which an intercalated 2D material can form is highlighted in light blue. For each chemical potential in this area, the lowest line (red, green, blue) indicates the most stable numbers of indium layers. As displayed in Fig. 4.5b the intercalated indium will form one or two layers. According to the theoretical calculations, the realization of the monolayer indenene is therefore possible.

The intercalation process has been done with various intercalation techniques in different works. It is common to begin with the growth of graphene on top of the SiC and then intercalate foreign atoms by annealing steps during evaporation [112, 113]. It is important, that the graphene has some defects, where the In atoms can penetrate into the graphene/SiC interface, as shown schematically in Fig. 4.6a. Another technique is grow-

ing the graphene defect-free and in a second step generating defects on purpose using an O_2/He plasma [98]. Furthermore, heavy elements, like Bi, have been intercalated via ion implantation [121]. Here, the foreign ions are accelerated to high energies with an e-beam evaporator and due to their sputtering at the surface, vacancies in the graphene lattice are created, where the ions can intercalate [121]. Not only the intercalation technique itself can be different, but also the starting point. While mostly the buffer layer graphene on top of the substrate is grown [112], an alternative route is to start with the mono- or even a bilayer graphene [113]. It does not depend on the atomic species, because the indium intercalation has been done through the ZLG [112] as well as through a bilayer graphene on top of the buffer layer [98]. With the knowledge of the three different graphene growth methods (ZLG, MLG and BLG), which have been discussed in chapter 3, the intercalation process is feasible with all of the three starting conditions. During this work, it was found that the most homogeneous intercalation could be achieved, by intercalating through the ZLG. Therefore, all the further results in this work were obtained from samples generated by this procedure. After the buffer layer graphene growth, the intercalation processes in two steps, as discussed in chapter 2.1. Similar to the results from Briggs *et al.*, an indium bilayer has formed below the graphene after the intercalation. The two indium layers can be clearly seen in the corresponding TEM measurement in Fig. 4.6b. Above the well-ordered SiC substrate, where the silicon atoms can be resolved, a bright signal of the heavier indium is apparent. For a STEM measurement applies that the higher the atomic number Z , the brighter the signal [55,56]. This is also the reason why the graphene on top of the indium layers can only be seen with difficulty as carbon only has $Z = 6$. After the intercalation, the ZLG is decoupled from the SiC substrate and a quasi-freestanding graphene layer is formed. This graphene monolayer is shown in an STM image in Fig. 4.6c. Different to the monolayer graphene on SiC, no buffer layer is seen. This confirms the decoupling through the intercalation. In the inset, a graphene honeycomb including the carbon atoms in red is displayed. The line profile in red indicates a lattice constant of around 2.51 \AA , which is comparable to the literature value [41]. Slight deviations can result from the STM stage calibration. Therefore, STM is not the method of choice for determining the lattice constant, but diffraction experiments.

4.4 Roadmap to indenene intercalation

As seen in the STEM images in Fig. 4.6b, indium has been successfully intercalated below the graphene. The ZLG is decoupled from the SiC substrate and thus turns into a quasi-freestanding MLG, as shown in Fig. 4.6c. However, this work aims to specifically cap the QSHI indenene, with its monolayer (1×1) structure. Therefore, the currently existing system must be reduced by one layer. As in the case of the pristine indenene,

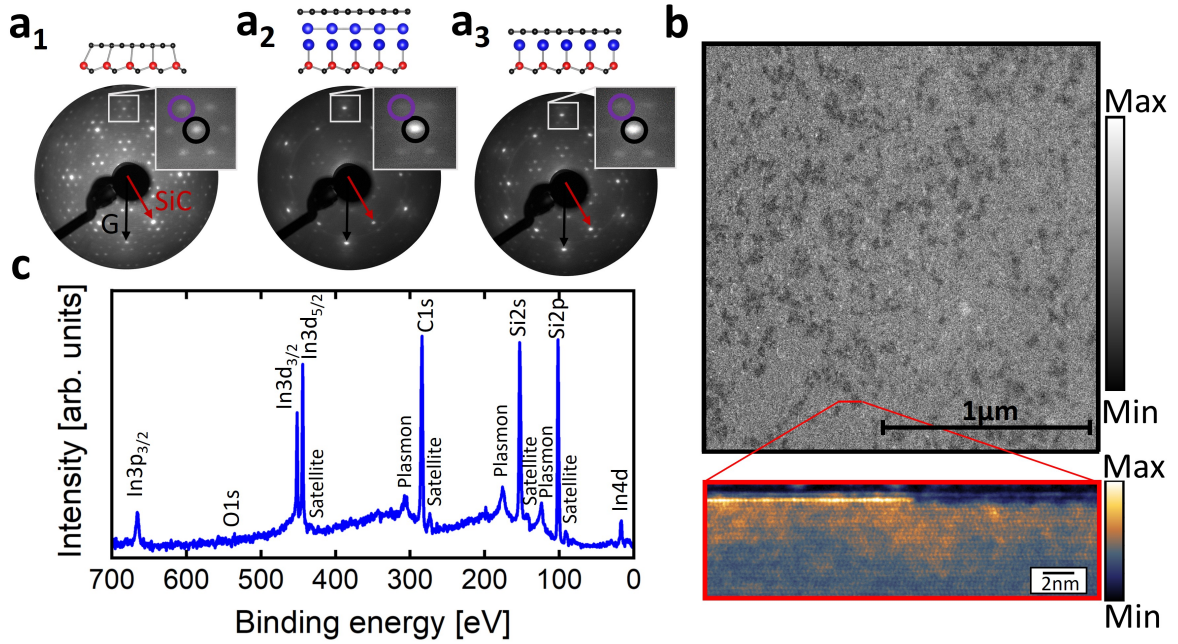


Fig. 4.7: **a** LEED image taken at 80 eV, showing the three phases towards the indenene intercalation. The inset reveals the ZLG decoupling, since the $(6\sqrt{3} \times 6\sqrt{3})R30^\circ$ reconstruction spots nearly vanished. **b** Large scale SEM (STEM) image of the intercalated system at the top (bottom) reveals a 75% indium intercalation-covered sample. **c** XPS overview scan indicates no contamination.

the idea is to transform the bilayer into a monolayer by post-annealing. It has been found, that temperatures of around 580 °C are sufficient to evaporate the indium atoms through the graphene capping layer to form the monolayer of indium. In Fig. 4.7a the LEED images, taken at 80 eV, for the ZLG and the two intercalated phases are displayed. The LEED image of the buffer layer graphene (a₁) was already discussed in chapter 3.2.2. Besides the (1×1) spots of the substrate (red) and graphene (black), the $(6\sqrt{3} \times 6\sqrt{3})R30^\circ$ reconstruction spots are visible. In the inset, six spots of the $(6\sqrt{3} \times 6\sqrt{3})R30^\circ$ reconstruction (purple) around the graphene (1×1) spot are observed. After the indium intercalation and the associated buffer layer decoupling the $(6\sqrt{3} \times 6\sqrt{3})R30^\circ$ spots vanished almost completely. Here, the indium atoms are bond to the topmost silicon atom and a quasi-freestanding graphene layer caps the system. The inset in 4.7a reinforces this statement, because of the brighter graphene (1×1) spot and the disappearing ZLG spots. After post-annealing at 580 °C for 30 min, the monolayer indenene has formed. This is demonstrated in Fig. 4.7b (bottom). Here, the STEM image of the sample is shown. Here the graphene capping layer as well as the monolayer indium can be resolved. A detailed STEM study of this system will be discussed later in chapter 4.5. So far, the number of intercalated indium layers can be precisely controlled, by simply post-annealing the sample after the intercalation process. In the LEED image of the intercalated indenene

sample (a_3) the brightness of the SiC (1×1) spots increases compared to the bilayer indium. The reason for that is the well-ordered (1×1) periodicity of indenene above the SiC. However, as the $(6\sqrt{3} \times 6\sqrt{3})R30^\circ$ reconstruction spots are slightly visible again, there are also areas on the sample where the indium is completely evaporated and the quasi-freestanding graphene forms back to a ZLG. This phase is also obtained at the right-hand side of the STEM image. According to the SEM image in Fig. 4.7b (top), the percentage of intercalated indium is about 75% of the sample surface. The dark spots correspond to the buffer layer graphene, whereas the bright area belongs to a successfully intercalated monolayer. The purity of the intercalated indenene film can be determined by the chemical composition of the sample measured with XPS. Besides, the core levels that are related to indium, silicon and carbon in Fig. 4.7c, no contaminations can be found. Therefore, the high purity of the sample can be confirmed. The peaks that are not assigned to a core level are marked as plasmons or X-ray satellite peaks. The X-ray satellite peaks arise due to the non-monochromatic X-ray source in the homelab. Besides the predominant Al $K\alpha_{1,2}$ line, the sample is also irradiated with the less intensive Al $K\alpha_3$ line, which has a 9.7 eV lower energy than the main line and only 7% of its intensity [122]. The plasmon peaks are due to the scattering of the photoelectrons with plasmons in the sample. Therefore, the photoelectrons lose a distinct amount of kinetic energy. An energy loss peak is obtained and labeled as “plasmon” in Fig. 4.7c [122].

4.5 Electronic properties of the intercalated indenene

After the intercalation and the post-annealing, STEM images reveal the presence of the monolayer of indium and LEED measurements display its (1×1) structure. However, the question remains, whether the intercalated indenene also features the same electronic and topological properties under the capping as its counterpart without graphene. Therefore, all four indium phases, i.e., bilayer and monolayer each with and without graphene, were grown. To exclude doping variations among different substrates samples, they were recycled by repeated H-etching [10], i.e., all four combinations on the very same SiC substrate are investigated. An ARPES band map of all of these 2D materials along the indium $K_{\text{In}}\Gamma M_{\text{In}}$ high symmetry path is depicted in Fig. 4.8. The path of the ARPES mapping is also shown in the bottom of the left band map. As displayed in LEED, the graphene Brillouin zone is larger and rotated by 30° . Therefore, the indium $K_{\text{In}}\Gamma M_{\text{In}}$ mapping direction is equivalent to the graphene $M_{\text{G}}\Gamma K_{\text{G}}$ high symmetry path. Each band map includes both, graphene and indenene, M and K points as well as the Γ point. The first (second) row shows the indium coverages without (with) a graphene capping. Each column corresponds to the same number of indium layers, where on the right-hand (left-hand) side the monolayer (bilayer) is depicted. In the left corner of each panel, the

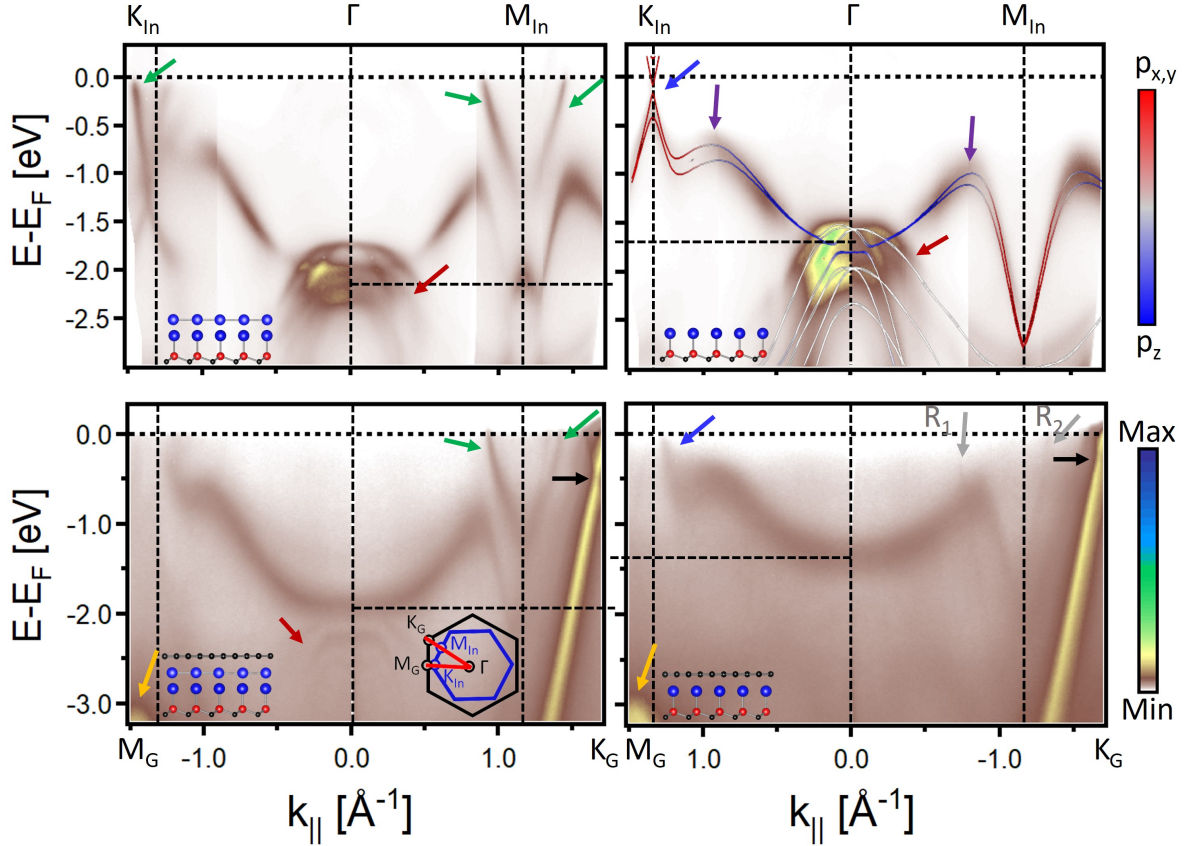


Fig. 4.8: ARPES band structure of the two indium coverages without (upper row, $h\nu=21.2$ eV) and with (lower row, $h\nu=46$ eV, logarithmic color code) a graphene capping along the $K_{\text{In}}\Gamma M_{\text{In}}$ high symmetry path. The bands of bilayer indium (left column), as well as the indenene (right column), show no significant differences with the additional graphene layer, apart from slight doping. The orange and black arrows indicate the graphene M and K point, the red arrow the SiC bands and the green one the additional metallic indium bands for the bilayer case. For the pure indenene DFT calculation are overlaid showing the gapped Dirac states at the K point (blue arrow). The blue and red color-coded bands in the calculation correspond to p_z and a $p_{x,y}$ orbital character, respectively. The purple arrows indicate the $p_z - p_{x,y}$ hybridization points.

investigated system is displayed. In addition, the DFT calculation for pristine indenene was superimposed on the ARPES band structure. The corresponding bands are marked in blue (p_z orbital) and red ($p_{x,y}$ orbitals). The white bands, positively curved below -1.5 eV correspond to the SiC substrate. These bands are indicated with a red arrow. Due to the SOC, a topological non-trivial energy gap opens at the K point (blue arrow), where the $p_{x,y}$ -orbital character is dominating, as discussed in chapter 4.2. The purple arrows indicate the hybridization point of the in- and out-of-plane orbitals, that mark the onset of the large hybridization gap that is necessary for a global gap opening [97]. The band structure of bilayer indium shows a similar dispersion as the indenene, but additional bands appear (green arrow). These bands prevent a global energy gap, due to the crossing with the Fermi level, making the bilayer metallic.

The band structures for the two intercalated systems are depicted in the bottom row of Fig. 4.8. With high intensity, the quasi-freestanding graphene bands around the M and K point (marked with an orange and black arrow, respectively) appear next to the rather weak indium bands. Since ARPES is surface sensitive, as described in chapter 2.2.2, the SiC signal is attenuated by the additional graphene layer. The linear bands from this layer are also replicated, as indicated by the gray arrows. These replicas appear, due to Umklapp scattering of the emitted electrons with the underlying lattice structure [123]. The first replica (R_1) originates from the scattering by the reciprocal In 1×1 lattice vector K_{In1x1} , whereas the second replica (R_2) is due to the scattering by $K_{gr1} + K_{gr2} - 2K_{In1x1}$, where $K_{gr1,2}$ are the graphene reciprocal lattice vectors. These replicas are also observed at various intercalated systems [124, 125].

Nevertheless, the band structure under the capping remains for both 2 and 1 ML In systems. In the bilayer case, the nearly free electron dispersion indicated by the green arrow is preserved as well as the linear dispersion of the intercalated indenene around the K point (blue arrow). Another striking difference between 2ML and 1ML In is the p -band minimum at the Γ point, which is shifted around 0.5 eV to higher binding energies for the monolayer indium compared to the bilayer, as indicated with horizontal dashed lines. This behavior is also seen after graphene capping. Nevertheless, the graphene layer on top leads to a slight p -doping of the band structure. Interestingly, this brings the indenene band gap slightly above the Fermi level. All the publications so far showed a metallic behavior, due to the occupied conduction band [9, 97]. The indenene samples from the published ARPES data and the band structure in Fig. 4.8 were produced on the same n -type (0.01-0.03) Ωcm PRIME wafer substrates.

Fig. 4.9 compares the indenene K point for the intercalated indenene with the pristine indenene sample. The special topological properties of indenene originate from the large non-trivial band gap at the Dirac point. The EDC including the peak-fits reveal the two valence bands (VB-1 and VB) and the first conduction band (CB), as illustrated in Fig. 4.9a. The second conduction band lies above the Fermi level and is therefore not accessible by ARPES. The peak fit maxima result in an energy gap of around 100 meV. In Fig. 4.9b the ARPES spectra of the intercalated sample around the Dirac point is depicted. Due to the scattering with the graphene layer on top of the QSHI indenene, the band is more washed out, as for the uncapped indium layer. Nevertheless, the linear band dispersion around the Dirac crossing point is still preserved after the intercalation. The p -doping of the indenene caused by the graphene capping, results in valence band maxima slightly above the Fermi level. A detailed doping study can be found in chapter 4.7.

Based on the good agreement between indium layers with and without graphene capping, it can be concluded, that the intercalated indenene features the same electronic properties as pristine indenene, except for a p -doping. But there is not only a difference in the indium

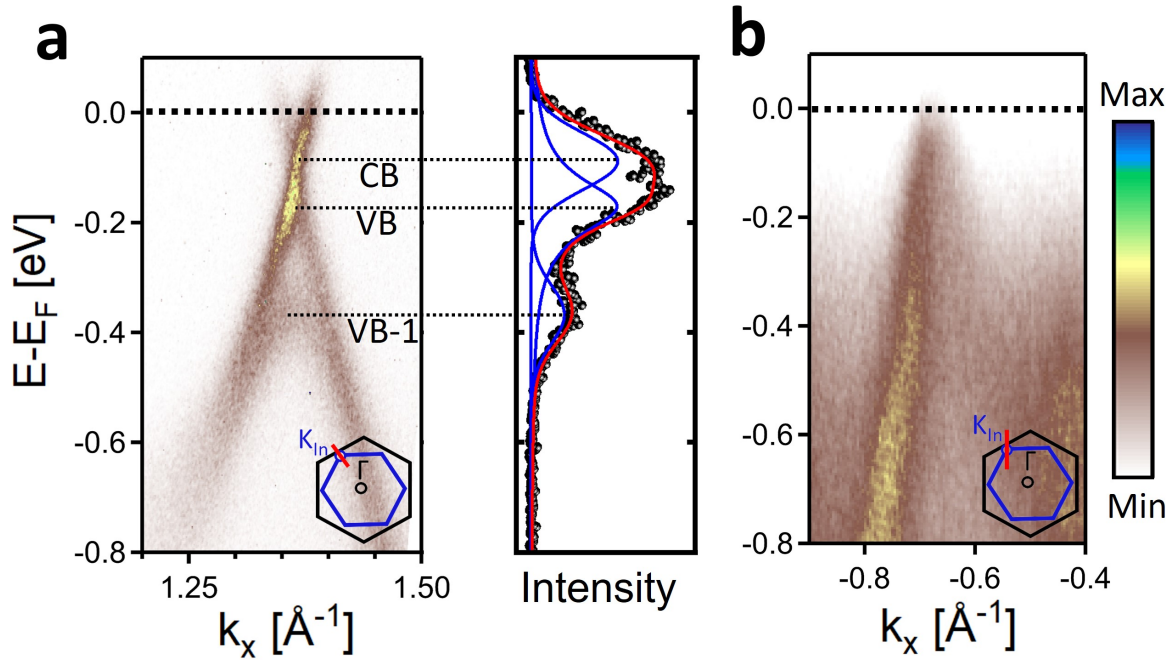


Fig. 4.9: **a** RT ARPES spectra of the indenene Dirac crossing point with the EDC and its peak-fit indicating a band gap between the lower conduction and upper valence band. **b** RT ARPES band structure around the intercalated indenene K point.

band filling after the intercalation, but also the graphene is affected. In the ARPES spectrum in Fig. 4.8 a graphene doping is observed. When one layer of indium is removed, the graphene gets slightly p-doped and the graphene M point bands (orange arrow) as well as the K point bands (black arrow) are shifted to higher energies. This doping effect at the graphene K point for both indium coverages is depicted in Fig. 4.10. The upper row (a) shows a high-resolution ARPES measurement around the graphene Dirac point for the bilayer indium intercalated sample, with the mapping direction depicted in the center of Fig. 4.10b. Here the MDCs including the fitted Voigt peak maxima (red dots) are displayed on the right. From a linear fit through these data points, the energy of the Dirac point below the Fermi level can be determined to $E_D = -0.51$ eV. After annealing the sample and thereby the reduction of one indium layer, the ARPES spectrum is displayed in Fig. 4.10b. Through an analog analysis based on the MDCs, the energy of the Dirac point is 0.28 eV below the Fermi level. Therefore, a shift by 0.23 eV to higher energies is observed when the number of indium layers is reduced. A similar change in the charge transfer to graphene upon post-annealing of intercalated indium was observed in an earlier study, however, the group was not able to determine the number of indium layers [112]. With the knowledge based on STEM and ARPES, shown in this work, the thickness of the indium layer can be determined unambiguously. Judging from the Dirac point position in ARPES, the sample in [112], defined as incompletely intercalated, probably has a bilayer

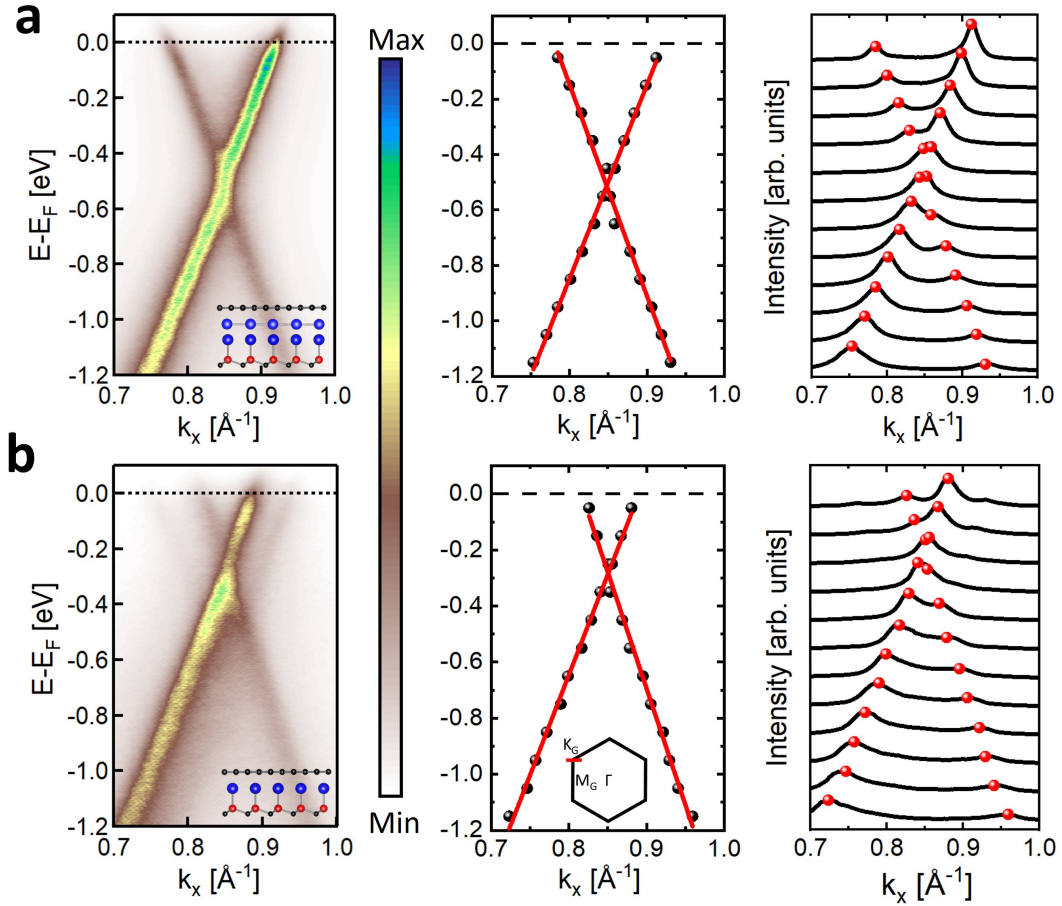


Fig. 4.10: ARPES spectra ($h\nu=46$ eV at RT) around the graphene K point for the **a** bilayer indium and **b** indenene intercalated sample on the left. The corresponding MDCs with their peak fitting maxima (red dots) on the right and a linear fit through these peak positions in the middle. By removing one layer of indium, the band filling of graphene changes by 0.23 eV.

indium coverage and the sample after eight intercalation steps could be the monolayer. Then the measured Dirac point energies of 0.58 eV and 0.33 eV below the Fermi level would be in close agreement with the previously presented results in Fig. 4.10. The charge carrier density $n = \frac{k_F^2}{\pi}$ of the two graphene layers can be calculated using the Fermi wave vector k_F . With the reduction of one indium layer the charge carrier density is decreased from $n = (16.2 \pm 4.6) \cdot 10^{12} \text{ cm}^{-2}$ for the bilayer of indium to $n = (3.5 \pm 2.6) \cdot 10^{12} \text{ cm}^{-2}$ in the intercalated indenene sample. Compared to hydrogen intercalated graphene, where the Fermi level is about 100 meV below the Dirac point [100], both graphene layers in Fig. 4.10 are highly n-doped. As no H-related doping is expected, we attribute the n-type band filling of graphene to charge transfer from indium as similarly concluded for other intercalation studies [123, 124]. A similar charge transfer to graphene was reported for Au-intercalation, yet p-doping for 2ML and n-doping for 1ML gold [124].

4.6 Heat and oxidation stability of indenene

Based on PES, STEM and LEED the intercalated monolayer indium remains not only structurally, but also electronically identical compared to the uncapped indenene. Therefore, it is expected that the graphene has no influence on the indenene and is freestanding above the quantum material. For ex-situ measurements, like Raman spectroscopy or transport measurements, the indenene sample must be stable in air. Thus, an oxidation study for both systems was performed, which is depicted in Fig. 4.11a. On the left-hand side, the pure indenene with its doublet In 3d core level spectra and on the right-hand side the intercalated indenene XPS spectra are displayed. The black curves belong to the as-grown indenene samples. This was grown and measured in the UHV with a pressure of lower than $2 \cdot 10^{-10}$ mbar. Afterwards, the two samples were gradually exposed to oxygen. The oxygen exposure was determined in units of Langmuir L . Langmuir is a unit that corresponds to the exposure of a surface to a gas and is defined by the exposure of 1 torr for 1 μs [126]. For pure indenene, a peak shift of around 1.5 eV to higher binding energies is observed, when increasing the oxygen exposure. This also implies that indenene is not stable in air. In contrast, the intercalated indenene shows no peaks shift even when the sample is taken out of the vacuum and exposed to ambient conditions for a few minutes. Conclusively, the graphene layer protects intercalated indenene from oxidation and makes ex-situ measurements possible.

In Fig. 4.11b, the influence of heat treatment of the two systems is shown. With increasing substrate temperature, more indium evaporates from the indenene sample and the In 3d core level spectra lose intensity. After post-annealing at 650 °C, no indium remains on the sample. Like in the previous case a small peak shift is detected and displayed depending on the temperature in the inset of Fig. 4.11b. This peak shift is potentially explained by a surface photovoltage (SPV) effect, caused by the X-ray source [127]. In equilibrium, the metallic layer on top of an insulating substrate leads to a band bending at the surface. When the incident light through the X-ray source creates electron-hole pairs, the system is in a non-equilibrium state as these pairs require a certain time to recombine. In a n-type situation, such as given for the SiC substrates, the bent potential draws the electrons into the bulk and therefore the holes have to compensate the space charge at the surface. This causes a uniform shift of all core levels, being substrate or adsorbate related, which can be seen in Fig. 4.11b on the left-hand side [127]. M. Alonso *et al.* demonstrated, that the SPV effect also depends on the metal capping thickness [127]. When heating the degenerately doped indenene, the indium coverage is reduced.

On the right-hand side, the In 3d core level for the intercalated indium for different post-annealing temperatures is shown. Therefore, the graphene capping layer protects the indium not only from oxidation but also from deintercalation due to heat. Even at 1000 °C,

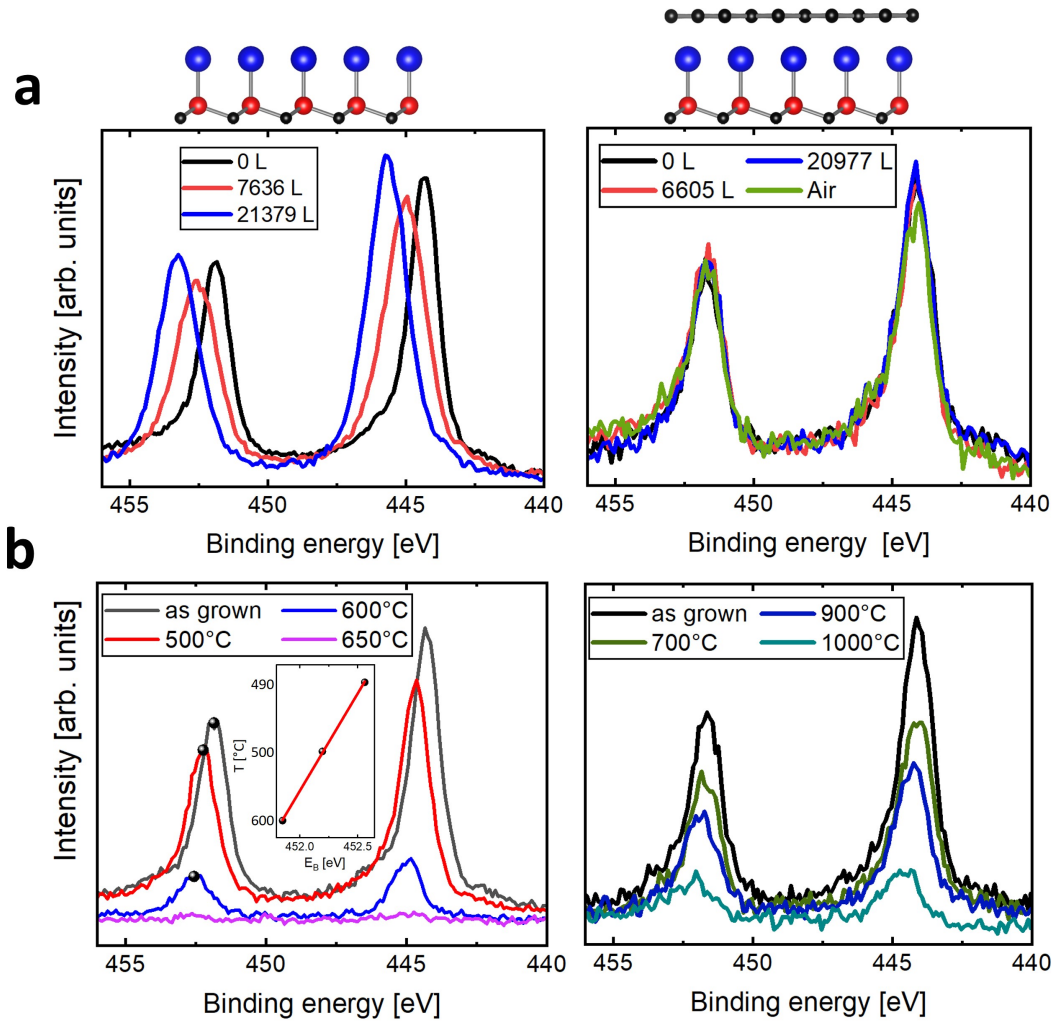


Fig. 4.11: **a** XPS spectra of the In 3d core level peak after oxygen exposure, showing that the pristine indenene sample (left) oxidized whereas the graphene layer on top of the QSHI (right) protects the indenene from air. **b** Comparison between indenene without (left) and with (right) a capping layer when post-annealing the sample. The graphene layer ensures that even at 1000 °C indium remains at the sample. The inset on the left-hand side shows the influence of a potential surface photovoltage effect for the decreasing coverage of the pristine indenene.

the indium is preserved in the graphene/SiC interface. Similar to the pure indenene at ever higher temperatures, the LEED image of the intercalated sample reveals slight $(\sqrt{3} \times \sqrt{3})R30^\circ$ reconstruction spots.

Since XPS confirms that the indenene is protected from oxidation by the graphene layer, transport measurements that could show the topological properties of indenene, could also be carried out. For this purpose, the sample has to be brought out of the UHV system to bond the contacts in ambient conditions. But there is a drawback with this system. To measure the QSH effect for indenene at RT, the capping should be insulating to avoid transport contributions from the capping layer. Unfortunately, graphene is, as already discussed, metallic and therefore not suited for transport measurements. A possible insu-

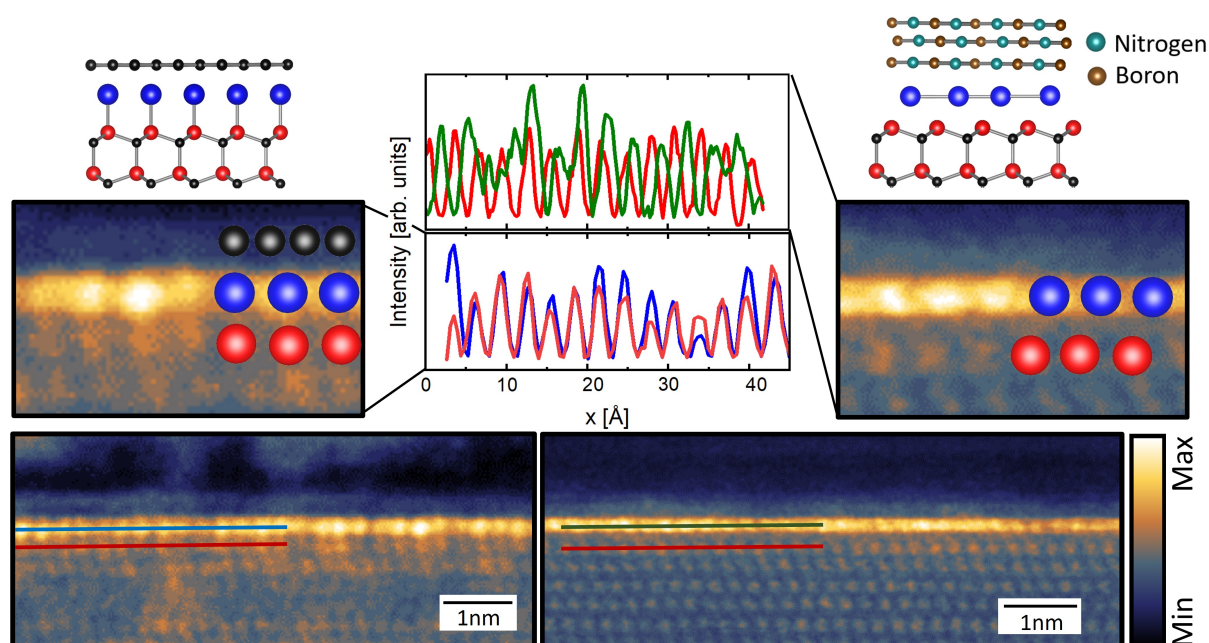


Fig. 4.12: STEM images of the intercalated indenene sample (left-hand side) and after growing boron nitride on top of the indenene (right-hand side). The two line profiles demonstrate a peak shift of the indium atoms, when the sample oxidizes, compared to the unoxidized case where each In atom sits exactly on top of a Si atom.

lating capping would be boron nitride.

Based on the successful graphene capping method, it is possible to determine the oxidation behavior of indenene under any material using STEM. On the left-hand side in Fig. 4.12 a non-oxidized indenene, e.g. by intercalation in the graphene/SiC interface, is depicted. As expected, each indium atom sits exactly above a silicon atom. This is again highlighted by the line profiles through the indenene (blue) and uppermost silicon (red) layer. In the STEM image on the bottom, the monolayer graphene on top of the QSHI is well resolved.

To study an insulating capping, first attempts of growing boron nitride on top of the monolayer indium were done. However, the insulating capping does not protect the indenene from air yet. The inset on the right-hand side in Fig. 4.12 and the line profiles in green and red display, that the indium atoms shift in-plane when oxidizing. Using STEM it is now possible to determine whether the indenene is oxidized or not. These measurements are in good agreement with the literature, which reveals a similar in-plane shift of the indium atoms for a 1 nm thick indium coverage on top of a SiC substrate [97]. On the other hand, for a non-oxidized bilayer indium with a graphene capping on top, no shift of the indium atoms is observed [98].

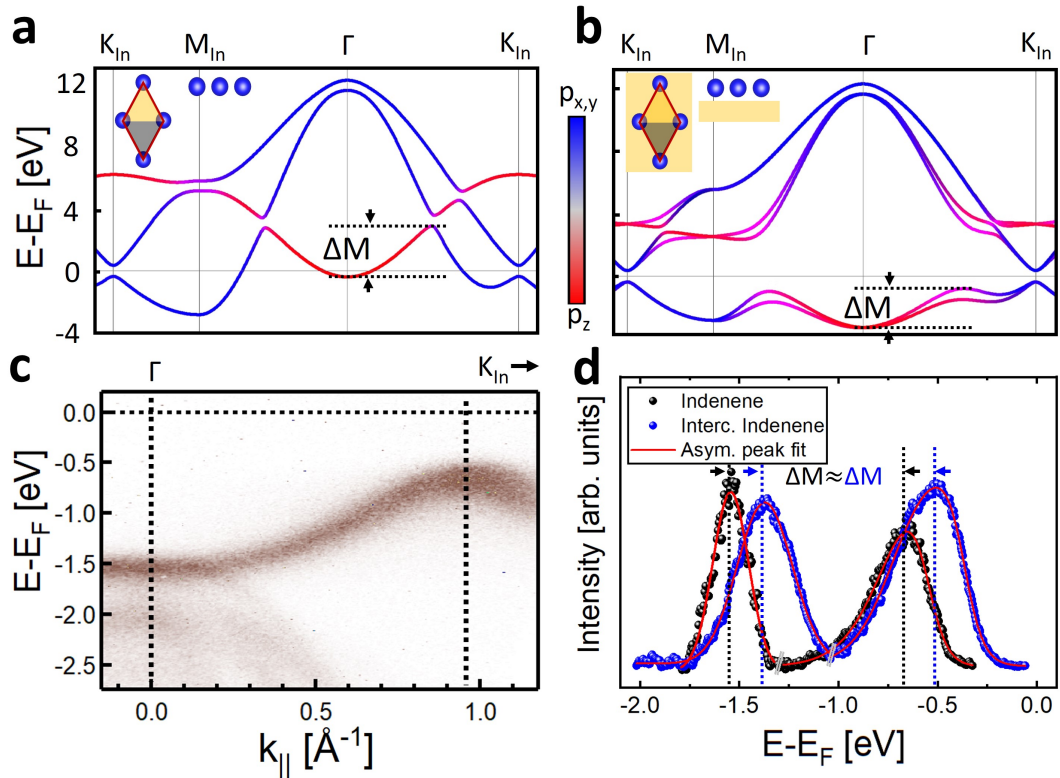


Fig. 4.13: **a** Tight binding model for a triangular monolayer with p -orbital character with **a** no and **b** large influence of the mirror symmetry break (MSB). A large MSB opens the hybridization gap and due to SOC, the system exhibits a topological non-trivial phase. **c** ARPES spectra ($h\nu=40.8$ eV at RT) of the pure indenene sample along the ΓK direction. **d** Black: EDCs indicated in **c** with dashed black lines. Blue: ECDs from the intercalated system in Fig. 4.8.

4.7 Topological properties of intercalated indenene

So far, the intercalation of the monolayer indium into the graphene/SiC interface was presented. Using LEED, the same (1×1) structure as for the pristine indenene was determined. Additionally, the ARPES spectrum confirms, that the indenene band structure is qualitatively preserved. This chapter finally aims to examine the conservation of the topological properties of the intercalated indenene. Fig. 4.13a shows the tight binding model for a triangular monolayer with p -orbital character according to Ref. [9]. Due to strong SOC, a band gap opens at the Dirac point. This model senses a freestanding indium lattice, without a substrate, as indicated at the top of Fig. 4.13a. Hence, due to the bands crossing the Fermi level this system is metallic. With ever-increasing presence of a homogeneous substrate, the strength of the MSB gets larger and the hybridization of the p_z and the $p_{x,y}$ orbitals opens an energy gap. This is displayed in Fig. 4.13b. The system represents a 2D TI. By increasing the strength of the out-of-plane MSB, the relative distances ΔM between the Γ point and hybridization point in the ΓK direction change.

This is shown with horizontal dashed lines in Fig. 4.13a,b. It allows to identify changes of in MSB for the intercalated indenene sample and can be compared to the pristine indenene. To suppress the SiC bands in the pristine indenene ARPES spectra, the band map along the ΓK high symmetry path was measured with the He II line and is depicted in Fig. 4.13c. The EDCs around the Γ point and the hybridization point for pristine and intercalated indenene samples are shown in Fig. 4.13d. Except for a general p-doping of around 0.17 eV, no significant change in the distance ΔM is observed. The size of this doping is also reflected in the shift of the indenene K point in Fig. 4.9. Therefore, the shift of the Dirac point is due to doping and not caused by a change in the MSB. Thus, the graphene layer on top of the QSHI does not change the strength of the MSB and the associated size of the hybridization gap.

LEED, STEM and PES indicate no change between the capped and uncapped indenene. However, due to the SiC substrate, also the ISB has to be taken into account. When the strength of the ISB λ_{ISB} is greater than the strength of the SOC λ_{SOC} , the system is in a topological trivial phase [9]. As λ_{ISB} depends on the In-Si bond distance d , normal incidence X-ray standing wave (NIXSW) experiments were performed to compare the In-Si bond length with and without a graphene capping.

The first step of this experiment is to identify all the relevant atomic species. This is done by an XPS spectrum exemplarily shown in Fig. 4.14 for the In 3d core level. The In 3d core level peak exhibits a shoulder, which could be caused by oxidation. For the preparation, the sample was exposed to air and was then transported for a few days in static vacuum ($\sim 10^{-5}$ mbar) to the synchrotron facility. However, such asymmetric peak is also observed for unoxidized pristine indenene samples [97].

In the XSW experiment the X-ray beam forms a standing wave, due to interference of the incident and reflected light, when the Bragg condition is fulfilled. The resulting standing wave is selected to ensure its periodicity is the same as the SiC substrate, with its bulk lattice spacing of $d_{\text{SiC}} = 2.52 \text{ \AA}$ [66]. Changing the photon energy $E = h\nu$ around the Bragg condition from around -2.5 eV to 3 eV, the phase $\Phi(h\nu)$ varies from 0 to π . This implies a shift of the standing wave nodes by half of the bulk lattice spacing. In this case, the photoelectron spectra for 47 different photon energies for the bulk materials (Si 2s and C 1s_{SiC}), the graphene (C 1s_{Gr}) and the indenene (In 3d) were measured. The data including photoelectron yield curve fits according to

$$Y(h\nu) = 1 + R(h\nu) + 2\sqrt{R(h\nu)}f_{\text{H}} \cdot \cos(\Phi(h\nu) - 2\pi P_{\text{H}}), \quad (4.6)$$

are displayed in Fig. 4.14 [128]. Besides the X-ray reflectivity $R(h\nu)$, two fitting parameters can be obtained. The coherent position P_{H} gives the position relative to the Bragg plane. Thus, the In-Si bond length can be determined. On the other hand, the coherent

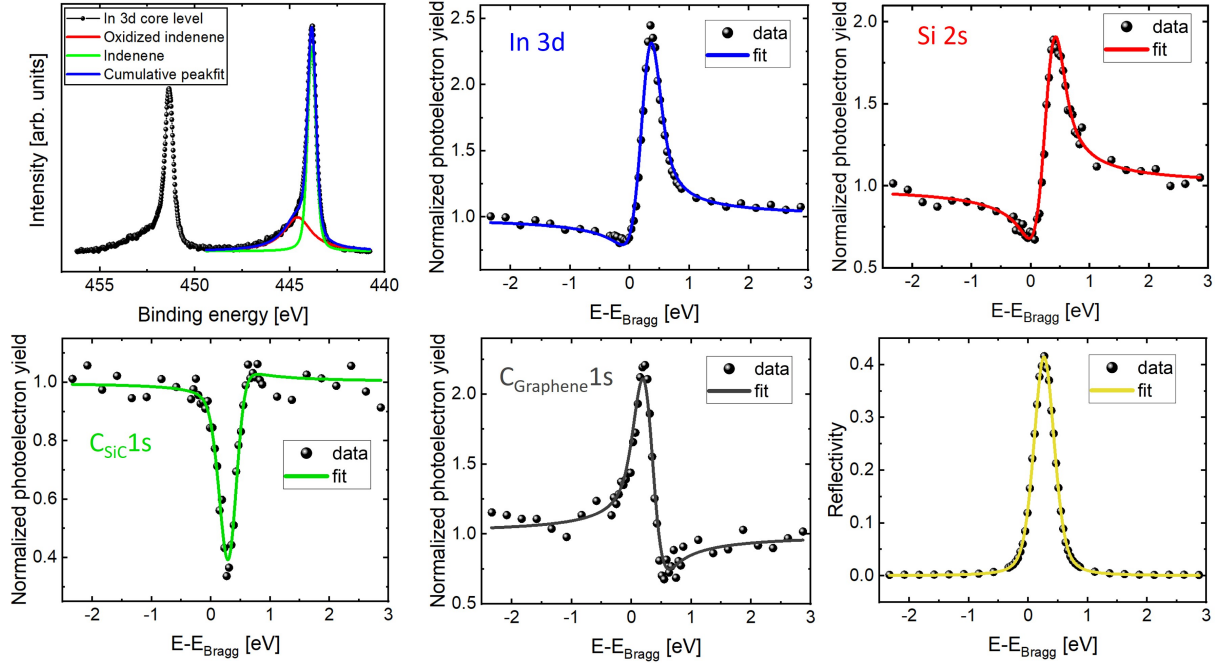


Fig. 4.14: Exemplary In 3d core level spectra to identify all the relevant components of the spectra. NIXSW yield curves of the In 3d, Si 2s, the two carbon species (SiC bulk and graphene) as well as a reflectivity lead to the coherent positions and fractions listed in 4.1.

fraction f_H indicates the order of the system. Both values are between 0 and 1, where the case of $f_H = P_H = 1$ displays well-ordered adsorbates on top of the SiC with the same lattice spacing as the substrate. The average fitting parameter from the photoelectron yield curves are listed in Tab. 4.1. The fitting parameter have an uncertainty of ± 0.005 and the measurement was done on two different positions of the sample. The error was determined with the largest error estimation.

Element	Coherent position [\AA]	Coherent fraction [\AA]	z [\AA]
Si	(1.0000 ± 0.0050)	(0.955 ± 0.020)	(0.000 ± 0.011)
C_{SiC}	(0.7500 ± 0.0050)	(1.075 ± 0.010)	(0.630 ± 0.011)
C_{Gr}	(0.415 ± 0.010)	(0.810 ± 0.035)	(6.086 ± 0.023)
In	(0.090 ± 0.015)	(1.100 ± 0.025)	(2.747 ± 0.038)

Table 4.1: Average coherent positions and fractions as well as the adsorption height z for the different species determined by the peak fits of the NIXSW measurement in Fig. 4.15.

As expected, the coherent position of the Si atoms is equal to 1.00. This indicates that the measurement has been calibrated accurately. The coherent fraction of the indenene layer with 1.10 is close to the optimal value of 1.00 and comparable with the coherent fraction of the Si layers with 0.955. This non-physically value above 1.00 is due to the known non-linearity of the analyzer. This effect has also been seen for the pure indenene sample and the intercalated Sb monolayer, which were measured at the same setup at the

beamline I09 of the Diamond Light Source Ltd. [9, 99]. However, the coherent position is not affected by this [99, 129]. The coherent fraction of the graphene layer is 0.81. It is significantly higher than the graphene values for the intercalated Sb with 0.71 and the hydrogen intercalation with 0.68 [99]. Therefore, it is assumed that the graphene layer on top of the QSHI is well-ordered. From the consideration of the coherent positions, the In-Si bond length and the distance from the QSHI to the graphene can be obtained. Here, it has to be mentioned, that if the coherent position is measured to be P_H , the height of the layer to be examined is $z = d_{\text{SiC}} \cdot (n + P_H)$, where n is an integer. A reasonable choice for n has to be made and cannot be concluded from the measurement. The indenene-substrate as well as the indenene-graphene distances are depicted in Fig. 4.15b.

A major advantage of this work compared to the published papers listed in Fig. 4.5b is, that both indenene systems, i.e. with and without the graphene capping were investigated. Most intercalation works so far report a freestanding graphene layer, which has no influence on the intercalant at all. Their drawback is, that no reliable statement can be made without the uncapped counterpart. In the case of indenene the two systems have been realized and the influence of the graphene can be considered. The distance between the QSHI and the graphene layer corresponds to $d = (3.339 \pm 0.044) \text{ \AA}$. This is about 92% of the van der Waals bonding distance, which is $d = 3.63 \text{ \AA}$ [130]. Therefore, and due to the presented ARPES data, it is expected, that the graphene has no influence on the indenene. However, comparing the two In-Si bond lengths of the capped and uncapped samples, a difference is observed. The graphene layer lifts the indenene by $\Delta d = (7.8 \pm 5.2) \text{ pm}$ to a higher In-Si bond length. Such changes in the bonding distance are important when considering intercalated systems theoretically, in particular, if they are as sensitive to this parameter as indenene is.

Fig. 4.15a shows the influence of the bond length on the indenene topology. The band structure of the indenene K point (top) is displayed for different distances d , as illustrated at the bottom. The first panel shows the indenene on top of a homogeneous substrate. As discussed before, due to the SOC, a non-trivial energy gap opens and the indenene reveals 2D TIs properties. In the case of the experimental realization, the monolayer of indium is grown on a 4H-SiC substrate. Therefore, the topmost carbon atoms render the halves A and B of the indenene unit cell inequivalent [131], which can be seen in the center of Fig. 4.15a. Looking at the panels step by step from the left to the right, the ISB term is reduced, which corresponds to a certain extent to increasing the Si-In distance. Therefore, the strength of the ISB λ_{ISB} clearly depends on the In-Si bond length. As discussed before, the ISB counteracts SOC and the relative strength of both define whether the indenene is in a topological trivial or non-trivial phase. This is illustrated in the tight binding calculations around the Dirac point for different $\frac{\lambda_{\text{ISB}}}{\lambda_{\text{SOC}}}$ ratios in Fig. 4.15a. For a small In-Si bond length, and the associated strong ISB, an AABB stacking of the OAM of

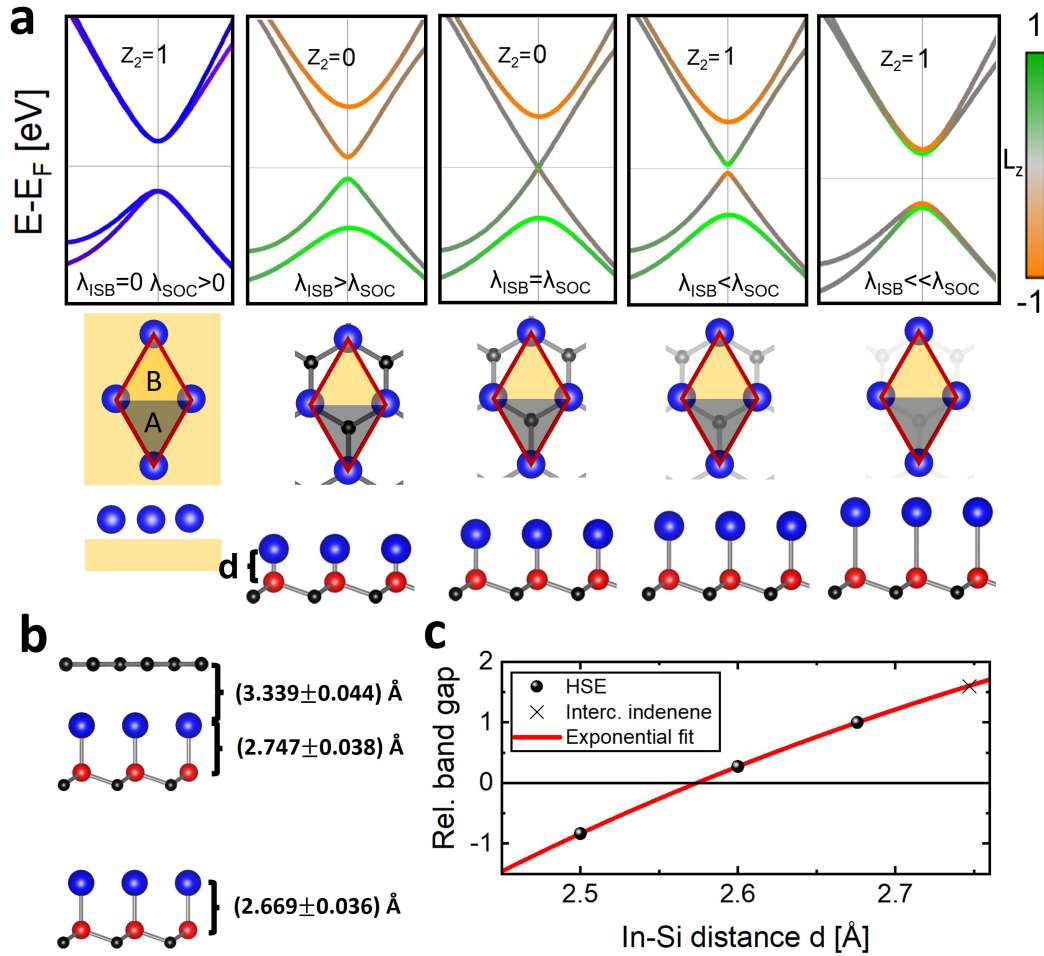


Fig. 4.15: **a** Tight binding model of the K point for decreasing ISB strength λ_{ISB} and the associated increase of the In-Si bond length d . Small distances d (large λ_{ISB}) lead to the trivial phase, whereas large distances d (small λ_{ISB}) correspond to the QSHI phase. **b** Ball-and-stick model with the bond length of the intercalated (top) and the pure (bottom) indenene, determined by the NIXSW measurement. **c** Hybrid functional HSE calculation of the relative band gap compared to indenene, as a function of the In-Si bond length. By extrapolating the HSE data points by a non-physical curve, the non-trivial energy gap for the intercalated indenene is expected to be around 60% larger than for the pristine indenene.

the valence and conduction band is observed. This corresponds to the trivial phase. By decreasing the ISB strength further the trivial band gap closes and reopens yielding an alternating stacking of the OAM, indicating the non-trivial phase. This non-trivial energy gap increases by increasing the In-Si distance d . The In-Si bond length as a function of the band gap at the K point was also calculated using the hybrid functional HSE, which leads to the results shown in Fig. 4.15c. As DFT calculations underestimate band gaps, the relative band gap compared to the pristine indenene is displayed in Fig. 4.15c. A negative relative band gap corresponds to the trivial phase. The non-physical exponential curve enables an extrapolation. The In-Si distance d for the intercalated monolayer

indium based on the fit corresponds to a 60% larger energy gap as the pure indenene. Therefore, the topological non-trivial energy gap of the QSHI indenene is expected to be around 200 meV.

The lifting of the indium atoms through the graphene capping layer drives indenene even more into the QSHI regime. Therefore, it has been shown that there is an interaction between the graphene and the intercalated material, even if the indenene-graphene distance is about 92% of the van der Waals bonding distance.

Chapter 5

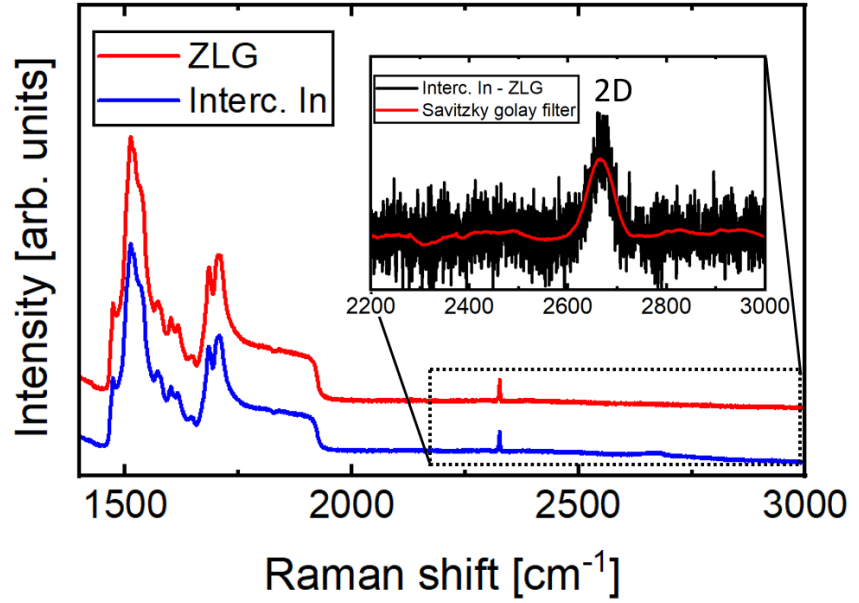
Conclusion and Outlook

In this thesis, the successful intercalation of bilayer and monolayer indium into the graphene/SiC interface was presented. Previous work on this topic reported so far mainly the graphene decoupling after the intercalation. Here, the focus was placed on the capping of a QSHI. Furthermore, it was shown, that graphene protects the indenene from degradation in air.

Growth of graphene - A full control of graphene growth on SiC was shown, by reproducing ZLG, MLG and BLG. The three different graphene coverages were analyzed in this work, as a starting point for the intercalation. The ZLG as well as the monolayer and bilayer graphene on top of the buffer layer were investigated and identified based on fingerprints reported in the literature using STM, PES and LEED.

Indenene intercalation - The intercalation method in this work uses ZLG as a template. STM measurements before and after the intercalation reveal the decoupling of the buffer layer and the associated formation of a quasi-freestanding graphene layer on top of the intercalant. By employing a post-annealing step, the 2ML In film can be reduced to a single layer. The study was corroborated by surface and interface sensitive techniques and it was possible to successfully identify ML and BL In intercalation by comparing to respective films without graphene. A XPS oxidation study of the capped and uncapped indenene sample demonstrates the protection from ambient conditions by the graphene layer. In addition, STEM images reveal the indium atoms being located exactly above the Si atoms. The comparison of the data from the capped and uncapped 2D material is so far unique. Although the band structure is qualitatively the same, detailed studies of the In-Si bonding distance showed, that graphene affects the In film - an impact that can be very important, especially with regards to the sensible interplay of ISB and SOC in indenene. This disproved, that graphene has no influence on the intercalated material and it cannot be assumed to be freestanding, as claimed in previous publications [99].

Fig. 5.1: Raman spectroscopy ($h\nu = 532$ nm) before (red) and after (blue) the indenene intercalation. The inset displays the difference of the two signals in the dashed marked area. After the ZLG decoupling, the graphene 2D peak is visible. However, due to the intercalated indium atoms, a red shift of around 50 cm^{-1} compared to the MLG on a SiC substrate is observed [132].



In the specific case of the indenene, the graphene lifts the In-Si bond length to a 7.8 pm larger distance than without the graphene capping. Such a height change of the indenene results in a decreasing strength of the inversion symmetry break. This in turn implies a larger non-trivial energy gap for the intercalated indenene compared to the pristine one.

Outlook - Based on these results we envision the following future experiments:

- Transport measurements of the intercalated system alone are not very promising due to the metallic graphene layer on top of the QSHI. When indenene is grown on the Si-terminated 4H-SiC(0001) substrate, it shows topological non-trivial properties. But it is assumed, that the indenene is in a trivial insulating phase, when growing it on the C-side of the substrate. After a successful indenene intercalation on both substrate sides, transport measurements could confirm the topological properties of the indenene, when comparing the results from the QSHI phase with the trivial insulating phase.
- The influence of the ISB and SOC on the topology can be further determined, by applying strain to the intercalated system to decrease or increase the In-Si bond length physically. As already shown, this goes along with a change in the ISB strength. Alternative other elements with a larger SOC can be intercalated, like Pb or Bi.
- The successful capping opens the door for ex-situ experiments, such as the Raman spectroscopy, to further characterize indenene. Fig. 5.1. displays the first attempts, which show the graphene 2D peak after the intercalation and the associated ZLG

decoupling. Furthermore, a red shift of the graphene 2D peak compared to the MLG on a SiC substrate [132] is observed. The results so far leave expectations on further investigations of the system and in particular to find an indenene related Raman signal potentially allowing to judge about the chemical state of indenene.

Bibliography

- [1] C. Mora; R.L. Rollins; K. Taladay; M.B. Kantar; M.K. Chock; M. Shimada and E.C. Franklin. *Nat. Clim. Change*, **8**, 931-933, (2018).
- [2] Y. Fan; P. Upadhyaya; X. Kou; M. Lang; S. Takei; Z. Wang; J. Tang; L. He; L.T. Chang; M. Montazeri; G. Yu; W. Jiang; T. Nie; R.N. Schwartz; Y. Tserkovnyak and K.L. Wang. *Nat. Mater.*, **13**, 699-704, (2014).
- [3] G.E. Moore. *Electronics*, **38**, 8, (1965).
- [4] K.S. Novoselov; A.K. Geim; S.V. Morozov; D. Jiang; Y. Zhang; S.V. Dubonos; I.V. Grigorieva and A.A. Firsov. *Science*, **306**, 5696, (2004).
- [5] C.L. Kane and E.J. Mele. *Phys. Rev. Lett.*, **95**, 226801, (2005).
- [6] J.C. Boettger and S.B. Trickey. *Phys. Rev. B*, **75**, 121402, (2007).
- [7] M. König; S. Wiedmann; C. Brüne; A. Roth; H. Buhmann and L.W. Molenkamp. *Science*, **318**, 766, (2007).
- [8] F. Reis; G. Li; L. Dudy; M. Bauernfeind; S. Glass; W. Hanke; R. Thomale; J. Schäfer and R. Claessen. *Science*, **357**, 6348, (2017).
- [9] M. Bauernfeind; J. Erhardt; P. Eck; P.K. Thakur; J. Gabel; T.L. Lee; J. Schäfer; S. Moser; D. Di Santo; R. Claessen and G. Sangiovanni. *Nat. Commun.*, **12**, 5396, (2021).
- [10] S. Glass; F. Reis; M. Bauernfeind; J. Aulbach; M.R. Scholz; F. Adler; L. Dudy; G. Li; R. Claessen and J. Schäfer. *J. Phys. Chem. C*, **120**, 19, 10361-10367, (2016).
- [11] D.P. Woodruff; B.C.C. Cowie and A.R.H.F. Etteman. *J. Phys. Condens. Matter.*, **6**, 10633-10645, (1994).
- [12] B. Fultz and J.M. Howe. *Transmission Electron Microscopy and Diffractometry of Materials*. 3rd ed. Springer Berlin, Heidelberg, ISBN: 978-3-642-29760-1, (2008).

- [13] P. Buseck; J. Cowley and L. Eyring. *High-Resolution Transmission Electron Microscopy: And Associated Techniques*. Oxford University Press, ISBN: 0195042751, (1989).
- [14] B. Schrader. *Infrared and Raman spectroscopy: methods and applications*. John Wiley & Sons, ISBN: 978-3-527-61542-1, (2008).
- [15] A.D. Becke. *J. Chem. Phys.*, **140**, 18A301, (2014).
- [16] K. Capelle. *Braz. J. Phys.*, **36**, 1318-1343, (2006).
- [17] G. Binnig; H. Rohrer; C. Gerber and E. Weibel. *Appl. Phys. Lett.*, **40**, 178, (1982).
- [18] C. Bai. *Scanning Tunneling Microscopy and Its Applications*. Springer Berlin, Heidelberg, ISBN: 3-540-65715-0 (1992).
- [19] R. Wiesendanger. *Scanning Tunneling Microscopy Spectroscopy*. Cambridge university press, ISBN: 0-521-41810-0 (1998).
- [20] J. Bardeen. *Phys. Rev. Lett.*, **6**, 57, (1961).
- [21] J. Tersoff and D.R. Hamann. *Phys. Rev. B*, **31**, 2, (1985).
- [22] M.P. Seah and W.A. Dench. *Phys. Rev.*, **30**, 705, (1927).
- [23] C. Davisson and L.H. Germer. *Phys. Rev.*, **30**, 705, (1927).
- [24] W. Friedrich; P. Knipping and M.v. Laue. *Interferenz-Erscheinungen bei Röntgenstrahlen*. Verl. der Königlichen Bayer. Akad. der Wiss. 303, (1912).
- [25] W.H. Bragg and W.L. Bragg. *Proc. R. Soc. Lond. A.*, **88**, 428-438, (1913).
- [26] T. Fauster; L. Hammer; K. Heinz and A. Schneider. *Oberflächenphysik*. De Gruyter Oldenbourg, ISBN: 9783110636697, (2019).
- [27] G. Ertl and J. Küppers. *Low Energy Electrons and Surface Chemistry*. VCH Verlagsgesellschaft, 0895730650, (1986).
- [28] M.A. van Hove; W.H. Weinberg and C.M. Chan. *Low energy electrons diffraction-Experiment, Theory and Surface Structure Determination*. Springer-Verlag Berlin Heidelberg, ISBN: 978-3-642-82723-5, (1986).
- [29] F. Reinert and S. Hüfner. *New. J. Phys.*, **7**, 97, (2005).
- [30] S. Hüfner. *Photoelectron Spectroscopy: Principles and Applications*. 3rd ed. Springer Berlin, Heidelberg, ISBN: 978-3-540-41802-3, (2003).

- [31] H.R. Hertz. *Ann. Phys. Chem.*, **31**, 983-1000, (1887).
- [32] W. Hallwachs. *Ann. Phys. Chem.*, **33**, 301-312, (1888).
- [33] A. Einstein. *Ann. Phys.*, **322**, 132-148, (1905).
- [34] W.E. Spicer and C.N. Berglund. *Phys. Rev. Lett.*, **12**, 9-11, (1964).
- [35] C. Nordling; E. Sokolowski and K. Siegbahn. *Phys. Rev.*, **105**, 1676-1677, (1957).
- [36] A. Damascelli. *Phys. Scr.*, **T109**, 61, (2004).
- [37] S. Suga; A. Sekiyama and C. Tusche. *Photoelectron Spectroscopy Bulk and Surface Electronic Structures*. 2nd ed. Springer Berlin, Heidelberg, ISBN: 978-3-662-52371-1, (2021).
- [38] K. Oura; V.G. Lifshits; A.A. Saranin; A.V Zotov and M. Katayama. *Surface Science: An Introduction*. Springer Berlin, Heidelberg, ISBN: 978-3-540-00545-2, (2003).
- [39] G.H. Major; N. Fairley; P.M.A. Sherwood; M.R. Linford; J. Terry; V. Fernandez and K. Artyushkova. *J. Vac. Sci. Technol. A.*, **38**, 061203, (2020).
- [40] D.A. Shirley. *Phys. Rev. B*, **5**, 4709, (1972).
- [41] A.H. Castro Neto; F. Guinea; N.M.R. Peres; K.S. Novoselov and A.K. Geim. *Rev. Mod. Phys.*, **81**, 109, (2009).
- [42] H. Raza. *Graphene Nanoelectronics*. Springer Berlin, Heidelberg, ISBN: 978-3-662-51990-5, (2012).
- [43] C. Riedl. *Epitaxial Graphene on Silicon Carbide Surface: Growth, Characterization, Doping and Hydrogen Intercalation*. PhD thesis Friedrich-Alexander-Universität Erlangen-Nürnberg, (2010).
- [44] S. Mammadov. *Polarization Doping and Work Function of Epitaxial Graphene on Silicon Carbide*. PhD thesis Technische Universität Chemnitz, (2018).
- [45] P.R. Wallace. *Phys. Rev.*, **71**, 622, (1947).
- [46] M.I. Katsnelson. *Graphene Carbon in Two Dimensions*. Cambridge University Press, ISBN: 9780521195409, (2012).
- [47] M.I. Katsnelson; K.S. Novoselov and A.K. Geim. *Nat. Phys.*, **2**, 620-625, (2006).
- [48] Y. Zhang; Y.W. Tan; H.L. Stormer and P. Kim. *Nature*, **438**, 201-204, (2005).

- [49] K.S. Novoselov; Z. Jiang; Y. Zhang; S.V. Morozov; H.L. Stromer; U. Zeitler; J.C. Maan; G.S. Boebinger; P. Kim and A.K. Geim. *Science*, **315**, 5817, (2007).
- [50] K.I. Bolotin; F. Ghahari; M.D. Shulman; H.L. Stromer and P. Kim. *Nature*, **462**, 196-199, (2011).
- [51] X. Du; I. Skachko; A. Barker and E.Y. Andrei. *Nat. Nanotechnol.*, **3**, 491-495, (2008).
- [52] C. Lee; X. Wei; J.W. Kysar and J. Hone. *Science*, **321**, 5887, (2008).
- [53] K. Yoshizawa; T. Kato and T. Yamabe. *J. Chem. Phys.*, **105**, 2099, (1996).
- [54] M.S. Dresselhaus and G. Dresselhaus. *Adv. Phys.*, **51**, 1-186, (2002).
- [55] E. McCann; D. Abergel and V. Falko. *Phys. J. Spec. Top.*, **148**, 91-103, (2007).
- [56] A.S. Mayorov; D.C. Elias; M. Mucha-Kruczynski; R.V. Gorbachev; T. Tudorovskiy; A. Zhukov; S.V. Morozov; M.I. Katsnelson; V.I. Falko; A.K. Geim and K.S. Novoselov. *Science*, **333**, 6044, (2011).
- [57] E. McCann and M. Koshino. *Rep. Prog. Phys.*, **76**, 056503, (2013).
- [58] Y. Cao; V. Fatemi; S. Fang; K. Watanabe; T. Taniguchi; E. Kaxiras and P. Jarillo-Herrero. *Nature*, **556**, 43-50, (2018).
- [59] K.V. Emtsev; F. Speck; T. Seyller; L. Ley and J.D. Riley. *Phys. Rev. B*, **77**, 155303, (2008).
- [60] K.S. Novoselov; A.K. Geim; S.V. Morozov; D. Jiang; M.I. Katsnelson; I.V. Grigorieva; S.V. Dubonos and A.A. Firsov. *Nature*, **438**, 197-200, (2005).
- [61] M. Ostler. *Quasi-free-standing Graphene on Silicon Carbide*. PhD thesis Friedrich-Alexander-Universität Erlangen-Nürnberg, (2014).
- [62] Y. Zhang; L. Zhang and C. Zhou. *Acc. Chem. Res.*, **46**, 10, 2329-2339, (2013).
- [63] A.M. Shikin; G.V. Prudnikova; V.K. Adamchuk; F. Moresco and K.-H. Rieder. *Phys. Rev. B*, **62**, 13202, (2000).
- [64] P.W. Sutter; J.I. Flege and E.A. Sutter. *Nat. Mater.*, **7**, 406-411, (2008).
- [65] A.B. Preobrajenski; M. Ling Ng; A.S. Vinogradov and N. Martensson. *Phys. Rev. B*, **78**, 073401, (2008).

- [66] A. Bauer; J. Kräußlich; L. Dressler; P. Kuschnerus; J. Wolf; K. Goetz; P. Käckell; J. Furthmüller and F. Blechstedt. *Phys. Rev. B*, **57**, 2647, (1998).
- [67] L.D. Madsen. *J. Electron. Mater.*, **30**, 1353-1360, (2000).
- [68] S. Link. *Intercalation of Graphene on SiC(0001): Ultra-high Doping Levels and New 2D materials*. PhD thesis Friedrich-Alexander-Universität Erlangen-Nürnberg, (2017).
- [69] F. Reis. *Realization and Spectroscopy of the Quantum Spin Hall Insulator Bismuthene on Silicon Carbide*. PhD thesis Julius-Maximilians-Universität Würzburg, (2021).
- [70] C. Riedl; U. Starke; J. Bernhardt; M. Franke and K. Heinz. *Phys. Rev. B*, **76**, 245406, (2007).
- [71] L. Simon; J.L. Bischoff and L. Kubler. *Phys. Rev. B*, **60**, 11653, (1999).
- [72] P. Martensson; F. Owman and L.I. Johansson. *Phys. Status Solidi B*, **202**, 501, (1997).
- [73] P. Ciochon; M. Marzec; N. Olszowska and J. Kolodziej. *Appl. Surf. Sci.*, **528**, 146917, (2020).
- [74] S. Goler; C. Coletti; V. Piazza; P. Pingue; F. Colangelo; V. Pellegrini; K.V. Emtsev; S. Forti; U. Starke; F. Beltram and S. Heun. *Carbon*, **51**, 249-254, (2013).
- [75] G.M. Rutter; N.P. Guisinger; J.N. Crain; E.A.A. Jarvis; J.M.D. Stiles; T. Li; P.N. First and J.A. Stroscio. *Phys. Rev. B*, **76**, 235416, (2007).
- [76] W. Chen; H. Xu; L. Liu; X. Gao; D. Qi; G. Peng; S.C. Tan; Y. Feng; K.P. Loh and A.T. Shen Wee. *Surf. Sci.*, **596**, 176-186, (2005).
- [77] L. Li and I.S.T. Tsong. *Surf. Sci.*, **351**, 141-148, (1996).
- [78] U. Starke and C. Riedl. *J. Phys. Condens. Matter.*, **21**, 134016, (2009).
- [79] F. Varchon; P. Mallet; J.Y. Veuillen and L. Magaud. *Phys. Rev. B*, **77**, 235412, (2008).
- [80] S.Y. Zhou; G.H. Gweon; A.V. Fedorov; P.N. First; W.A. de Heer; D.H. Lee; F. Guinea; A.H. Castro Neto and A. Lanzara. *Nat. Mater.*, **6**, 770-775, (2007).
- [81] A. Bostwick; T. Ohta; T. Seyller; K. Horn and E. Rotenberg. *Nat. Phys.*, **3**, 36-40, (2007).

- [82] A. Pramanik; S. Thakur; B. Singh; P. Willke; M. Wenderoth; H. Hofsäss; G. Di Santo; L. Petaccia and K. Maiti. *Phys. Rev. Lett.*, **128**, 166401, (2022).
- [83] E.L. Shirley; L.J. Terminello; A. Santoni and F.J Himpfel. *Phys. Rev. B*, **51**, 13614, (1995).
- [84] J. Jobst; D. Waldmann; F. Speck; R. Hirner; D.K. Maude; T. Seyller and H.B. Weber. *Phys. Rev. B*, **81**, 195434, (2010).
- [85] Q. Wang; W. Zhang; L. Wang; K. He; X. Ma and Q. Xue. *J. Phys. Condens. Matter.*, **25**, 095002, (2013).
- [86] M.Z. Hasan and C.L. Kane. *Rev. Mod. Phys.*, **82**, 3045, (2010).
- [87] F.D.M. Haldane. *Phys. Rev. Lett.*, **61**, 2015, (1988).
- [88] K.v. Klitzing; G. Dorda and M. Pepper. *Phys. Rev. Lett.*, **45**, 494, (1980).
- [89] C.L. Kane. *Contemporary Concepts of Condensed Matter Science: Chapter 1- Topological Band Theory and the \mathbb{Z}_2 invariant*. Elsevier, ISBN: 978-0-444-63314-9, **6**, 3-34 (2008).
- [90] W.P. Su; J.R. Schrieffer and A.J. Heeger. *Phys. Rev. Lett.*, **42**, 1698, (1979).
- [91] J.K. Asboth; L. Oroszlany and A. Palyi. *A Short Course on Topological Insulators*. Springer Cham, ISBN: 978-3-319-25605-4, (2015).
- [92] M.S. Lodge; S.A. Yang; S. Mukherjee and B. Weber. *Adv. Mater.*, **33**, 2008029, (2021).
- [93] A. Molle; J. Goldberger; M. Houssa; Y. Xu; S.C. Zhang and D. Akinwande. *Nat. Mater.*, **16**, 163-169, (2017).
- [94] P. Vogt; P. De Padova; C. Quaresima; J. Avila; E. Frantzeskakis; M.C. Asensio; A. Resta; B. Ealet and G.L. Lay. *Phys. Rev. Lett.*, **108**, 155501, (2012).
- [95] M.E. Davila; L. Xian; S. Cahangirov; A. Rubio and G.L. Lay. *New J. Phys.*, **16**, 095002, (2014).
- [96] Ff. Zhu; Wj. Chen; Y. Xu; Cl. Gao; Dd. Guan; Ch. Liu; D. Qian; S.-C. Zhang and Jf. Jia. *Nat. Mater.*, **14**, 1020-1025, (2015).
- [97] J. Erhardt; M. Bauernfeind; P. Eck; M. Kamp; J. Gabel; T.L. Lee; G. Sangiovanni; S. Moser and R. Claessen. *J. Phys. Chem. C*, **126**, 16289-16296, (2022).

- [98] N. Briggs; B. Bersch; Y. Wang; J. Jiang; R.J. Koch; N. Nayir; K. Wang; M. Kolmer; W. Ko; A. Duran; S. Subramanian; C. Dong; J. Shallenberger; M. Fu; Q. Zou; Y.W. Chuang; Z. Gai; A.P. Li; A. Bostwick; C. Jozwiak; C.Z. Chang; E. Rotenberg; J. Zhu; A.C.T. van Duin; V. Crespi and J.A. Robinson. *Nat. Mater.*, **19**, 637-643, (2020).
- [99] Y.R. Lin; S. Wolff; P. Schädlich; M. Hutter; S. Soubatch; T.L. Lee; F.S. Tautz; T. Seyller; C. Kumpf and F.C. Bocquet. *Phys. Rev. B*, **106**, 155418, (2022).
- [100] C. Riedl; C. Coletti; T. Iwasaki; A.A. Zakharov and U. Starke. *Phys. Rev. Lett.*, **103**, 246804, (2009).
- [101] C. Virojanadara; A.A. Zakharov; R. Yakimova and L.I. Johansson. *Surf. Sci.*, **604**, L4, (2010).
- [102] Y. Sohn; S.W. Jung; F. Göhler; W.J. Shin; S. Cha; T. Seyller and K.S. Kim. *J. Korean Phys. Soc.*, **78**, 157-163, (2021).
- [103] S. Wolff; S. Roscher; F. Timmermann; M.V. Daniel; F. Speck; M. Wanke; M. Albrecht; T. Seyller. *Ann. Phys.*, **531**, 1900199, (2019).
- [104] F. Bisti; C. Profeta; H. Vita; M. Donarelli; F. Perrozzi; P.M. Sheverdyaeva; P. Moras; K. Horn and L. Ottaviano. *Phys. Rev. B*, **91**, 245411, (2015).
- [105] Y. Zhang; H. Zhang; Y. Cai; J. Song; D. Qiao; Q. Chen; F. Hu; P. Wang; K. Huang and P. He. *Chem. Phys. Lett.*, **703**, 33-38, (2018).
- [106] Q. Chu; L. Li; C. Zhu; Y. Zang; S. Lin and Y. Han. *Mater. Lett.*, **211**, 133-137, (2018).
- [107] A. Yurtsever; J. Onoda; T. Iimori; K. Niki; T. Miyamachi; M. Abe; S. Mizuno; S. Tanaka; F. Komori and Y. Sugimoto. *Small*, **12**, 3956-3966, (2016).
- [108] A. Bayani and K. Larsson. *Sci. Rep.*, **10**, 1042, (2020).
- [109] K. Yagyu; T. Tajiri; A. Kohno; K. Takahashi; H. Tochiara; H. Tomokage and T. Suzuki. *Appl. Phys. Lett.*, **104**, 053115, (2014).
- [110] C. Virojanadara; S. Watcharinyanon; A.A. Zakharov and L.I. Johansson. *Phys. Rev. B*, **82**, 205402, (2010).
- [111] C. Ghosal; M. Gruschwitz; J. Koch; S. Gemming and C. Tegenkamp. *Phys. Rev. Lett.*, **129**, 116802, (2022).

- [112] H. Kim; N. Tsogtbaatar; B. Tuvdendorj; A. Lkhagvasuren and J.M. Seo. *Carbon*, **159**, 229-235, (2020).
- [113] T. Hu; D. Yang; W. Hu; Q. Xia; F. Ma and K. Xu. *Carbon*, **171**, 829-836, (2021).
- [114] S.L. Wong; H. Huang; Y. Wang; L. Cao; D. Qi; I. Santoso; W. Chen and A.T.S. Wee. *ACS Nano*, **5**, 9, 7662-7668, (2011).
- [115] C. Xia; S. Watcharinyanon; A.A. Zakharov; L.I. Johansson; R. Yakimova and C. Virojanadara. *Surf. Sci.*, **613**, 88-94, (2013).
- [116] C. Xia; S. Watcharinyanon; A.A. Zakharov; L. Hultmann; L.I. Johansson; R. Yakimova and C. Virojanadara. *Phys. Rev. B*, **85**, 045418, (2012).
- [117] I. Antoniazzi; T. Chagas; M.J.S. Matos; L.A.B. Marcal; E.A. Soares; M.S.C. Mazzoni; R.H. Miwa; J.M.J. Lopes; A. Malachias; R. Magalhaes-Paniago and M.H. Oliveira Jr. *Carbon*, **167**, 746-759, (2010).
- [118] Y.C. Cheng; Z.Y. Zhu and U. Schwingenschlögl. *EPL*, **101**, 27008, (2013).
- [119] N.M. Caffrey; R. Armiento; R. Yakimova and I.A. Abrikosov. *Phys. Rev. B*, **92**, 081409(R), (2015).
- [120] J.C. Kotsakidis; A. Grubisic-Cabo; Y. Yin; A. Tadich; R.L. Myers-Ward; M. De-Jarld; S.P. Pavunny; M. Currie; K.M. Daniels; C. Liu; M.T. Edmonds; N.V. Medhekar; D.K. Gaskill; A.L.V. de Parga and M.S. Fuhrer. *Chem. Mater.*, **32**, 6464-6482, (2020).
- [121] A. Stöhr; S. Forti; S. Link; A.A. Zakharov; K. Kern; U. Starke and H.M. Benia. *Phys. Rev. B*, **94**, 085431, (2016).
- [122] M. Cardona and L. Ley. *Photoemission in Solids I*. Springer-Verlag Berlin Heidelberg, ISBN: 978-3-662-30919-3, (1978).
- [123] C.M. Polley; L.I. Johansson; H. Fedderwitz; T. Balasubramanian; M. Leandersson; J. Adell; R. Yakimova and C. Jacobi. *Nat. Commun.*, **11**, 2236, (2020).
- [124] S. Forti; S. Link; A. Stöhr; Y. Niu; A.A. Zakharov; C. Coletti and U. Starke. *Phys. Rev. B*, **99**, 115404, (2019).
- [125] B. Matta; P. Rosenzweig; O. Bolkenbaas; K. Küster and U. Starke. *Phys. Rev. Res.*, **4**, 023250, (2022).

- [126] I. Mills; T. Cvitas; K. Homann and N. Kallay. *Quantities, Units and Symbols in Physical Chemistry*. International union of pure and applied chemistry, ISBN: 978-0-85404-433-7, (1993).
- [127] M. Alonso; R. Cimino and K. Horn. *Phys. Rev. Lett.*, **64**, 16, (1990).
- [128] M.J. Bedzyk. *Encyclopedia of Cond. Matt. Phys.*, **6**, 330, (2005).
- [129] T.J. Reber; N.C. PLumb; J.A. Waugh and D.S. Dessau. *Rev. Sci. Instrum.*, **85**, 043907, (2014).
- [130] M. Mantina; A.C. Chamberlin; R. Valero; C.J. Cramer and D.G. Truhlar. *J. Phys. Chem. A*, **113**, 5806-5812, (2009).
- [131] H. Güntherodt and D. Anselmetti. *Scanning Tunneling Microscopy I: General Principles and Applications to Clean and Adsorbate-Covered Surfaces*. Springer-Verlag Berlin Heidelberg, ISBN: 3540584153, (1994).
- [132] N. Ferralis. *J. Mater. Sci.*, **45**, 5135-5149, (2010).

Acknowledgements

Mit dem Abschluss dieser Arbeit möchte ich mich bei all denjenigen bedanken, die zum Gelingen dieser Arbeit beigetragen haben.

An erster Stelle möchte ich mich bei Herrn Prof. Dr. Ralph Claessen für die Möglichkeit bedanken, dass ich meine Masterarbeit am Lehrstuhl der Experimentellen Physik IV anfertigen durfte. Durch die Teilnahme an Konferenzen und Strahlzeiten konnte ich Einblicke in das wissenschaftliche Arbeiten auch außerhalb unseres Lehrstuhls bekommen.

Weiterhin möchte ich mich bei Dr. Simon Moser für die ständige Unterstützung bedanken. Nicht nur im Labor, sondern auch bei wissenschaftlichen und auch nicht-wissenschaftlichen Diskussionen konnte ich im letzten Jahr viel dazulernen.

Ein herzlicher Dank gilt auch meinem Betreuer Jonas Erhardt. Er hat mich während der gesamten Zeit super betreut, mich in alle Messanlagen eingelernt und auf jede meiner Fragen eine Antwort gehabt. Außerdem möchte ich mich für die erfolgreiche Zusammenarbeit und die Hilfe bei unserem gemeinsamen Paper bedanken.

Special thanks go to Dr. Kyungchan Lee for the help in the laboratory and the maintenance work. Furthermore I want to thank Dr. Bing Liu for the the supervision during in the first steps of this thesis

I would also like to thank everyone who was involved in the three beamtimes, namely Jonas Erhardt, Philipp Kessler, Matthias Schmitt, Dr. Timur Kim and explicitly Dr. Tien-Lin, Dr. Deepnarayan Biswas and the Oxide-team for the XSW measurements.

Vielen Dank auch an Philipp Eck für die theoretischen Rechnungen dieser Arbeit und Dr. Martin Kamp für die SEM und TEM Bilder.

Ein herzlicher Dank gilt auch Moni Seifer, die sich um alle nötigen Dinge kümmert und dem Team somit sehr viel Arbeit abnimmt. Zum Abschluss möchte ich mich noch bei allen weiteren weiteren Kolleginnen und Kollegen der EPIV für die schöne Zeit bedanken.

Das Zustandekommen dieser Arbeit hing auch wesentlich von der unermüdlichen Unterstützung meiner Freunde und Familie ab. Ein großer Dank geht dabei an meine Eltern, meinen Bruder Pascal und meine Freundin Merit. Vielen Dank für Eure Geduld, Aufmerksamkeit und Liebe.

Selbstständigkeitserklärung

Ich, Cedric Franz Schmitt, versichere, dass ich die vorstehende Arbeit selbstständig und ohne fremde Hilfe angefertigt und mich keiner anderer als der in den beigefügten Verzeichnissen angegebenen Hilfsmittel bedient habe. Alle Textstellen, die wörtlich oder sinngemäß aus Veröffentlichungen Dritter entnommen wurden, sind als solche kenntlich gemacht. Weitere Personen waren an der geistigen Leistung der vorliegenden Arbeit nicht beteiligt. Die eingereichte elektronische Fassung der Arbeit ist vollständig. Mir ist bewusst, dass nachträgliche Ergänzungen ausgeschlossen sind. Die Arbeit wurde bisher keiner anderen Prüfungsbehörde vorgelegt und auch nicht veröffentlicht.

Würzburg, den 21. Dezember 2022

.....

Cedric Franz Schmitt